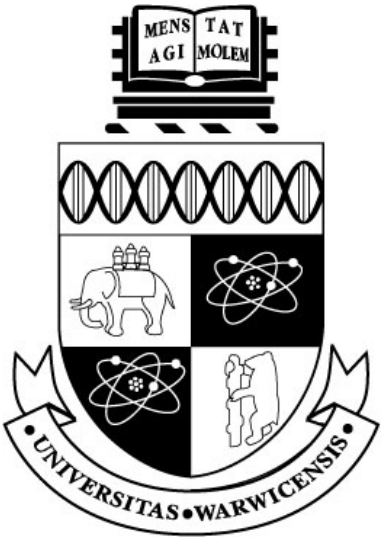

Multinuclear NMR of Hybrid Proton Electrolyte Membranes in Metal Oxide Frameworks

by

Frederik Hintz Romer

Thesis

Submitted to the University of Warwick

for the degree of

Doctor of Philosophy

Department of Physics

January 2017

THE UNIVERSITY OF WARWICK

Contents

Acknowledgements

First and foremost, I would like to express my gratitude to Prof. John V. Hanna, for his constant guidance and support throughout my PhD. I would also like to thank all the members of the solid-state NMR group at Warwick for creating such an enjoyable environment. I am also immensely grateful to my friends and family, particularly my parents Lone and Harald as well as my girlfriend Mona, for their incredible love and support, without which this could not have been possible.

Declarations

The work contained in this thesis is a result of my original research, carried out between September 2011 - August 2015, under the supervision of Prof. John V. Hanna at the University of Warwick. Where contributions of others are included, these are indicated within the text. This work has not been submitted for another degree.

Abbreviations

NSF	Naphthalene Sulphonate Formaldehyde
SPEEK	Sulfonated Poly(Ether Ether Ketone)
CP	Cross Polarisation
MAS	Magic Angle Spinning
RF	Radio Frequency
EMF	Electromotive Force
BPP	Bloembergen, Pound and Pucell
PEM	Proton Electrolyte Membrane
MOF	Metal Oxide Framework
mTiO_2	Mesoporous Titanium Oxide
mNb_2O_2	Mesoporous Niobium Oxide
mTa_2O_2	Mesoporous Tantalum Oxide
PFG	Pulsed Field Gradient

Chapter 1

A Brief Overview of Proton Electrolyte Membranes

A fuel cell converts chemical fuel into electrical energy through a chemical reaction where a hydrogen containing fuel source reacts with an oxidising agent which is usually oxygen from the air [1–3]. The difference between fuel cells and batteries is that a fuel cell produces electricity continuously as long as fuel and oxygen are provided. Whereas in batteries the chemicals are present inside the battery and react with each other to produce electricity.

All fuels cells contain an anode, a cathode and an electrolyte which separates the anode and cathode. The hydrogen fuel is split into protons and electrons using a catalyst at the anode. Oxygen is split at the cathode. Then depending on the type of electrolyte used either H^+ diffuse to the cathode or O^{2-} diffuse to the anode where they form water. The electrons generated at the anode flow in an external circuit where the electrical energy can be used. In this work we focus on when the electrolyte is a proton exchange membrane (PEM) where protons diffuse from the anode to the cathode. This is illustrated in figure 1.1. In such a system the reactions at the anode and cathode as well as overall

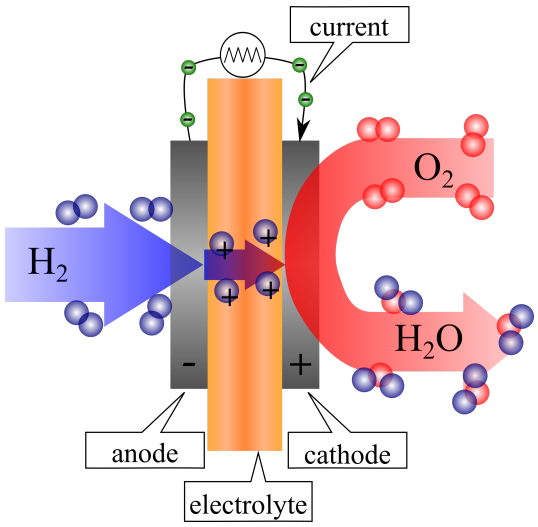

Figure 1.1: A schematic of a fuel cell with using a hydrogen fuel. Protons diffuse through a proton electrolyte membrane from the anode to the cathode where they react with oxygen to form water.

reactions are respectively,

$$\begin{aligned} H_2 &\rightarrow 2H^+ + 2e^- \\ O_2 + 4H^+ + 4e^- &\rightarrow 2H_2O \\ 2H_2 + O_2 &\rightarrow 2H_2O. \end{aligned}$$

The energy contained in the molecular bonds are released in the form of electrons and little wasted in the form of heat in comparison to the conventional combustion engines which are used in modern vehicles. The incease is approximately from 20% in combustion engines to over 40% in a PEM fuel cell. Thus there is huge potential for economics as well as incidental environmental benefits if PEM fuel cells are developed and brought into common use.

The first fuel cell powered by hydrogen and oxygen gas was created by William Robert Grove in 1839. He immersed ends of two platinum electrodes in a solution of sulphuric acid on one side and hydrogen or oxygen on the other. This resulted in a current flowing betwen the electrodes while the level of water in sealed containers within the gas chambers rose. This device was called a "gas

voltaic" battery [4, 5].

In 1889 Ludwig Mond and Carl Langer created a fuel cell which ran on gas derived from coal instead of hydrogen as had been used until then [6]. They called this "Mond-gas" and it is notable for being the first use of a hydrogen containing fuel which was not diatomic hydrogen.

In 1893 Friedrich Wilhelm Ostwald explained the performance of fuel cells. He determined the role each of the components of fuel cells and how it related to all the others. This included explaining function of the electrodes, electrolyte and oxidising and reducing agents [7]. His work in effect explained how Groves gas battery worked which until this point had been been unknown and a topic of heated debate.

In 1933 Francis Thomas Bacon made an alkali based fuel cell which uses hydroxide as oxidant instead of oxygen [8]. This design was later developed by NASA for use in space due to its clean operation and the only end product being drinkable water. The result was a 1.5 kW "Apollo fuel cell" used in space on the Apollo missions between 1958-9 [9].

In the 1950s fluorinated and sulfonated carbon chains become available for use as electrolyte membranes. In 1955 the first commercial fuel cell was made by Willard Thomas Grubb for General Electric (GE) [10]. It used a proton exchange membrane of sulfonated polystyrene. Three years later in 1958 another GE scientist Leonard Niedrach succeeded in depositing platinum on the membrane to act as catalyst for the oxidation of hydrogen and reduction of oxygen [10]. This fuel cell was also the PEM cell and it was used in the Gemini space missions between 1962 and 1965 to power the craft in space [9, 11].

In the 1970s scientist at DuPont built a fuel cell using a new flourinated polymer called Nafion as their proton electrolyte membrane. This polymer is still the most widely used today due to mechanical durability and conductivity [12] which no material since has been able to match commercially. However, like other fluorinated polymers it relies on being hydrated by water for its proton conduction which limits its operating temperature to 80 °C [3].

PEM are currently receiving renewed interest due to their use in fuel cells

(FCs) which are capable of replacing the internal combustion engine. The advantage in power generation efficiency of fuel cells over conventional engines makes them ideal replacements in areas such as the transport industry, distributed power and portable electrical devices.

Today the main problems holding back the commercialisation of fuel cells in vehicles is the lack of an appropriate and cost effective electrolyte membrane. Most electrolytes operate at high temperatures of many hundred degrees. This is for obviously undesirable in a moving vehicle as such materials would need to be heated to their conducting temperature before operation. Polymer electrolyte membranes have shown significant proton conductance in the intermediate temperature regime of 150°C to 200°C [13,14]. These temperatures are also required as carbon monoxide (CO) poisons the platinum nanoparticle (Pt/C) catalyst used at the anode at lower temperatures [14–16]. This is because there is a large entropy associated with Gibbs free energy of CO adsorption onto Pt/C which can overcome the enthalpy of adsorption at high temperatures [16].

In addition to having a high proton conductivity the desired properties of an ideal PEM for use in fuel cells include both long term structural and thermal stability of the proton conductivity. An anhydrous membrane which eliminates the need for water management systems which plagues the current Nafion based membranes. Any membrane also needs to be as inexpensive as possible to allow for use in mass production [13].

The amount of articles exploring one or more of these areas have exploded [17]. Recent developments in materials for PEMs involve immobilising heterocyclic aromatic compounds such as imidazole [18, 19], triazole [20, 21], pyrazole [22] and and benzimadole [20, 23] to a scaffold to improve their thermal and structural stability. These heterocycles posses all both hydrogen acceptor (base) and donor (acid) sites and by analogy to water this is thought to be why they are good at forming hydrogen bonded networks which can be used for proton transport. While the scaffolds successfully stabilise the heterocycles it comes at the cost of significantly reduced proton conductivity.

This work is focused on the proton conductivity of Naphthalene Sulfonate

Formaldehyde (NSF) resin which is made up of polymerised naphthalene monomers with an acidic sulfonate group attached. The NSF resin adsorbed into the pores of mesoporous metal oxides to stabilise the polymer thermally and mechanically as with the heterocycles. The sulfate acid is much stronger than the nitrogen based heterocycles but NSF does not have any groups which can act as proton acceptors. However, the walls of the pores in the Titanium, Tantalum and Niobium oxides used in this work are also acidic which means that they could also participate in proton conduction. It therefore the goal of this thesis to elucidate as far as possible the diffusion pathway of NSF resin adsorbed into the pores of a metal oxide. Of particular focus how the metal oxide framework is able to enhance the proton conductivity of NSF resin observed in bulk [24, 25] and determining whether the pore walls participate in the proton transport.

1.1 Nuclear Magnetic Resonance of Proton Electrolyte Membranes

It has been shown that proton conduction can occur via two distinct mechanisms. The first is vehicle transport i.e. water molecules physically moving and bring protons along [26]. The second is Grotthus jumping or structural diffusion protons jumping between hydrogen bonding sites in a sample [26, 27]. These mechanisms are not mutually exclusive and it is well established that the high proton conductivity of water is higher than can be explained purely by vehicle diffusion of H_2O molecules. There is a significant contribution to the overall diffusion rate by structural diffusing protons between adjacent water molecules through the formation of hydroxyl (OH^-) and hydroxonium (H_3O^+) [28–30]. As has been discussed water is not desirable in the PEM of a fuel.

Therefore there is impetus to understand rapid structural diffusion in order to help in the creation of an anhydrous material which can transport protons purely through structural diffusion. At its simplest structural diffusion is protons jumping from one site to another which cascades into macroscopic diffusion. The local proton jumps occur at very different time scales and are heavily de-

pendent on the local structure for the availability of hydrogen bonding sites to jump between. It has been shown that a high density of hydrogen bonding sites which are dynamically connected meaning each site can be connected to several others at different times yields increased proton motion. This enables proton motion to cascade into rapid diffusion [26, 31]. The local environments which protons experience as well as the dynamics of the motion vary greatly between samples.

Nuclear magnetic resonance provides a set of powerful tools to investigate all these aspects of proton transport at an inherently local level which distinguishes it from other analytical tools such as diffraction. The principal way to investigate motion using NMR involves identical experiments repeated at many different temperatures to observe the evolution of a particular property and then model this evolution.

The simplest parameter this is done with is the proton chemical shift which is extremely sensitive to changes in the local environment [32, 33]. This has been used to calculate the rate constant for proton transport between a hydrogen bonded and free state when participating in diffusion [34]. The change in the rate constant can then be used in an Arrhenius plot to calculate the energy barrier between these two states. However, this exact analysis is only possible in situations where there is symmetric exchange [34]. Nevertheless, this illustrates that the chemical shift carries much information about the dynamic processes which protons participate in [35, 36].

A closely related property when discussing proton transport is the width of the proton resonance which is inversely related to the T_2 relaxation. The linewidth of the resonance is also directly related to the exchange rate between hydrogen bonded sites and thus proton diffusion. This is because motion averages inhomogeneous magnetic fields over the period of the NMR experiment. This can again be modelled as random motion which must overcome a certain energy barrier to occur and is therefore modelled using an Arrhenius analysis [37–40]. Such analysis is however often complicated by overlapping resonances which prevent the accurate determination of the linewidth. This can be sometimes be alleviated using labelling and observation of deuterium [41–43].

The spin lattice T_1 relaxation is likewise affected by motion of the diffusion protons. This can be modelled by assuming the only interaction which causes T_1 relaxation is the fluctuation in the proton homonuclear dipolar coupling due to motion as it is much larger than any other interaction. This is called the BPP model and combined with the assumption that all motion causing relaxation in this model has an associated characteristic frequency which is thermally activated and random. This means the the characteristic frequency of the motion can be simulated using an Arrhenius relationship allows one to calculate the expected T_1 relaxation at a given temperature [36,44–48]. However, simulating the the T_1 data in most samples requires an empirical modification to the model which is called the stretched BPP [49,50].

Diffusion rate can be measured using a technique called pulsed field gradient NMR [51]. In the case of proton conducting materials it has been used to measure the diffusion of water hydrated membranes with a fluoridated carbon polymer chain like Nafion [52,53] and SPEEK [52] as well as molten phosphor based acids [54–56] and room temperature ionic liquids [57]. A diffusion measurement of a proton conductor mesoporous zeolite Si-MCM-41 which is neither hydrated nor liquid has been achieved using magic angle spinning during the PFG experiment [58].

Chapter 2

NMR Theory

This chapter lays out the foundations of the quantum mechanical theory behind NMR including a description of the matrix formalism used to describe nuclear spins and their time evolution as well as the effect of the dipolar coupling and how its line broadening effect may be eliminated. This chapter is based mostly on the books written by Abragam [59], Duer [60] and Callaghan [61].

2.1 Mathematical Description of an NMR experiment

2.1.1 Nuclear Spin

Spin is an intrinsic property of matter in the same way as electric charge, mass or energy are properties of matter. The spin of a nucleus is determined by its constituent protons and neutrons. Spin is quantised in units of $\hbar$ (the reduced Plank constant) and its maximum value is dependent on the *spin angular momentum quantum number*, I, which can take a positive integer or half-integer values.

Each nucleus with a spin I has $2I+1$ spin states, which, without the presence of a permanent magnetic field, are degenerate. Spins possess a perma-

nent magnetic moment, $\boldsymbol{\mu}$, which interacts with any applied magnetic field, $\mathbf{B}_0$, whereby the degeneracy of the spin states is lifted. This is called the *Zeeman interaction* and the energy shift it causes, denoted in classical terms, is,

$$E = -\boldsymbol{\mu} \cdot \mathbf{B}_0. \tag{2.1}$$

When this is expressed by quantum mechanical operators the result is the *Zeeman Hamiltonian*, $\hat{\mathscr{H}}_Z$, given by,

$$\hat{\mathscr{H}}_Z = -\hat{\boldsymbol{\mu}} \cdot \mathbf{B}_0 = -\gamma \hbar \hat{\mathbf{I}} \cdot \mathbf{B}_0, \tag{2.2}$$

where γ is the gyromagnetic ratio, $\hat{\boldsymbol{\mu}}$ is the operator for the magnetic moment and $\hat{I}$ is the operator for the spin angular momentum. In NMR the applied magnetic field is described as an axial field along the z-axis in which case the Zeeman Hamiltonian becomes

$$\hat{\mathscr{H}}_Z = -\gamma \hbar B_0 \hat{I}_z, \tag{2.3}$$

where $\hat{I}_z$ the component of the spin angular momentum parallel to the z-axis. This equation is often written as,

$$\hat{\mathscr{H}}_Z = \omega_0 \hat{I}_z, \tag{2.4}$$

where $\omega_0 = -\gamma B_0$ is called the *Larmor frequency* and $\hbar$ has been dropped resulting in units of angular frequency. The gyromagnetic ratio is a constant for a particular spin isotope which means each isotope has a characteristic Larmor frequency under a particular field strength.

2.1.2 Angular Momentum Operators

Any system in quantum mechanics can be described by a wavefunction, $|\psi\rangle$, which contains the information about the physical properties of the system. Such information can be extracted from the wavefunction using an operator, $\hat{A}$, which

represents the desired physical property. Using Dirac notation the *expectation value*, $\langle A \rangle$, can be calculated

$$\langle A \rangle = \langle \psi | \hat{A} | \psi \rangle. \tag{2.5}$$

A spin system is described by the wavefunctions $|I, m\rangle$ where I is the spin angular momentum quantum number and m the magnetic quantum number. The operators representing spin angular momentum are $\hat{I}_x, \hat{I}_y, \hat{I}_z$ and $\hat{I}^2$. The first three are components of the spin along the x, y and z axes, while the latter is the total spin. The spin wavefunctions $|I, m\rangle$ are eigenfunctions of the $\hat{I}_z$ and $\hat{I}^2$ operators and are therefore referred to as the Zeeman eigenfunctions with their eigenvalues given by

$$\hat{I}^2 |I, m\rangle = I(I+1)|I, m\rangle \tag{2.6}$$

$$\hat{I}_z |I, m\rangle = m|I, m\rangle, \tag{2.7}$$

where m can take values $I, I-1, ..., -I$ for a total of $2I+1$ states. The work presented in this thesis has used spins with $I = 1/2$. Such spins have two states which are commonly labelled $|\alpha\rangle$ (spin up) and $|\beta\rangle$ (spin down), where following equation 2.7:

$$\hat{I}_z |\alpha\rangle = +\tfrac{1}{2}|\alpha\rangle \qquad \hat{I}_z |\beta\rangle = -\tfrac{1}{2}|\beta\rangle. \tag{2.8}$$

In order to completely describe a spin $I = 1/2$ quantum mechanically, a linear superposition of its two states is used

$$|\psi\rangle = c_\alpha |\alpha\rangle + c_\beta |\beta\rangle, \tag{2.9}$$

where c_α and c_β are complex coefficients which determine the weighting of each state. Using equation 2.5, the expectation value for the $\hat{I}_z$ operator is

$$\langle \hat{I}_z \rangle = c_\alpha c_\alpha^* \langle \alpha | \hat{I}_z | \alpha \rangle + c_\alpha c_\beta^* \langle \alpha | \hat{I}_z | \beta \rangle + c_\beta c_\alpha^* \langle \beta | \hat{I}_z | \alpha \rangle + c_\beta c_\beta^* \langle \beta | \hat{I}_z | \beta \rangle \tag{2.10}$$

$$= \tfrac{1}{2}(c_\alpha c_\alpha^* - c_\beta c_\beta^*). \tag{2.11}$$

However, $|\alpha\rangle$ and $|\beta\rangle$ are not eigenfunctions of the $\hat{I}_x$ and $\hat{I}_y$ operators. Instead applying these operators leads to interconversion between the states.

$$\hat{I}_x|\alpha\rangle = \tfrac{1}{2}|\beta\rangle \quad \hat{I}_x|\beta\rangle = \tfrac{1}{2}|\alpha\rangle \quad \text{and} \quad \hat{I}_y|\alpha\rangle = \tfrac{i}{2}|\beta\rangle \quad \hat{I}_y|\beta\rangle = -\tfrac{i}{2}|\alpha\rangle. \tag{2.12}$$

The expectation values of the $\hat{I}_x$ and $\hat{I}_y$ operators therefore becomes

$$\langle\hat{I}_x\rangle = \tfrac{1}{2}(c_\alpha c_\beta^* + c_\beta c_\alpha^*) \quad \langle\hat{I}_y\rangle = \tfrac{i}{2}(c_\alpha c_\beta^* - c_\beta c_\alpha^*). \tag{2.13}$$

From equations 2.11 and 2.13 it can be seen that while the expectation value of the $\hat{I}_z$ operator is defined by the self-products of the coefficients, the expectation values of $\hat{I}_x$ and $\hat{I}_y$ only contains the cross-products of the coefficients. This fact allows the calculation of the expectation value in a more efficient notation as will be shown in the next section.

2.1.3 The Density Matrix and Operator

When a spin system is small, the linear combination of states is sufficient. However, if there are several coupled spins or if $I > 1/2$ then this notation becomes unwieldy. Calculations become convenient by using a matrix notation instead. An operator, $\hat{A}$, can be described by a matrix with elements $A_{rs} = \langle r|\hat{A}|s\rangle$, where for a single spin with $I = 1/2$ then r and s are both either α or β:

$$\mathbf{A} = \begin{pmatrix} A_{\alpha\alpha} & A_{\beta\alpha} \\ A_{\alpha\beta} & A_{\beta\beta} \end{pmatrix} = \begin{pmatrix} \langle\alpha|\hat{A}|\alpha\rangle & \langle\beta|\hat{A}|\alpha\rangle \\ \langle\alpha|\hat{A}|\beta\rangle & \langle\beta|\hat{A}|\beta\rangle \end{pmatrix}. \tag{2.14}$$

This is called the *matrix representation* of operator $\hat{A}$ in the eigenbasis of $\hat{I}_z$.

Likewise the spin system can be described by a matrix, using the *density operator*:

$$\hat{\rho} = \overline{|\psi\rangle\langle\psi|}, \tag{2.15}$$

where the overbar refers to the *ensemble average* of the spins – this will be omit-

ted for simplicity in the following. This gives rise to the *density matrix* with elements $\rho_{rs} = \langle r|\hat{\rho}|s\rangle = \langle r|\psi\rangle\langle\psi|s\rangle$ where for a single spin with $I = 1/2$ then $|\psi\rangle$ is defined in equation 2.9 while r and s remain defined as in equation 2.14:

$$\boldsymbol{\rho} = \begin{pmatrix} \rho_{\alpha\alpha} & \rho_{\beta\alpha} \\ \rho_{\alpha\beta} & \rho_{\beta\beta} \end{pmatrix} = \begin{pmatrix} c_\alpha c_\alpha^* & c_\beta c_\alpha^* \\ c_\alpha c_\beta^* & c_\beta c_\beta^* \end{pmatrix}. \tag{2.16}$$

It can be seen clearly that the effect of the density operator is to extract the coefficient of the state it operates on. This means the elements of the density matrix are self-products and cross-products of the coefficients seen in the expectation values of the angular momentum operators in equations 2.11 and 2.13. To extract these terms from the density matrix a matrix multiplication is performed with the matrix representation of the operator:

$$\boldsymbol{\rho}\mathbf{A} = \begin{pmatrix} c_\alpha c_\alpha^* A_{\alpha\alpha} + c_\beta c_\alpha^* A_{\beta\alpha} & c_\alpha c_\alpha^* A_{\beta\alpha} + c_\beta c_\alpha^* A_{\beta\beta} \\ c_\alpha c_\beta^* A_{\alpha\alpha} + c_\beta c_\beta^* A_{\alpha\beta} & c_\alpha c_\beta^* A_{\alpha\beta} + c_\beta c_\beta^* A_{\beta\beta} \end{pmatrix}. \tag{2.17}$$

The diagonal elements contained in the matrix above are the exact terms as in equation 2.10 used to calculate the expectation value of the angular momentum operators. The off-diagonal elements, however, are not relevant and therefore discarded. This is done formally by taking the trace of the matrix:

$$\langle A\rangle = Tr(\boldsymbol{\rho}\mathbf{A}) = c_\alpha c_\alpha^* A_{\alpha\alpha} + c_\beta c_\alpha^* A_{\beta\alpha} + c_\alpha c_\beta^* A_{\alpha\beta} + c_\beta c_\beta^* A_{\beta\beta}. \tag{2.18}$$

The above equation contains the full expression for the expectation value of an angular momentum operator. However, the matrix representation of any operator contains several elements which are zero which significantly reduces the number of terms one needs to consider.

2.1.4 The Propagator

The signal which is detected by a NMR spectrometer is the result of the bulk magnetisation generated by the spins precessing at the Larmor frequency. The

evolution of the precession generates a time varying signal, which is detected by induction using the spectrometer circuitry. In this context, it is appropriate to discuss the evolution with time of a spin ensemble, in the form of the density operator, $\hat{\rho}(t)$, to describe the NMR signal.

The time evolution of any wavefunction, $|\psi\rangle$, can be described by the time dependent Schrödinger equation:

$$\frac{d}{dt}|\psi\rangle = -\imath\hat{\mathscr{H}}|\psi\rangle, \tag{2.19}$$

where $\hat{\mathscr{H}}$ is the time independent Hamiltonian acting on the spin system. If a similar differentiation is applied to the density operator from equation 2.15, then the Liouville von-Neumann equation can be derived:

$$\frac{d}{dt}|\hat{\rho}(t)\rangle = -\imath\left[\hat{\mathscr{H}}, \hat{\rho}(t)\right], \tag{2.20}$$

which has the standard solution:

$$\hat{\rho}(t) = e^{-\imath\hat{\mathscr{H}}t}\hat{\rho}(0)e^{\imath\hat{\mathscr{H}}t}. \tag{2.21}$$

This is an extremely powerful equation which allows one to calculate the density matrix, and hence the state of the whole spin system, at any time. The only requirements are that the initial state of the density matrix, $\hat{\rho}(0)$, and the Hamiltonian, $\hat{\mathscr{H}}$, acting on the system in the subsequent time are known. At thermal equilibrium, $\hat{\rho}(0) \propto \hat{I}_z$. The form of the Hamiltonian is discussed in more detail in the next section.

2.2 The Hamiltonian

The complete Hamiltonian affecting a spin system at any one time is comprised of a number of terms, each one a Hamiltonian due to a specific interaction. For

a diamagnetic sample, the complete set of terms is:

$$\hat{\mathscr{H}}_{total} = \hat{\mathscr{H}}_Z + \hat{\mathscr{H}}_{RF} + \hat{\mathscr{H}}_D + \hat{\mathscr{H}}_Q + \hat{\mathscr{H}}_J + \hat{\mathscr{H}}_{CS}, \tag{2.22}$$

each of these Hamiltonians can be written in a completely general form:

$$\hat{\mathscr{H}}_\Lambda = \hat{\mathbf{I}} \cdot \tilde{\mathbf{\Lambda}} \cdot \hat{\mathbf{S}} = \begin{bmatrix} \hat{I}_x & \hat{I}_y & \hat{I}_z \end{bmatrix} \begin{bmatrix} A_{xx} & A_{xy} & A_{xz} \\ A_{yx} & A_{yy} & A_{yz} \\ A_{zx} & A_{zy} & A_{zz} \end{bmatrix} \begin{bmatrix} \hat{S}_x \\ \hat{S}_y \\ \hat{S}_z \end{bmatrix}, \tag{2.23}$$

where $\tilde{\mathbf{\Lambda}}$ is a second rank tensor, $\hat{\mathbf{I}}$ is a spin operator and $\hat{\mathbf{S}}$ can be either another spin operator or an external field.

The simplest example of such a Hamiltonian is the Zeeman Hamiltonian, $\hat{\mathscr{H}}_Z$, which describes the interaction between the nuclear spin, $\hat{\mathbf{I}}$, and the external magnetic field, $\hat{\mathbf{B}}_0$, and is written as:

$$\hat{\mathscr{H}}_Z = \hat{\mathbf{I}} \cdot \tilde{\mathbf{Z}} \cdot \hat{\mathbf{B}}_0, \tag{2.24}$$

where

$$\tilde{\mathbf{Z}} = -\gamma \begin{bmatrix} 1 & 0 & 0 \\ 0 & 1 & 0 \\ 0 & 0 & 1 \end{bmatrix}, \tag{2.25}$$

where γ is the gyromagnetic ratio. The Zeeman Hamiltonian defines the geometry of the *laboratory frame*, which is the frame all other Hamiltonian tensors have to be expressed in relation to. In this frame, the external magnetic field is aligned with the z-axis such that $\hat{\mathbf{B}}_0 = \begin{bmatrix} 0 & 0 & \hat{B}_0 \end{bmatrix}$. Likewise, the magnetisation of the spins in this frame is also aligned with the z-axis and therefore $\hat{\mathbf{I}} = \begin{bmatrix} 0 & 0 & \hat{I}_z \end{bmatrix}$. This results in the familiar Zeeman Hamiltonian from section 2.1.1:

$$\hat{\mathscr{H}}_Z = -\gamma B_0 \hat{I}_z = \omega_0 \hat{I}_z. \tag{2.26}$$

2.2.1 Spherical Tensors

For each of the Hamiltonians in equation 2.22, there is a *principal axis frame* (PAF) in which the second rank tensor, $\tilde{\mathbf{A}}$, in equation A.1 only has diagonal elements which are non-zero. The PAF is, however, not coincident with the laboratory frame, defined by the Zeeman Hamiltonian, and from which one observes the spin system experimentally. The PAF is, because of its diagonal tensor, the preferred frame to use. However, interaction tensors in the PAF have to undergo a frame rotation to bring them into the laboratory frame. This transformation is necessary because the effect of the interaction has no physical meaning unless it is expressed in the frame which it is observed from.

Cartesian tensors are a nuisance to perform frame rotations on as after just one rotation it very likely that all nine tensor elements are non-zero. It is instead convenient to use a set of basis operators with spherical symmetry, the *irreducible spherical tensor operators*. Irreducible spherical tensors, $\hat{T}_j$, have a *rank* $j = 0, 1, 2, ...$ and each contain operator elements, $\hat{T}_{j,m}$, which are labelled with an order $m = j, j-1, ..., -j$. All the spherical tensors up to and including rank $j = 2$ are shown in Appendix A.

The elements of a tensor with rank j form a complete set under rotation, i.e., elements with different ranks do not mix. This is due to irreducible spherical tensor operators transforming like the irreducible representation of the three dimensional rotation point group and it greatly reduces the number of non-zero elements obtained after a rotation. The Hamiltonian of interaction Λ can be written as a sum of several irreducible spherical tensor operators:

$$\hat{\mathscr{H}}_{\Lambda} = \sum_{j=0}^{2} \sum_{m=-j}^{+j} (-1)^m A_{j,m} \hat{T}_{j,-m}, \tag{2.27}$$

where $A_{j,m}$ describes the orientation dependence of the interaction Λ, while $\hat{T}_{j,-m}$ are the appropriate operators for the spin component of the interaction.

In the PAF, where only the diagonal elements of the interaction tensor, Λ, are non-zero it follows from the equations in 2.27 only four components of these

irreducible spherical tensor are non-zero:

$$\hat{\mathscr{H}}_{\Lambda}^{PAF} = A_{0,0}^{PAF}\hat{T}_{0,0} + A_{2,0}^{PAF}\hat{T}_{2,0} + A_{2,2}^{PAF}\hat{T}_{2,-2} + A_{2,-2}^{PAF}\hat{T}_{2,2}. \tag{2.28}$$

In addition, some Hamiltonians have even fewer terms contributing due to additional symmetry elements in the interaction. For example, the dipolar coupling, which will be discussed in more detail later, only has a single non-zero tensor element, $\hat{\mathscr{H}}_{D}^{PAF} = A_{2,0}^{PAF}\hat{T}_{2,0}$.

2.2.2 Frame Transformations

The transformation from the principal axis frame, $\hat{\mathscr{H}}_{\Lambda}^{PAF}$, into the laboratory frame, $\hat{\mathscr{H}}_{\Lambda}^{LAB}$, is performed via three successive rotations through the Euler angles ($\alpha \quad \beta \quad \gamma$) about the axes in the original PAF. The full rotation, $\hat{\mathbf{R}}(\alpha,\beta,\gamma)$, is described in terms of each rotation individually:

$$\hat{\mathbf{R}}(\alpha,\beta,\gamma) = \hat{\mathbf{R}}_z(\gamma)\hat{\mathbf{R}}_y(\beta)\hat{\mathbf{R}}_z(\alpha), \tag{2.29}$$

where $\hat{\mathbf{R}}_a(\theta)$ is a rotation about the axis a by an angle θ and it can be shown that it takes the form

$$\hat{\mathbf{R}}_a(\theta) = \exp(-\imath\theta\hat{I}_a). \tag{2.30}$$

For an irreducible spherical tensor, the equivalent frame transformation is performed using a rotation matrix of the form

$$D^{j}_{m',m}(\alpha\beta\gamma) = \exp(-\imath m'\alpha)d^{j}_{m',m}(\beta)\exp(-\imath m\gamma), \tag{2.31}$$

where $d^{j}_{m',m}(\beta)$ is a reduced Wigner rotation matrix element. A rotation from a starting frame, A^{PAF}, to an end frame, A^{LAB}, using the rotation operator with Euler angles, $\hat{\mathbf{R}}(\alpha_{PL},\beta_{PL},\gamma_{PL})$, is therefore performed using an equation of the

form

$$A^{LAB}_{j,m'} = \sum_m A^{PAS}_{j,m} D^j_{m,m'}(\alpha_{PL}, \beta_{PL}, \gamma_{PL}), \tag{2.32}$$

whereby the Hamiltonian of the interaction in the laboratory frame becomes

$$\hat{\mathscr{H}}^{LAB}_{\Lambda} = \sum_{j=0}^{2} \sum_{m=-j}^{+j} (-1)^m \hat{T}_{j,-m} \sum_{m'} A^{PAS}_{j,m'} D^j_{m',m}(\alpha_{PL}, \beta_{PL}, \gamma_{PL}). \tag{2.33}$$

This description only holds for static samples. In order to take into account the effect of magic angle spinning, an intermediary frame, the *rotor frame*, needs to be introduced. This will be discussed in section 2.4.

2.2.3 The Secular Approximation

Of all the terms contributing to the complete Hamiltonian in equation 2.22 the Zeeman Hamiltonian, $\hat{\mathscr{H}}_Z$, is the strongest. The rest of the interactions have Hamiltonians

$$\hat{\mathscr{H}}_1 = \hat{\mathscr{H}}_{RF} + \hat{\mathscr{H}}_D + \hat{\mathscr{H}}_Q + \hat{\mathscr{H}}_J + \hat{\mathscr{H}}_{CS}, \tag{2.34}$$

which can be well described as a small perturbation on the Zeeman Hamiltonian. If this is the case then the eigenfunctions of $\hat{\mathscr{H}}_1$ are well approximated by the eigenfunctions of the Zeeman Hamiltonian. Limiting the situation to when $\hat{\mathscr{H}}_1$ is purely described by the Zeeman eigenfunctions, which is a first order approximation, then the following holds.

Since $\hat{\mathscr{H}}_1$ and $\hat{\mathscr{H}}_Z$ have the same eigenfunctions they must also commute. This means only the parts of $\hat{\mathscr{H}}_1$ which actually commutes with $\hat{\mathscr{H}}_Z$ can affect the energy level of the spin eigenstates. Therefore, the operator for the spin in the irreducible spherical tensor, $\hat{T}_{j,m}$, in the perturbing Hamiltonians, $\hat{\mathscr{H}}_1$, must commute with the Zeeman Hamiltonian, i.e. $\hat{I}_z$. The commutator between these

two operators is

$$[\hat{I}_z, \hat{T}_{j,m}] = m\hat{T}_{j,m}. \tag{2.35}$$

Therefore, the only irreducible spherical tensors which can affect the Zeeman energy levels are those with an order of $m = 0$, as only under this circumstance do the operators commute. It must be noted that this is only true when examining the interactions in the laboratory frame. In this frame, using the secular approximation, only two tensors contribute to a Hamiltonian:

$$\hat{\mathscr{H}}_{\Lambda}^{LAB} = A_{0,0}^{LAB}\hat{T}_{0,0} + A_{2,0}^{LAB}\hat{T}_{2,0}. \tag{2.36}$$

2.3 Effect of Radio Frequency Pulses

A radio frequency pulse affects the spin system like a oscillating magnetic field, $B_1(t)$. As the magnetic field affecting the spin system is time dependent so are the resulting eigenstates and energies. A standard NMR probe can deliver a radio frequency pulse equivalent to an oscillating magnetic field B_1 of approximately 1 mT. This is several orders of magnitude less than a static magnetic field which is typically on the order of 10 T. This means that any RF field will have no effect on the spin states unless it is on resonance with the Larmnor frequency. In equation 2.2 we described the Zeeman Hamiltonian and we now add this oscillating magnetic field

$$\begin{aligned} \hat{\mathscr{H}} &= \hat{\mathscr{H}}_Z + \hat{\mathscr{H}}_{pulse} \\ &= -\gamma B_0 \hat{I}_z - 2\gamma B_1(t)\hat{\mathbf{I}} \\ &= \omega_0 \hat{I}_z + 2\omega_{nut}\cos(\omega_{rf}t + \phi)\hat{I}_x \end{aligned} \tag{2.37}$$

where the carrier wave of the oscillating magnetic field is ω_{rf} with phase ϕ and an amplitude $\omega_{nut} = \gamma B_1$ where B_1 is the maximum of the oscillating magnetic field. In order to see the effect of the RF pulse Hamiltonian on the spin system we must first remove the time dependence of the Hamiltonian. This is done by

transforming into a frame which is rotating around the z-axis at the frequency ω_{rf} using the rotation operator in equation 2.30 and applying it to the Hamiltonian in the following fashion:

$$\begin{aligned}\hat{\mathscr{H}}_{rot} &= \hat{\mathrm{R}}_z(-\omega_{rf}t)\hat{\mathscr{H}}\hat{\mathrm{R}}_z(+\omega_{rf}t) \\ &= \hat{\mathrm{R}}_z(-\omega_{rf}t)\left(\hat{\mathscr{H}}_Z + \hat{\mathscr{H}}_{pulse}\right)\hat{\mathrm{R}}_z(+\omega_{rf}t). \end{aligned} \tag{2.38}$$

As the $\hat{I}_z$ operator is invariant under rotation around the z-axis we only need to consider the effect on $\hat{\mathscr{H}}_{pulse}$. Thus in the rotating frame the Hamiltonian for the RF pulse becomes

$$\begin{aligned}\hat{\mathscr{H}}_{pulse,rot} &= \hat{\mathrm{R}}_z(-\omega_{rf}t)\hat{\mathscr{H}}_{pulse}\hat{\mathrm{R}}_z(+\omega_{rf}t) \\ &= -\omega_{rf}\hat{I}_z + \omega_{nut}\left(\hat{I}_x\cos\phi + \hat{I}_y\sin\phi\right). \end{aligned} \tag{2.39}$$

We can now choose the phase of the RF pulse to be $\phi = 0$ without any loss of generality and this yields the following form for the Hamiltonian in the rotating frame

$$\begin{aligned}\hat{\mathscr{H}}_{rot} &= \hat{\mathscr{H}}_Z + \hat{\mathscr{H}}_{pulse,rot} \\ &= \omega_0\hat{I}_z - \omega_{rf}\hat{I}_z + \omega_{nut}\hat{I}_x. \end{aligned} \tag{2.40}$$

As previously stated the static magnetic field giving rise to the Larmor frequency, ω_0, is much larger than the magnetic field caused by the oscillating magnetic field ω_{nut}. However, if we choose the carrier frequency, ω_{rf} of the oscillating magnetic field to be *on resonance* with the Larmor frequency $\omega_{rf} = \omega_0$ the effect of the static magnetic field is canceled and the Hamiltonian acting under these circumstances simply becomes

$$\hat{\mathscr{H}}_{rot} = \omega_{nut}\hat{I}_x. \tag{2.41}$$

which is analogous to the Zeeman Hamiltonian in equation 2.4. To understand the effect this Hamiltonian caused by an on resonance RF pulse on the equilibrium magnetisation $\hat{I}_z$ we use the Liouville-von Neumann equation from 2.21

which describes the effect of a Hamiltonian through time

$$\hat{\rho}(t) = e^{-\imath\omega_{nut}t\hat{I}_x}\hat{I}_z e^{\imath\omega_{nut}t\hat{I}_x} \tag{2.42}$$

By comparison to the rotation operators in equation 2.30 it is clear that this equation describes a rototation of the initially longitudinal magnetisation around the x-axis which generates transverse magnetisation along the y-axis

$$\hat{\rho}(t) = \hat{I}_z \cos\omega_{nut}t - \hat{I}_y \sin\omega_{nut}t. \tag{2.43}$$

It is clear that we can choose how much of the magnetisation we transfer from the z-axis to the y-axis by changing the duration, τ_{rf} of the applied pulse with nutation frequency ω_{nut}

$$\theta_{nut} = \omega_{nut}\tau_{rf} \tag{2.44}$$

For a pulse were the entire magnetisation is rotated to the y-axis this becomes $\omega_{nut}\tau_{rf} = \pi/2$ and we speak of a 90°-pulse. Similarly, a pulse where $\omega_{nut}\tau_{rf} = \pi$ is called a 180°- pulse.

This description of the RF pulse is still viewed from the rotating frame. If we briefly consider the view from the laboratory frame we observe that during the duration of the RF pulse the magnetisation still precesses around the z-axis while the magnetisation is simultaneously rotated around the x-axis. This type of rotation is called *nutation*.

2.3.1 NMR Signal Detection

When considering an ensemble of spins it is clear that the effect of the 90°_x-pulse described is entirely coherent magnetisation along $-\hat{I}_y$. For a spin 1/2 such a magnetisation is in fact an equal mixing of the $|\alpha\rangle$ and $|\beta\rangle$ states of the Zeeman Hamiltonian which point in a common direction. In the absence of a RF pulse this coherence continues to precess around the z-axis under the influence of the

Zeeman Hamiltonian

$$\hat{\rho}(t) = -\hat{I}_y \cos\omega_0 t + \hat{I}_x \sin\omega_0 t. \tag{2.45}$$

This describes magnetisation rotating clockwise around the z-axis in the transverse plane at the Larmor frequency which induces an electromotive force (EMF) in the coil used to generate the RF pulse. This is called the *free induction decay* or FID and is the manner in which the NMR experiment is detected.

This detection is actually achieved by mixing the signal measured at the Larmor frequency ω_0 with a reference frequency ω_{obs}. The effect of this can be seen by entering a frame rotating at ω_{obs}

$$\hat{\rho}_{rot}(t) = -\hat{I}_y \cos(\omega_0 - \omega_{obs})t + \hat{I}_x \sin(\omega_0 - \omega_{obs})t. \tag{2.46}$$

The complex signal operator $N\gamma[\hat{I}_x + \imath\hat{I}_y]$ is then used to extract the signal which is observed

$$\begin{aligned} Tr(N\gamma[\hat{I}_x + \imath\hat{I}_y]\hat{\rho}_{rot}(t)) = & - \imath \mathrm{Tr}(\hat{I}_y^2)\cos(\omega_0 - \omega_{obs})t \\ & + \mathrm{Tr}(\hat{I}_y^2)\sin(\omega_0 - \omega_{obs})t, \end{aligned} \tag{2.47}$$

where the trace is used to remove unobservable off diagonal elements.

Using the identity

$$\mathrm{Tr}(\hat{I}_x^2) = \mathrm{Tr}(\hat{I}_y^2) = \mathrm{Tr}(\hat{I}_z^2) = \frac{1}{3} I(2I+1)(I+1) \tag{2.48}$$

and the equilibrium magnetisation

$$M_{eq} = \frac{N\gamma^2 B_0 \hbar^2 I(I+1)}{3k_B T} \tag{2.49}$$

from Maxwell-Boltzmann statistics on spins in thermal equilibrium [61] where N is the density of spins. Combining equations 2.47, 2.48 and 2.49 allows us to

simply write the expected observed signal as

$$Tr(N\gamma[\hat{I}_x + \imath\hat{I}_y]\hat{\rho}_{rot}(t)) = \imath M_{eq}\exp(-\imath(\omega_0 - \omega_{obs})t) \tag{2.50}$$

This result is important as one can measure a signal from the EMF in this form using a method called RF heterodyne detection. In such a detection scheme the signal output of the RF coils which is in the form $V_0\cos\omega_0 t$ is split into two channels where it is mixed separately with a reference frequency which is 90°out of phase with each other by which is obtained separate in phase and quadrature phase output signals. Heterodyning with two quadrature channels is equivalent to multiplication

$$\begin{aligned} & V_0\cos\omega_0 t(\cos\omega t + \imath\sin\omega t) \\ = \;& V_0\cos\omega_0 t\exp(\imath\omega t) \\ = \;& V_0[\exp(-\imath(\omega_0 - \omega)t) + \exp(\imath(\omega_0 + \omega)t)]. \end{aligned} \tag{2.51}$$

It is clear that the first term in equation 2.51 is equivalent to equation 2.50 and therefore this method is capable of measuring the operators $\hat{I}_x + \imath\hat{I}_y$. The fact that we also measure the frequency sum is irrelevant as it can be easily eliminated using a filter.

2.4 Magic Angle Spinning

All interactions described by second rank tensors such as the dipolar coupling and the chemical shift have anisotropic components which affect the observed frequency depending on the molecular orientation relative to the applied B_0 magnetic field. In a powdered sample where all possible orientations may be assumed to be present this results in broad *powder pattern lineshape*. This gives rise to resonances with broad lineshapes which obscures spectral information such as the isotropic chemical shift, which is a quantity one needs to access to determine structural information. To recover this information, Magic Angle Spinning (MAS) is introduced, whereby the sample is spun around an axis in-

clined by an angle β_{RL}. This can be treated mathematically using the methods described in section 2.2.2 by inserting an intermediary rotating frame, the rotor frame, between the PAF and the laboratory frame. In order to understand the effect of MAS on any second order interaction such as the dipolar coupling or the chemical shift one need only consider the following tensor element,

$$\hat{\mathscr{H}}_D^{PAF} = A_{2,0}^{PAF}\hat{T}_{2,0}. \tag{2.52}$$

In order to transform into the rotor frame, the PAF is rotated through the Euler angles (α_{PR} β_{PR} γ_{PR}). Written in the form of equation 2.32, the transformation becomes:

$$A_{2,m}^{rotor} = A_{2,0}^{PAS} D_{0,m}^2(\alpha_{PR}, \beta_{PR}, \gamma_{PR}), \tag{2.53}$$

where $m = 0, \pm 1, \pm 2$ for a total of five terms. Note that the order, m, does not have to be zero, as it is not necessary to fulfil the secular approximation because this is not the laboratory frame. To reach this frame, another rotation through the Euler angles (α_{RL} β_{RL} γ_{RL}) is necessary. Here the angle α_{RL} describes the continual rotation of the intermediary rotor frame relative to the laboratory frame such that $\alpha_{RL} = -\omega_R t$, where ω_R is the rotation frequency in angular frequency units and γ_{PR} is the rotor phase relative to the magnetic field which defines the initial orientation of the interaction.

$$A_{2,0}^{LAB} = \sum_{m=-2}^{2} A_{2,0}^{PAF} D_{0,m}^2(\alpha_{PR}, \beta_{PR}, \gamma_{PR}) D_{m,0}^2(\alpha_{RL}, \beta_{RL}, \gamma_{RL}) \tag{2.54}$$

$$= \sum_{m=-2}^{2} A_{2,0}^{PAF} d_{0,m}^2(\beta_{PR}) d_{m,0}^2(\beta_{RL}) \exp(-\imath m \gamma_{PR}) \exp(-\imath m \alpha_{RL}), \tag{2.55}$$

where $A_{2,0}^{LAB}$ is the only term in the laboratory frame due to the secular approximation which now applies. When equation 2.55 is written in full, it becomes:

$$A_{2,0}^{LAB} = A_{2,0}^{PAF} \begin{pmatrix} \frac{1}{4}\left[3\cos^2\beta_{PR} - 1\right]\left[3\cos^2\beta_{RL} - 1\right] \\ -\frac{3}{4}\sin 2\beta_{PR} \sin 2\beta_{RL} \cos\left[\gamma_{PR} - \omega_R t\right] \\ +\frac{3}{4}\sin^2\beta_{PR} \sin^2\beta_{RL} \cos\left[2\gamma_{PR} - 2\omega_R t\right] \end{pmatrix}. \tag{2.56}$$

The inclination of the rotor frame relative to the laboratory frame, β_{RL}, is under experimental control and when it is set to $\beta_{RL} = 54.74°$, the $3\cos^2\beta_{RL} - 1$ term equals zero and equation 2.56 reduces to:

$$A_{2,0}^{LAB}(t) = A_{2,0}^{PAF}\begin{pmatrix} -\frac{1}{\sqrt{2}}\sin 2\beta_{PR}\cos[\gamma_{PR} - \omega_R t] \\ +\frac{1}{2}\sin^2\beta_{PR}\cos[2\gamma_{PR} - 2\omega_R t] \end{pmatrix}. \tag{2.57}$$

Every term describing the spatial dependency of the second rank tensor is now time dependent. The integral of equation 2.57 over a full rotor period $\Delta t = \tau_R = {}^{2\pi}/_{\omega_R}$ is zero:

$$\int_{t=0}^{\tau_R} A_{2,0}^{LAB}(t)dt = 0. \tag{2.58}$$

Equation 2.58 is interpreted as the time dependent part of the second rank tensor being averaged to zero over a full rotor cycle. However, the evolution during the free induction decay is often sampled more than once over a rotor cycle, and may therefore not be completely averaged to zero. This leads to the observation of spinning sidebands, if the spinning frequency is low compared to the magnitude of an interaction such as the dipolar coupling or chemical shielding.

2.5 Chemical Shift

The behaviour of the nucleus in reaction to an external magnetic field is the primary interest in NMR. However, the electrons which surround every nucleus are also affected by the external magnetic field of the NMR spectrometer. The electrons react to produce a secondary field which modifies the the total magnetic field experienced by the nucleus in a manner which depends on the local electron distribution. The interaction between this secondary magnetic field and the nucleus is called the *shielding interaction* and the frequency shift it causes in a NMR spectrum is called the *chemical shift*. When considering the shielding interaction it is helpful to decompose it into two components.

Firstly, all electrons affected by the external magnetic field are subject to the Lorentz force. For bound electrons this induces a current as they move within their orbitals. This motion causes a secondary field which opposes the external field at the centre of motion. The total magnetic field which is experienced by the nucleus is therefore reduced by the electron motion. This is called a shielding interaction and is known as the diamagnetic contribution. The strength of the interaction depends on the distance between the electrons and the nucleus. The dependence is of the order of $1/r^3$, where r is the radial distance between the nucleus and electrons. Consequently, the core electrons being closest to the nucleus contribute more than valence electrons which are further from the nucleus. This effect therefore tends to be fairly constant for a particular type of nucleus. However, the diamagnetic current at any one nucleus are affected by the surrounding atoms which each generate their own currents. The total effect of these diamagnetic currents on the NMR frequency is observed by changing the Larmor frequency of a given nucleus depending its local environment. This is the primary effect which causes the chemical shift.

Secondly, the external magnetic field distorts the ground state electron orbitals which determine the electron density distribution around a nucleus. This distortion of the ground state can be described as a perturbation of ground state by orbitals of a higher energy excited electronic state. These excited electronic states can be paramagnetic and therefore cause the resulting ground electronic state in an external magnetic field to slightly paramagnetic. The result of such a paramagnetic state is to create a secondary magnetic field which supports the external field and is therefore said to deshield the nucleus.

Importantly both these components are affected by changes in the local electronic density distribution and geometry. The resulting chemical shift is therefore highly dependent on the local electronic environment. This makes the chemical shift extremely valuable to an NMR spectroscopist as it is diagnostic of the local electronic density and hence structure.

The chemical shielding Hamiltonian acting on spin $\mathbf{I}$ while in the presence

of an external magnetic field $\mathbf{B_0}$ is written

$$\hat{\mathscr{H}}_{CS} = -\gamma \hat{\mathbf{I}} \cdot \boldsymbol{\sigma} \cdot \mathbf{B_0}, \tag{2.59}$$

where $\boldsymbol{\sigma}$ is a second rank Cartesian tensor called the chemical shielding tensor. The chemical shielding tensor can be diagonalised by choosing the correct principal axis frame. In this PAF the diagonal elements are frequently expressed as the isotropic shift, δ_{iso}, anisotropy, Δ, and asymmetry, η, which are defined as follows

$$\sigma_{iso} = \frac{1}{3}\left(\sigma_{xx} + \sigma_{yy} + \sigma_{zz}\right) \tag{2.60}$$

$$\Delta = \sigma_{zz} - \sigma_{iso} \tag{2.61}$$

$$\eta = \frac{\sigma_{xx} + \sigma_{yy}}{\Delta}. \tag{2.62}$$

These diagonal elements are commonly ordered and labeled as $\sigma_{zz} - \sigma_{iso} \geq \sigma_{xx} - \sigma_{iso} \geq \sigma_{yy} - \sigma_{iso}$. This is called the Haeberlen convention [62].

A typical sample used in solid state NMR is powdered. Such a sample contains many crystallites which have all possible orientations relative to the external magnetic field $\mathbf{B_0}$. Crystallites at each orientation give rise to a frequency shift. When the resonances of all crystallites at all orientations are co-added this yields a broad resonance called a powder pattern.

NMR experiments do not measure the chemical shift directly. Rather, the a reference compound is used and the frequencies of all resonances are measured relative to a specific resonance in spectrum of the reference. Therefore any chemical shifts quoted are offset frequencies relative to specific resonance in a specific compound and calculated using the following equation

$$\delta_{iso} = \frac{\nu - \nu_{ref}}{\nu_{ref}}, \tag{2.63}$$

where δ_{iso} is the isotropic chemical shift in units of *parts per million* or *ppm*.

There are more interesting theory and applications of the chemical shield-

ing which are discussed by Duer [60] but these are outside the scope of this work.

2.5.1 Under MAS

The anisotropies giving rise to a powder patterns which are recorded in static NMR experiments contains much information. However, in a spectrum containing more than a couple of resonances the patterns tend to overlap which obscures any useful information. The chemical shielding interaction, $\boldsymbol{\sigma}$, is a second rank tensor and as discussed in section 2.4 any anisotropic components arising from the interaction can be averaged to zero over a rotor period by spinning the sample around the magic angle. For each resonance where the MAS frequency is smaller than the anisotropy this results in the observation of a series spinning sidebands separated by the spinning frequency where the solid resonances would have been.

2.6 Dipolar Coupling

The dipolar coupling is the interaction between the permanent magnetic moments of two spins. It is a through space interaction, the magnitude of which depends on the orientation of the internuclear vector relative to the applied magnetic field, B_0. It is described by $\hat{\mathscr{H}}_D$, the dipolar Hamiltonian:

$$\hat{\mathscr{H}}_D = -2\sum_{i<j} \hat{\mathbf{I}}_i \cdot \tilde{\mathbf{D}} \cdot \hat{\mathbf{S}}_j, \tag{2.64}$$

where $\hat{\mathbf{I}}_i$ and $\hat{\mathbf{S}}_j$ refer to the i^{th} spin of isotope I and the j^{th} spin of isotope S, respectively. When I and S refer to spins of the same isotope then the interaction is called *homonuclear* and when they refer to different isotopes then the interaction is called *heteronuclear*. The interaction tensor $\tilde{\mathbf{D}}$ for the dipolar coupling has the particularity that in the PAF the trace of the matrix is zero $A_{xx}+A_{yy}+A_{zz}=0$ and axially symmetric $A_{xx}=A_{yy}\neq A_{zz}$. Therefore, there is only a single irreducible

spherical tensor element contributing to the Hamiltonian in this frame

$$\hat{\mathscr{H}}_D^{PAF} = A_{2,0}^{PAF}\hat{T}_{2,0}, \tag{2.65}$$

where

$$A_{2,0}^{PAF} = \sqrt{6}b_{ij}, \tag{2.66}$$

and b_{ij} is the dipole coupling constant (in rad s^{-1}) between the i^{th} I spin and the j^{th} S spin given by

$$b_{ij} = \hbar\left(\frac{\mu_0}{4\pi}\right)\frac{\gamma_I\gamma_S}{r_{ij}^3}, \tag{2.67}$$

where μ_0 is the permeability of free space and γ_I and γ_S are the gyromagnetic ratios of isotopes I and S respectively, while r_{ij} refers to the internuclear distance between spin i and j. Note that, for convenience, the dipolar coupling constant is here defined as positive, whereas it is often defined as a negative number. In units of Hz, the dipolar coupling constant becomes,

$$d_{ij} = b_{ij}/2\pi. \tag{2.68}$$

Using equations 2.31 and 2.32 to transform equation 2.65 from the PAF into the laboratory frame by rotating through the Euler angles (α_{PL} β_{PL} γ_{PL}):

$$\begin{aligned} A_{2,0}^{LAB,static} &= A_{2,0}^{PAS}D_{0,0}^2(\alpha_{PL},\beta_{PL},\gamma_{PL}) \\ &= A_{2,0}^{PAS}d_{0,0}^2(\beta_{PL}) \\ &= \sqrt{6}b_{ij}\tfrac{1}{2}\left[3\cos^2(\beta_{PL})-1\right] \end{aligned} \tag{2.69}$$

The spin operator of the spherical tensor, $\hat{T}_{2,0}$, is different depending on whether the dipolar interaction occurs between a pair of homonuclei or het-

eronuclei:

$$\hat{T}_{2,0}^{HET} = 2\hat{I}_z\hat{S}_z \tag{2.70}$$
$$\hat{T}_{2,0}^{HOM} = 2\hat{I}_z\hat{S}_z - (\hat{I}_x\hat{S}_x + \hat{I}_y\hat{S}_y) \tag{2.71}$$
$$= 2\hat{I}_z\hat{S}_z - \tfrac{1}{2}(\hat{I}_-\hat{S}_+ + \hat{I}_+\hat{S}_-) \tag{2.72}$$
$$= 3\hat{I}_z\hat{S}_z - \hat{\mathbf{I}}\cdot\hat{\mathbf{S}}, \tag{2.73}$$

where $\hat{I}_{+,-} = \hat{I}_x \pm \imath\hat{I}_y$ and $\hat{S}_{+,-} = \hat{S}_x \pm \imath\hat{S}_y$ are the raising and lowering operators. In all the above equations a normalisation factor of $\frac{1}{\sqrt{6}}$ has been omitted and the matrix representations of the operators for a pair of spin $I = \frac{1}{2}$ are:

$$2\hat{I}_z\hat{S}_z = \begin{bmatrix} \frac{1}{2} & 0 & 0 & 0 \\ 0 & -\frac{1}{2} & 0 & 0 \\ 0 & 0 & -\frac{1}{2} & 0 \\ 0 & 0 & 0 & \frac{1}{2} \end{bmatrix} \quad -(\hat{I}_x\hat{S}_x + \hat{I}_y\hat{S}_y) = \begin{bmatrix} 0 & 0 & 0 & 0 \\ 0 & 0 & \frac{1}{2} & 0 \\ 0 & \frac{1}{2} & 0 & 0 \\ 0 & 0 & 0 & 0 \end{bmatrix}. \tag{2.74}$$

2.6.1 Heteronuclear Coupling

For the heteronuclear case, only the $2\hat{I}_z\hat{S}_z$ term is present and contains only diagonal elements. Therefore the eigenstates of spins coupled by dipolar coupling are just products of the Zeeman eigenstates ($|\alpha\alpha\rangle, |\alpha\beta\rangle, |\beta\alpha\rangle, |\beta\beta\rangle$). It is possible to calculate the expectation value of the first order shift in energy which the Zeeman eigenstates experience, away from the Larmor frequency, when the dipolar coupling is taken into account:

$$\langle m_I m_S | 2\hat{I}_z\hat{S}_z | m_I m_S \rangle = 2 m_I m_S d', \tag{2.75}$$

where $d' = d_{ij}\frac{1}{2}\left[3\cos^2(\beta_{PL}) - 1\right]$.

For a pair of spin $I = \frac{1}{2}$ nuclei, this becomes,

$$|\alpha\alpha\rangle = |\beta\beta\rangle = +\tfrac{1}{2}d' \tag{2.76}$$
$$|\alpha\beta\rangle = |\beta\alpha\rangle = -\tfrac{1}{2}d'. \tag{2.77}$$

The result of all of the above is that the NMR signal detected from the spins changes from the Larmor frequency to a distribution of frequencies centred on the Larmor frequency given by

$$\begin{aligned} \nu_D(\beta) &= \nu_0 \pm d' \\ &= \nu_0 \pm d_{ij}\tfrac{1}{2}\left[3\cos^2(\beta)-1\right], \end{aligned} \tag{2.78}$$

the angle β, being unevenly distributed between 0 and π in a powdered sample, gives rise to an additional weighting of $\sin\beta$. The result is a broad resonance with a particular shape called a Pake doublet [63].

2.6.2 Homonuclear Coupling

When two homonuclear spins interact, the additional term of $\hat{I}_x\hat{S}_x + \hat{I}_y\hat{S}_y$ complicates matters. As can be seen in equation 2.72 this term can also be written as a combination of ladder operators, the effect of which is to mix the $|\alpha\beta\rangle$ and $|\beta\alpha\rangle$ eigenstates. The same is clear from the matrix representation in equation 2.74 which has two off diagonal elements which cause precisely this mixing. The effect is that the eigenstates of the dipolar Hamiltonian are no longer products of Zeeman eigenstates but linear combinations of them.

Furthermore, consider a three spin system, where one of the possible eigenstates consists of a linear combination of the $|\alpha\alpha\beta\rangle$, $|\alpha\beta\alpha\rangle$ and $|\beta\alpha\alpha\rangle$ Zeeman eigenstates. If an observation is made of a system in this state, it collapses into one of the Zeeman eigenstates. If repeated measurements are made then each of the Zeeman eigenstates will be seen at different times. If focussing on just one of the spins, I_1, then it would sometimes appear to be in state $|\alpha\rangle$ (when collapsed into $|\alpha\alpha\beta\rangle$ or $|\alpha\beta\alpha\rangle$) and sometimes state $|\beta\rangle$ (when collapsed into $|\beta\alpha\alpha\rangle$). Therefore, it appears as if I_1 is constantly changing its spin state between $|\alpha\rangle$ and $|\beta\rangle$ without the emission or absorption of a photon, as would be required if it were uncoupled. This is equivalent to there being a continuous exchange of z-magnetisation between the spins in the homonuclear network. This exchange has consequences when attempting to remove the effect of the dipolar

coupling by magic angle spinning as has been discussed in section 2.4.

When there are more than two homonuclear spins, the flip-flop term mixes degenerate Zeeman eigenstates, such that the resulting eigenfunctions for the full multiple spin system are linear combinations of the Zeeman eigenstates, which are not degenerate. This gives rise to multiple different transition frequencies, which when observed under static conditions gives rise to a large broadening. The lineshape becomes approximately Gaussian, when there are many coupled spins. This is called *homogenous* broadening.

2.6.3 Heteronucleus coupled to a homonuclear network

Finally, consider the effect of a large number of I spins in a homonuclear network coupled to just one heteronucleus S. Suppose that a single spin, I_1, is closer to S than any other spin in the homonuclear network and therefore this pair also has the strongest heteronuclear dipolar coupling. From the discussion above, it is clear that I_1 changes its spin state each time the system is observed. It should also be obvious that the magnitude of heteronuclear dipolar coupling depends on which eigenstate both S and I_1 are in. Hence, when repeatedly observing spin S, the associated $S-I_1$ dipolar coupling varies with each observation, as the heteronuclear dipolar coupling still depends on the ever changing I_1 state. In such a case, homogeneous broadening, similar to that which would be observed on the I_1 spin, is also present in a spectrum showing the S resonance. Therefore, when observing the S spin it is necessary to include the network of I spins in the description. This poses a problem when simulating spins in this situation as adding extra spins increases computation time exponentially.

2.6.4 Under MAS

Reducing the line broadening effect of homonuclear dipolar coupling between more than two spins is different to the case of a heteronuclear coupling of identical strength. This is caused by the phenomenon described in section 2.6.2, whereby the state of every spin in a homonuclear network varies, over time,

between Zeeman eigenstates $|\alpha\rangle$ and $|\beta\rangle$. The rate of change between eigenstates of a spin, I_1, is equal to the strength of the dipolar interactions affecting I_1 in frequency units. As MAS only averages the dipolar coupling to zero over a full rotor period, the spin state is required to remain unchanged in this time frame. Hence, to average the line broadening effect of a homonuclear dipolar coupling, the spinning frequency needs to significantly exceed the magnitude of the coupling being averaged. By contrast, it is possible to eliminate the line broadening effect of a heteronuclear dipolar coupling, when the spinning frequency is smaller than the size of the heteronuclear interaction.

2.7 Longitudinal Relaxation

The thermal equilibrium of a spin system was shown to be proportional to $\hat{I}_z$ in equation 2.4. In equation 2.43 it was shown that this equilibrium magnetisation can be converted into transverse magnetisation in the xy plane by the application of a RF pulse. The process by which magnetisation returns to its equilibrium state along $\hat{I}_z$ is called longitudinal relaxation or spin-lattice relaxation and has a characteristic time constant T_1.

Relaxation can be caused by anything which causes fluctuations in the local magnetic field through the molecular motion. In solid state NMR this motion tends to be forms of reorientation such as methyl rotation or chemical exchange such as self diffusion of hydrogen bonded protons. The causes of such fluctuations in the local field are the anisotropic interactions of the chemical shielding (see section 2.5), dipolar coupling (see section 2.6), quadrupolar moment (see section 2.9) and paramagnetism.

This work is focused mainly on the relaxation rate of self diffusing protons in organic polymers and metal oxide frameworks (MOFs). Under such circumstances the dominant interaction causing fluctuations in the magnetic field is the homonuclear dipolar coupling between protons.

The phenomenological description of the longitudinal relaxation are described by the Bloch equations [64]. If an ensemble of spins with no initial

magnetisation are suddenly subjected to a static magnetic field, B_0 the magnetisation along the z-axis is given by

$$M_z(t) = M_{eq}\left(1 - \mathrm{e}^{-t/\mathrm{T}_1}\right), \tag{2.79}$$

where M_z is the magnetisation along the z-axis after a time t and M_{eq} is the magnetisation along $\hat{I}_z$ at equilibrium and T_1 is the time constant describing how fast the magnetisation returns to the equilibrium state. Relaxation for a period of $t = T_1$ results in ∼63% of the equilibrium magnetisation aligned with the z-axis while after a period of $t = 5T_1$ ∼99.3% of the equilibrium magnetisation is aligned. This is important as if NMR measurements are repeated faster than the longitudinal relaxation returns the magnetisation to the equilibrium state one risks saturating the spins and consequently not generating the coherence one wishes to measure.

2.7.1 The Saturation Recovery

The saturation recovery experiment is an NMR experiment designed to measure the T_1 longitudinal relaxation. The sequence and coherence transfer pathway for this experiment is shown in figure 2.1.

The sequence begins with a series of high power pulses called a pulse comb. These pulses destroy all population differences between the Zeeman energy levels or coherences generated by previous RF pulses. The spins can be considered to be completely randomly distributed as if there were no external magnetic field affecting them.

After the pulse comb there is a period, τ_1, wherein the spin ensmble begins to relax back to its equilibrium state along the z-axis. The rate at which this happens in given in equation 2.79.

Then, a 90°-pulse is applied which excites all coherences for a specific nuclei. However, the only one which is of interest is the coherence $p = -1$ which can be detected in the coil. The magnitude of signal detected is proportional to the number of spins which give rise to it.

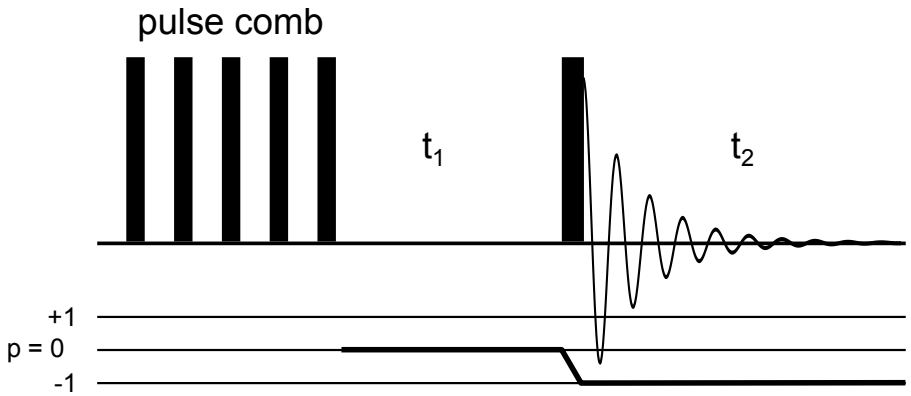

Figure 2.1: The pulse sequence for a saturation recovery experiment (top) and its coherence transfer pathway (bottom). The black rectangles are RF pulses while the duration between pulses are periods of free precession.

This means that the magnitude of the signal detected in this case depends on how big a proportion of the spin have relaxed back to align with the z-axis. By varying the time τ_1 the proportion of spin which are aligned with the z-axis changes. The longer τ_1 the higher the proportion of spins aligned and thus the signal intensity increases. Eventually, after a long relaxation period τ_1 the spins reach their equilibrium magnetisation again and the signal intensity detected by NMR reaches a plateau. By repeating the experiment in figure 2.1 at different values of τ_1 an NMR spectroscopist is able to measure the longitudinal relaxation rate, T_1, using the Bloch equations 2.79 to simulate the signal intensity recovered after a period, τ_1.

2.7.2 The BPP model

The classic paper by Bloembergen, Pound and Purcell (BPP) [65] describing a theoretical framework linking the random fluctuations in the local magnetic field caused by the dipolar fields of spins in motion in the sample. Importantly for this work, it describes how the relaxation reacts to changes in temperature.

In a solid random motions causes fluctuations in the local magnetic field. Such fluctuations are characterised by a time correlation function $G(t)$ which describes the relationship between average local magnetic field now and after a time t has passed. This in effect measures the rate of change of the local mag-

netic field. An unchanging or constant local magnetic field would have a high correlation over time whereas a random or rapidly fluctuating field would have a low correlation over time. In the BPP model it is assumed that the correlation starts high and then decays exponentially with time giving

$$G(t) \propto \exp\left(\frac{-t}{\tau_c}\right), \tag{2.80}$$

where τ_c is the correlation time which characterises how quickly the local magnetic field changes. A constant which is determined by the strength of the interaction causing the fluctuations in the magnetic field is omitted. However, our interest is in how effective these fluctuations in the magnetic field are at causing relaxation in a spin species with a arbitrary Larmor frequency. The condition for causing relaxation efficiently is that the frequency of the motion associated with the correlation function is close the Larmor frequency of the spin species. This can be done by calculating the spectral density of the correlation function which can be found by Fourier transforming the correlation function as follows

$$J(\nu) \propto \int_{-\infty}^{\infty} G(t)\exp(-\imath 2\pi\nu t), \tag{2.81}$$

where ν is the frequency which the motion is causing relaxation to take place in. In this work this frequency will be the proton Larmor frequency. Note that the constants from the correlation function and the Fourier transform have been left out. When the transform is performed with correlation function in equation 2.80 the spectral density becomes [59]

$$J(\nu) = \frac{2\tau_c}{1+(2\pi\nu\tau_c)^2}, \tag{2.82}$$

where ν and τ_c have the same meaning as in equations 2.80 and 2.81.

The correlation time τ_c which is characteristic of the motion causing the relaxation can be modelled as a thermally activated process with characteristic

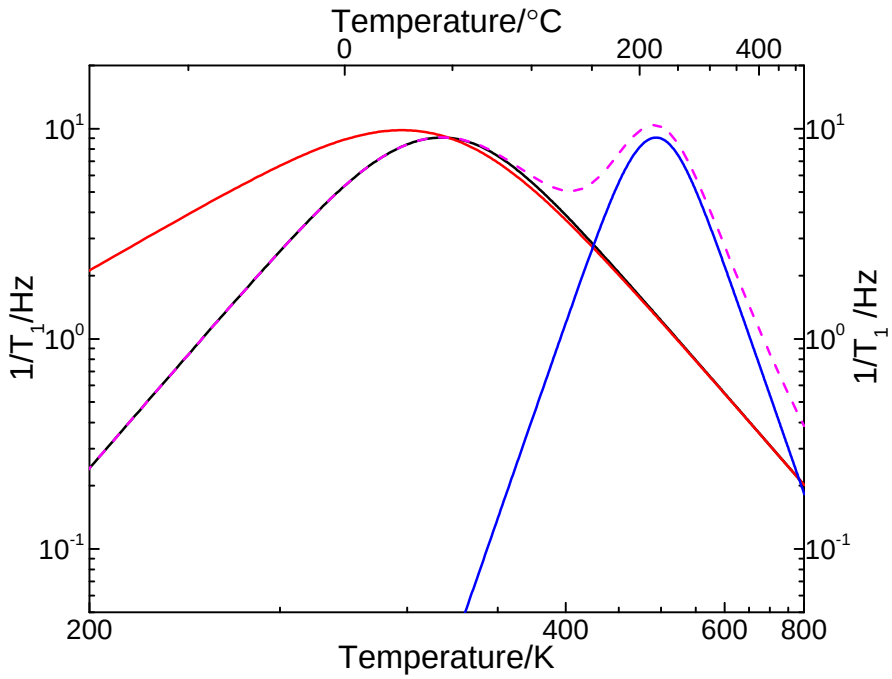

Figure 2.2: A plot of $\frac{1}{T}$ against $\log_{10}(\frac{1}{T_1})$ of the BPP model with $\tau_0 = 10^{-13}$ s and $E_a = 20$ kJ (black), stretched BPP model with $\beta = 0.5$ (red), standard BPP model with $\tau_0 = 10^{-15}$ s and $E_a = 50$ kJ (blue) and the two standard BPP models added together (magenta). In all cases $\nu_0 = 500$ MHz and $C = 10^8$ Hz.

activation energy E_a as follows

$$\tau_c = \tau_0 \exp\left(\frac{E_a}{RT}\right), \tag{2.83}$$

where τ_0 is the Arrhenius constant describing the motion, R is the gas constant and T is the temperature in Kelvin.

For a single and simple motion the NMR relaxation rate can be calculated from a linear superposition of the spectral densities. If the principal mechanism for relaxation is the homonuclear dipolar coupling between nuclei with spin $I = \frac{1}{2}$ as is the case for most proton relaxation rates in solids. Under such conditions the linear superposition needed to calculate the longitudinal relaxation rate becomes [59]

$$\frac{1}{T_1} = C\big[J(\nu_0) + 4J(2\nu_0)\big]. \tag{2.84}$$

where C is a constant representing the strength of the magnetic interaction between the species causing relaxation. In this work this is assumed to be the proton homonuclear dipolar coupling, d_{ij} (see section 2.6).

Combining equations 2.82-2.84 and plotting them as $\frac{1}{T}$ against $\ln\left(\frac{1}{T_1}\right)$ the energy barrier, E_a, of the thermally activated motion can be extracted. Such a plot of the BPP model is shown in figure 2.2.

In the case of proton self diffusion in a solid all the above conditions used in arriving to equation 2.84 are likely to be fulfilled. Since protons have a very large gyromagnetic ratio the dipolar coupling between protons is very strong and likely the dominant cause of relaxation. Furthermore, self diffusion is certainly a thermally activated motion and is a simple motion. Hence, all the conditions can be met.

2.7.3 Stretched Correlation Function

When the T_1 curve is not symmetrical around its maximum the standard BPP model is can no longer simulate the data accurately. In such cases it is necessary to modify the model to take into account this asymmetry. This can be done empirically by raising the exponential in the correlation function to power β as follows

$$G(t) \propto \exp\left(\frac{-t}{\tau_c}\right)^{\beta}. \tag{2.85}$$

This type of empirical modification has a rich history in NMR and specifically for simulating T_1 behaviour as a function of temperature [66, 67]. When a Fourier transform is performed on this type of correlation function the numerator of spectral density is changed from being squared to instead being raised to the power of $1+\beta$ as follows

$$J(\nu) = \frac{2\tau_c}{1+(2\pi\nu\tau_c)^{1+\beta}}. \tag{2.86}$$

The effect of this change to the spectral density can be seen in figure 2.2.

The model is no longer symmetrical about the maximum. Instead when the stretched correlation function is used the slope on of the curve is different on the high and low temperature side of the maximum.

Comparing the stretched model to the normal model with identical parameters, it is clear that the slope on the high temperature side of the maximum is the same. However, on the low temperature side the slope is gentler in the stretched model with $\beta = 0.5$ than in the standard BPP model.

2.7.4 Multiple Correlated Motions

There are occasions when several particle motions contribute significantly to the T_1 relaxation. In this work we will observe two independent maxima for the T_1 relaxation similar to the example in figure 2.2. Such cases can be modelled by allowing spin exchange between phases with different motion and therefore T_1 relaxation. Generally, a system with k relaxation conditions results in k coupled differential equations which take the form as follows

$$\frac{dI_{ij}(t)}{dt} = -\frac{I_{ij}(t)}{T_1^j} - \frac{I_{ij}(t)}{\tau_j} + \sum_k \frac{I_{ik}(t)}{\tau_{kj}} p_{kj}, \tag{2.87}$$

where $I_{ij}(t)$ is the probability of a spin starting in the i phase being in the j phase a time t later while not being relaxed to the z axis. τ_j is the mean residency time of the j phase while p_{kj} is the conditional probability that a spin in phase k moves to phase j T_1^j represents the possibility of T_1 relaxation in the j phase. This equation is very similar to the classic Bloch equation for the T_1 relaxation except we have allowed the magnetisation to move between areas with different relaxation conditions.

In this work we will encounter relaxation where there appears to be two phases. Solving equation 2.87 for two phases leads to a very long equation which can be seen written out several places [61, 68]. We will focus on the limiting cases which are used in this work. The first of these is when the exchange between phases is very high i.e. $\tau_j, \tau_{kj} \ll T_1^j$. In this case we observe only the

average relaxation

$$\frac{1}{T_1^{av}} = \frac{I_1}{T_1^1} + \frac{I_2}{T_1^2} \tag{2.88}$$

where T_1^1 and T_1^2 is the relaxation experienced in phases 1 and 2 while I_1 and I_2 are the probabilities of finding a particle in phase 1 and 2 respectively. This becomes more interesting when it is combined with the BPP model we have seen in section 2.7.2 as the relaxation in each phase is caused by a different characteristic motion τ_c which means that it is possible to have the relaxation from different phases dominate at different temperatures. This is illustrated in figure 2.2. Such a model has also been used previously to model the relaxation of protons in gelatin based conductors [47].

The other limiting case we shall concern ourselves with is slow exchange when the exchange between phases is much slower than the relaxation i.e. $\tau_j, \tau_{kj} \gg T_1^j$. In this case we observe several different relaxation constants simultaneously in the saturation recovery which leads to the following relationship with two phases

$$I_z(t) = I_1\left(1 - \mathrm{e}^{-t/\mathrm{T}_1^1}\right) + I_2\left(1 - \mathrm{e}^{-t/\mathrm{T}_1^2}\right), \tag{2.89}$$

where $I_z(t)$ is the magnetisation along the z-axis with two different relaxation constants T_1^1 and T_1^2 while I_1 and I_2 is the probability of finding the particle in phase 1 and 2. Naturally, there are intermediate cases which have been explored in detail by Wennerstrstöm [69]. It should be noted that a very similar model in used for commonly used for diffusion and this is discussed in section 2.10.4.

2.8 Transverse Relaxation

In addition to the T_1 relaxation, there is another type of relaxation termed *transverse* or *spin-spin* relaxation which is labelled T_2. This type of relaxation is best understood using the spin vector model for NMR. As explained in section 2.3, it is possible using RF pulses to generate coherent magnetisation in the x-y plane

which precesses around the z-axis. In an ensemble of spins, this magnetisation initially is all pointing in the same direction i.e. it is in phase. However, over time as the spins precess around the z-axis the phase of the spins in the ensemble start to differ from one another and the magnitude of the magnetisation in the x-y plane decreases until it eventually is reduced to zero. This phenomenon is called *spin decoherence* and the rate by which this happens is transverse T_2 relaxation. Magnetisation which is no longer coherent is called incoherent magnetisation.

A perfectly relaxed spin ensemble which is rotated by a 90°-pulse into a coherence in the x-y plane and which has no other interactions affecting it can be described as follows

$$\begin{aligned} M_x(t) &= M_{eq} \sin(\omega_0 t) e^{-t/T_2} \\ M_y(t) &= M_{eq} \cos(\omega_0 t) e^{-t/T_2}. \end{aligned} \tag{2.90}$$

The observed transverse relaxation rate is defined as period of time it takes for the magnetisation to the decay to $1/e$ of the original intensity. In the case of a lorentzian lineshape this turns out to be

$$T_2^* = \frac{1}{\pi\Omega}. \tag{2.91}$$

where Ω is the width of the resonance at half height and T_2^* is the observed transverse relaxation rate.

The causes of incoherent magnetisation leading to the overall observed transverse relaxation T_2^* can be separated into two groups. They are differentiated by whether the relaxation can be refocused by the spin echo experiment explained in section 2.8.1. Relaxation which can be refocused by a spin echo is termed inhomogeneous broadening and is labelled T_2. Relaxation which cannot be refocused by a spin echo is termed homogeneous broadening and labelled $T_2^{'}$. The relationship between these quantities is

$$\frac{1}{T_2^*} = \frac{1}{T_2} + \frac{1}{T_2^{'}} \tag{2.92}$$

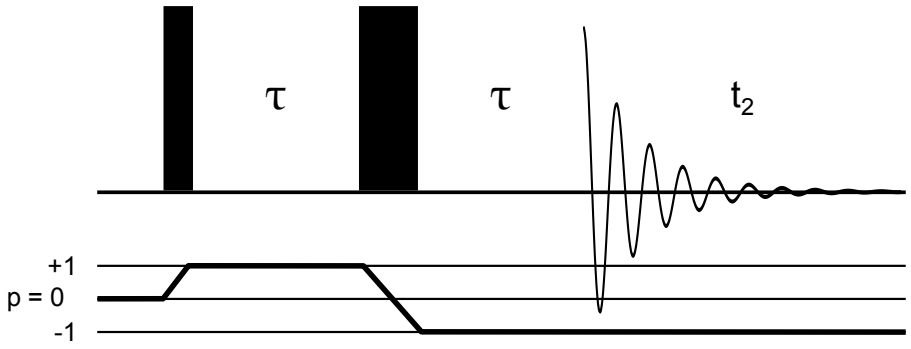

Figure 2.3: The pulse sequence and coherence transfer pathway for a spin echo experiment. The rectangles represent RF pulses with the first narrow rectangle being a 90°-pulse and the second broader rectangle a 180°-pulse.

The T_2^* term includes such factors as imperfect apparatus and nuclear spin interactions such as multiple spins coupled by homonulcear dipolar coupling and heteronucealar coupling not removed by ^{1}H decoupling.

2.8.1 The Spin Echo

The pulse sequence and coherence transfer pathway for a spin echo experiment is shown in figure 2.3. This experiment was first described by Hahn in 1950 [70]. It consists of an initial 90°-pulse to rotate the magnetisation from the z-axis into the x-y plane. Thereafter a period, τ, of free precession is allowed wherein spins precess around the z-axis at their characteristic frequency ν_0. A 180°-pulse is then applied which flips spins to their opposite. Another period of free precession is then allowed. However, during this period the spins rotate around the z-axis in the opposite direction than the first period due to the 180°-pulse. Therefore when the acquisition is started after the period τ the magnetisation is back to the state it had right after the initial 90°-pulse.

The spin echo has many other interesting properties which makes it a very widely used NMR experiment. For resonances which are very broad and consequently dephase rapidly a spin echo can be used to overcome the signal loss and phase problems associated with the dead-time after a RF pulse before acquisition can be started.

2.9 Quadrupole Coupling

Three quarters of all spin active nuclei possess a spin I greater than $1/2$. Such nuclei are called *quadrupolar* as they exhibit a property termed the *quadrupole moment*. Quadrupolar nuclei can interact with the electric field gradient which is inherently present around every nuclei unless the distribution of nearby electrons and nuclei exhibits cubic symmetry. Such nuclei make up approximately 74% of all nuclei with a magnetic moment. They occur in a huge variety of compounds from organic molecules through enzymes and inorganic minerals and crystals are almost entirely made up of atom with a quadrupolar moment. Combined with the extraordinary wealth of information available from the the quadrupole moment when interacting with its surroundings make quadrupolar nuclei incredibly useful when studying materials using NMR. However, as we shall see the same wealth of information in the quadrupolar interaction also makes it very complicated to study.

The quadrupole moment of a nucleus arises because of the symmetry of the charge distribution within itself. This charge distribution can be described in terms of multipoles where the zeroth-order multipole is the charge of nucleus which all nuclei possess. The first-order multipole is also called the dipole moment which all nuclei with spin $I \geq 1/2$ have. The second-order multipole is called the quadrupolar moment which all nuclei with spin $I > 1/2$ possess in addition to the dipolar moment. This nuclear charge distribution is inherent for each type of nucleus and does not change depeding on the chemical environment. The electric quadrupole moment of a nucleus is usually given as eQ, where e is the elementary charge charge.

This intrinsic quadrupole moment interacts with the electric field gradient. The electric field gradient is dependent on the geometry of the local environment i.e. the placement of nuclei and electrons in bonds as well as any symmetry these exhibit. It follows that the electric field gradient varies depending on the molecular orientation relative to the applied magnetic field, $\mathbf{B_0}$. Consequently the strength of quadrupole interaction is likewise dependent on the molecular orientation. This quadrupole interaction changes the nuclear energy levels in

addition to the Zeeman and dipolar interactions discussed earlier.

When the Zeeman interaction is on the order of 10 times larger than the quadrupole interaction the latter can be treated using perturbation theory to show how the nuclear energy levels are affected and consequently the impact on the NMR spectrum of a quadrupolar nucleus.

2.9.1 The Quadrupole Hamiltonian

The quadrupole Hamiltonian which describes the interaction between the quadrupole moment of nucleus of spin $\mathbf{I}$ and the electric field gradient $\mathbf{V}$ can be written in its most simple form as follows in units of angular frequency (rad s^{-1}) [60, 71]

$$\hat{\mathscr{H}}_Q = \frac{eQ}{2I(2I-1)\hbar}\hat{\mathbf{I}} \cdot \tilde{\mathbf{V}} \cdot \hat{\mathbf{I}}, \tag{2.93}$$

where $\hat{\mathbf{I}}$ is the nuclear spin vector, $\tilde{\mathbf{V}}$ is the second rank tensor describing the electric field gradient, e is the elementary charge and Q is the nuclear quadrupole moment. In the principal axis frame (PAF) the electric field gradient $\mathbf{V}$ is a diagonal matrix with a trace of zero. These non-zero diagonal elements are conventionally used to define the parameters

$$eq = V_{zz}^{PAF} \quad \text{and} \quad \eta_Q = \frac{V_{xx}^{PAF} - V_{yy}^{PAF}}{V_{zz}^{PAF}}, \tag{2.94}$$

where η_Q is the *quadrupolar asymmetry parameter* and e the elementary charge. As the trace of the electric field gradient tensor is zero the *quadrupolar anisotropy* of this tensor is simply eq.

It can be shown that in the PAF the quadrupolar Hamiltonian can be described using only two elements of the irreducible spherical tensor as follows [59, 60]

$$\hat{\mathscr{H}}_Q^{PAF} = A_{2,0}^{PAF}\hat{T}_{2,0} + A_{2,\pm2}^{PAF}\hat{T}_{2,\pm2} \tag{2.95}$$

where

$$A_{2,0}^{PAF} = \sqrt{6}\frac{e^2qQ}{4I(2I-1)} \quad \text{and} \quad A_{2,\pm2}^{PAF} = \frac{e^2qQ}{4I(2I-1)}\eta_Q \tag{2.96}$$

and the spin spherical tensors accompanying these are

$$\hat{T}_{2,0} = \sqrt{\tfrac{1}{6}}(3\hat{I}_z^2 - \hat{\mathbf{I}}\cdot\hat{\mathbf{I}}) \quad \text{and} \quad \hat{T}_{2,\pm2} = \tfrac{1}{2}\hat{I}_\pm^2. \tag{2.97}$$

One can transform the quadrupolar Hamiltonian into the laboratory frame using rotation matrices through the spherical polar angles (θ, ϕ) as seen in section 2.6 for the dipolar Hamiltonian. This leads to complicated and extremely long equation which isn't relevant to this work but can found in many places [59, 60]. However, it has been shown that the quadrupole Hamiltonian leads to the Zeeman nuclear energy levels shifting. The first and second order energy of these shifts have been shown to be respectively [59, 72]

$$\begin{aligned} E_m^{(1)} &= \frac{e^2qQ}{4I(2I-1)\hbar}\big[3m^2 - I(I+1)\big]\tfrac{1}{2}\big[(3\cos^2\theta - 1) \\ &\quad +\eta_Q\cos 2\phi\sin^2\theta\big] \end{aligned} \tag{2.98}$$

$$\begin{aligned} E_m^{(2)} &= -\left(\frac{e^2qQ}{4I(2I-1)\hbar}\right)^2\frac{m}{\omega_0}\big\{-\tfrac{1}{5}\big(I(I+1)-3m^2\big)\big(3+\eta_Q^2\big) \\ &\quad +\tfrac{1}{28}\big(8I(I+1)-12m^2-3\big)\big[(\eta_Q^2-3)(3\cos^2-1)+6\eta_Q\sin^2\theta\cos 2\phi\big] \\ &\quad +\tfrac{1}{8}\big(18I(I+1)-34m^2-5\big)\big[\tfrac{1}{140}(18+\eta_Q^2)(35\cos^4\theta - 30\cos^2\theta + 3) \\ &\quad +\tfrac{3}{7}\eta_Q\sin^2\theta(7\cos 2\phi - 1)\cos 2\phi + \tfrac{1}{4}\eta_Q^2\sin^4\theta\cos 4\phi\big]\big\}. \end{aligned} \tag{2.99}$$

where I is the nucelar spin quantum number with $2I+1$ energy levels labelled m rangeing in integer steps from $-I$ to I.

There are a few points of relevance to make with respect to these equations. The size of the perturbation to the Zeeman nuclear energy states is different for each. This means that the nuclear energy levels are not equally spaced any more and in principle each has it own characteristic frequency. Furthermore, it can be that the angular dependency of the first order perturbation has

two terms of which one is different to that seen in dipolar coupling. This means the quadrupole lineshape caused by this angular dependency cannot be completely removed by magic angle spinning.

There is one important exception to the above energy shifts and broadening by the quadrupole Hamiltonian. For any half-integer quadrupolar nucleus, such as $I = \frac{5}{2}$ for ^{17}O in this work, the first order perturbation to the transition energy between states $+\frac{1}{2} \rightarrow -\frac{1}{2}$ is zero. This means that this transition gives rise to a narrow resonance unless the quadrupole coupling is so large that the second order perturbation becomes significant. The resonance caused by this transition is so important it has been named the *central transition*. This is the transition which is observed in the ^{17}O spectra in this work and without this narrow resonance the low gyromagnetic ration and natural abundance such spectra would not have been possible.

When the quadrupole interaction is strong enough the second order perturbation can also be detected in the NMR spectrum. The size of the second order perturbation depends inversely on the Larmor frequency ($1/\omega_0$) which means that by going to higher magnetic fields one can reduce the magnitude of this energy perturbation. It is peculiar as it not only broadens the resonance from a transition anisotropically it also has an isotropic component. This means that the isotropic chemical shift measured shifts to a different chemical shift when measured at different magnetic field strengths.

The effect of RF pulses

We now turn to the effect of the quadrupolar coupling on the radio frequency pulses used to manipulate spins. It has been shown that when the quadrupolar coupling strength is much larger than the nutation frequency $\omega_Q \gg \omega_1$ then the effective flip angle caused by the RF field which the nucleus experiences changes to [73, 74]

$$\theta_Q = W_m \omega_1 \tau \tag{2.100}$$

where

$$W_m = [I(I+1) - m(m+1)]^{1/2} \tag{2.101}$$

where I is the nuclear spin quantum number and m represents the on resonance transition from nuclear energy level $m \rightarrow m+1$ and τ is the pulse length.

Resonances excited pulses in this regime where $\omega_Q \gg \omega_1$ thus experience a greater effective nutation frequency than they would were the quadrupole coupling absent. These are called soft pulses and in the case of half-integer nuclear spin often means that only the central transition is selectively excited. If on the other hand $\omega_1 \gg \omega_Q$ the RF pulses excite all transitions equally i.e. the satellite transitions will be seen as well. This is often called a hard or a non-selective pulse. Trouble occurs when there are multiple resonances with different quadrupole coupling strengths as this leads some resonances to experience a greater nutation frequency. This often makes it difficult to uniformly and optimally excite a spectrum with multiple resonances of the same quadrupole nucleus. Using small excitation angles θ_Q results in a more uniform flip angles and are thus often used when studying quadrupolar nuclei.

2.10 Diffusion and Magnetic Field Gradients

2.10.1 Fick's Laws

Diffusion traditionally describes the process of particles moving from an area of higher concentration to one of lower concentration also called particle flux and represented by **J**. This process was first explained by Adolf Fick in 1855 [75, 76]. Assuming the concentration of particles at a point **r** and at time t can be described by $n(\mathbf{r}, t)$ the flux of particles can be written as

$$\mathbf{J} = -D\nabla n(\mathbf{r}, t) \tag{2.102}$$

where D is a parameter known as the *diffusion coefficient* which describes the rate of diffusion at any given concentration. This relationship is called Fick's first law. To insure that this equation reflects reality we require that the total number of particles are conserved which means that the rate of change of the concentration $n(\mathbf{r}, t)$ with time is simply proportional to change or divergence of the flux

$$-\nabla \cdot \mathbf{J} = \frac{\partial n}{\partial t} \tag{2.103}$$

which when combined with Fick's first law leads to the following equation

$$\frac{\partial n}{\partial t} = D\nabla^2 n \tag{2.104}$$

where ∇^2 is the Laplace operator which applies a derivative with respect to the spatial coordinates twice. This equation is called Fick's second law and known as the diffusion equation.

Fick's equations of diffusion were originally developed to describe the phenomenon of *mutual diffusion* where a counter-current of different particles maintain overall mass density. This is typically the case for two liquids or gasses mixing. However, the same framework may be used to describe molecular movement in liquid comprising a single molecule as well as the Brownian motion of particles suspended in a liquid with no concentration gradients. This is called self diffusion.

2.10.2 Magnetic Gradient Fields

We now wish to add an additional magnetic field on top of the static $B_0\hat{\mathbf{k}}$ which we already discussed gives us the Zeeman Hamiltonian and the Larmor frequency in section 2.1.1. This additional magnetic field is a gradient magnetic field $\mathbf{B}(\mathbf{r})$ which varies spatially across the sample and is added the existing field $B_0\hat{\mathbf{k}}$. This is done such that the strength of the field is zero near the centre of the sample but the local gradient of the sample is $\nabla\mathbf{B}(\mathbf{r})$. The total magnetic field

$\mathbf{B_{tot}}$ can therefore be expressed as follows

$$\begin{aligned}\mathbf{B}_{tot}(x,y,z) &= B_0\hat{\mathbf{k}} + \mathbf{r}\cdot\nabla\mathbf{B}(\mathbf{r}) \\ &= (\mathbf{r}\cdot\nabla B_x)\hat{\mathbf{i}} + (\mathbf{r}\cdot\nabla B_y)\hat{\mathbf{j}} + (B_0 + \mathbf{r}\cdot\nabla B_z)\hat{\mathbf{k}}\end{aligned}$$

Spins do not care which direction $\mathbf{B}_{tot}(x,y,z)$ faces but takes the local direction as its quantisation axis for its Larmor frequency which is proportional to the magnitude of $\mathbf{B}_{tot}$

$$\omega_0 = \gamma|\mathbf{B}_{tot}|. \tag{2.105}$$

When we evaluate $|\mathbf{B}_{tot}|$ by expanding its terms while assuming that the primary field $B_0 \gg B(\mathbf{r})$ we get the following

$$\begin{aligned}|\mathbf{B}_{tot}| &= [(\mathbf{r}\cdot\nabla B_x)^2 + (\mathbf{r}\cdot\nabla B_y)^2 + (B_0 + \mathbf{r}\cdot\nabla B_z)^2]^{1/2} \\ &\approx B_0 + \mathbf{r}\cdot\nabla B_z + \frac{1}{2}B_0^{-1}[(\mathbf{r}\cdot\nabla B_x)^2 + (\mathbf{r}\cdot\nabla B_y)^2 + (\mathbf{r}\cdot\nabla B_z)^2]^{1/2} \\ &\approx B_0 + \mathbf{r}\cdot\nabla B_z. \end{aligned}\tag{2.106}$$

It can be seen that all the components of the gradient field involving B_x and B_y no longer contribute to the gradient field. This means one can use coils which produce only three gradient components $\delta B_x/\delta z$, $\delta B_y/\delta z$ and $\delta B_z/\delta z$. In fact one can substitute

$$\mathbf{G} = \nabla B_z \tag{2.107}$$

such that the Hamiltonian becomes

$$\begin{aligned}\hat{\mathscr{H}} &= \hat{\mathscr{H}}_z + \hat{\mathscr{H}}_G \\ &= \gamma\,(B_0 + \mathbf{r}\cdot\mathbf{G})\,\hat{I}_z. \end{aligned}\tag{2.108}$$

We will now consider the effect of applying a constant gradient field following a 90°_x-pulse. In section 2.3.1 it was shown that such a pulse generates $-\hat{I}_y$

magnetisation which under the influence of the Zeeman Hamiltonian evolves into equation 2.46 The evolution of the $-\hat{I}_y$ magnetisation under the Hamiltonian including gradient field as well follows a very similar route

$$\begin{aligned}\hat{\rho}(t) &= e^{-\imath(\omega_0+\gamma\mathbf{r}\cdot\mathbf{G})t\hat{I}_z}(-\hat{I}_y)e^{\imath(\omega_0+\gamma\mathbf{r}\cdot\mathbf{G})t\hat{I}_z} \\ &= -\hat{I}_y\cos(\omega_0+\gamma\mathbf{r}\cdot\mathbf{G})t+\hat{I}_x\sin(\omega_0+\gamma\mathbf{r}\cdot\mathbf{G})t. \qquad (2.109)\end{aligned}$$

The observed signal following the gradient field can be calculated by going into the rotating frame using the operator $N\gamma[\hat{I}_x+\imath\hat{I}_y]$ using the same steps seen in section 2.3.1 which yields the following

$$\begin{aligned}M_+(\mathbf{r},t) &= Tr(N\gamma[\hat{I}_x+\imath\hat{I}_y]\hat{\rho}(t)) \\ &= \imath M_{eq}\exp(-\imath(\omega_0-\omega_{obs}+\gamma\mathbf{r}\cdot\mathbf{G})t) \\ &= M_+(\mathbf{r_0},0)\exp(-\imath\gamma\mathbf{r}\cdot\mathbf{G}t) \qquad (2.110)\end{aligned}$$

where $M_+(\mathbf{r_0},0)$ is identical to the expression observed in equation 2.50 describing an observed resonance at ω_0. It is important to note that the effect of $\exp(-\imath\gamma\mathbf{r}\cdot\mathbf{G}t)$ then is to make the Larmor frequency slightly higher or slower depending on the affected spins position. This is equivalent to adding a phase the Larmor frequency of the spins the magnitude of which is dependent on where in the sample the spins are located as well as how long the gradient field is active. This special behaviour of the phase is called an isochromat. If one applies a linear gradient G in along the z axis the subsequent evolution over time is

$$M_+(z,t)=M_+(z,0)\exp(-\imath\gamma zGt). \qquad (2.111)$$

This equation tells us that the isochromat forms a helical phase as one travels along the z axis at a fixed time. This leads to a very informative way of visualising the effect on the Larmor frequency of the gradient field by considering the path length along the z axis one must travel for the phase acquired by the

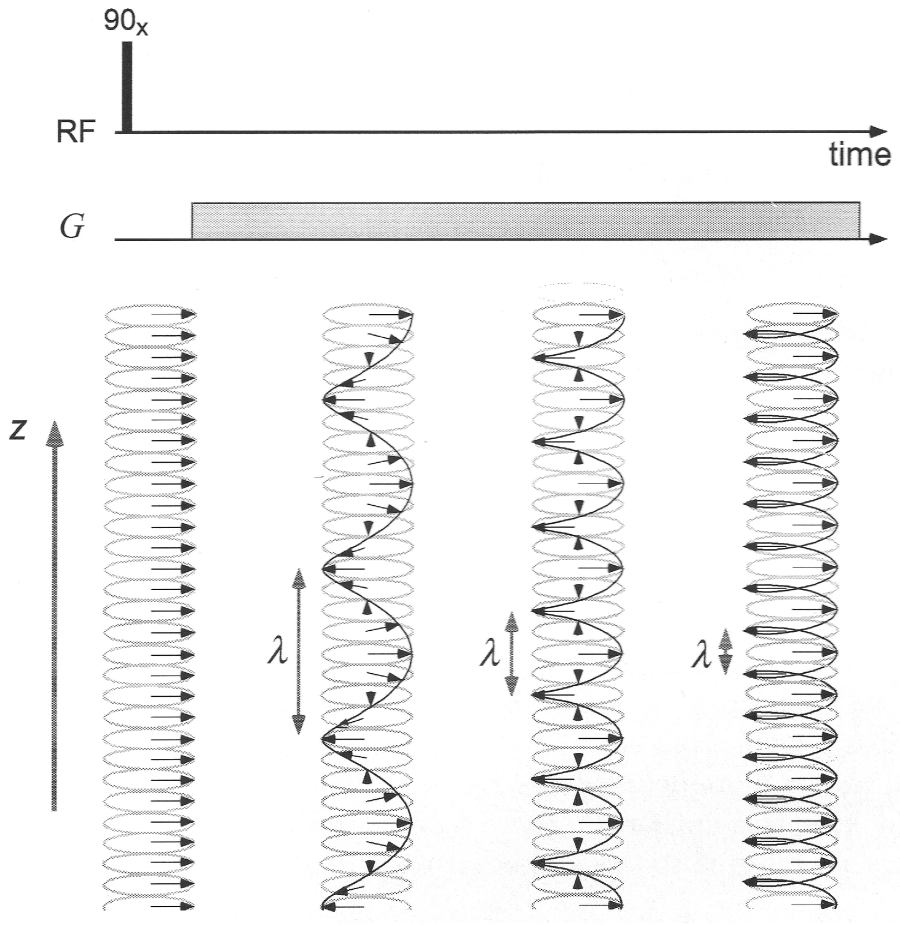

Figure 2.4: The evolution of the phase along the z axis under a magnetic gradient field G following a 90°_x-pulse. Immediately after the rf pulse the phase is the same for every spin along the z-axis. As time progresses the phase evolves into a helix along the z axis. Copied from [61].

spins to be equal to a full rotation or 2π

$$\lambda = \frac{2\pi}{\gamma G t} \tag{2.112}$$

where λ is the path length along the z axis between a full rotation around the helix. This leads to a spatial differentiation of the Larmor frequency which either becomes slightly greater or smaller depending on the position of the contributing spins as can be seen in figure 2.4. This property is commonly used in Magnetic Resonance Imaging using gradient coils in three dimensions. Detailed discussion of this topic is however outside the scope of this thesis.

2.10.3 Diffusion in a Gradient Field

Until now our discussion of magnetic field gradients have implicitly assumed that the spins which are observed have been stationary throughout the gradient pulse. This assumption is both correct and useful when considering imaging techniques. However, we wish to consider the effect of a gradient field on a moving particle in the gradient field. We must acknowledge that a moving particle will experience a different magnetic gradient field whenever it changes position. This means that such a moving particle will experience an additional change in phase compared to what a stationary particle will experience. The key to understanding how a magnetic gradient field then is two fold. First we must be able to calculate the phase difference between a moving and a stationary particle even if they start in the same position and how it relates to the particle movement. Second, we must under experimental conditions be able to remove the phase acquired by stationary spins due to the magnetic gradient field in order to isolate the extra phase acquired due to movement.

The second condition turns out to be the simplest to solve as we have experimental control over whether the spins acquire phase by having a frequency slightly higher or lower than the Larmor frequency in absence of a magnetic gradient field. This is practically done using either a 180°-pulse between two identical gradient pulses or two gradient pulses where one is applied along the z axis while the the second is applied along the $-z$ axis. In both cases the phase helix shown in figure 2.4 is unwound. This can be expressed mathematically if we require the sum of the magnetic gradient field with time to be equal to zero which can be expressed as the following integral [61]

$$\int_0^t \mathbf{G}(t')dt' = 0, \tag{2.113}$$

where $\mathbf{G}(t)$ refers to magnetic gradient which changes over time. Note that the change to $\mathbf{G}(t)$ is done to indicate that an echo is formed at acquisition and the above condition is kept.

The simplest experiment using this condition to investigate diffusion is

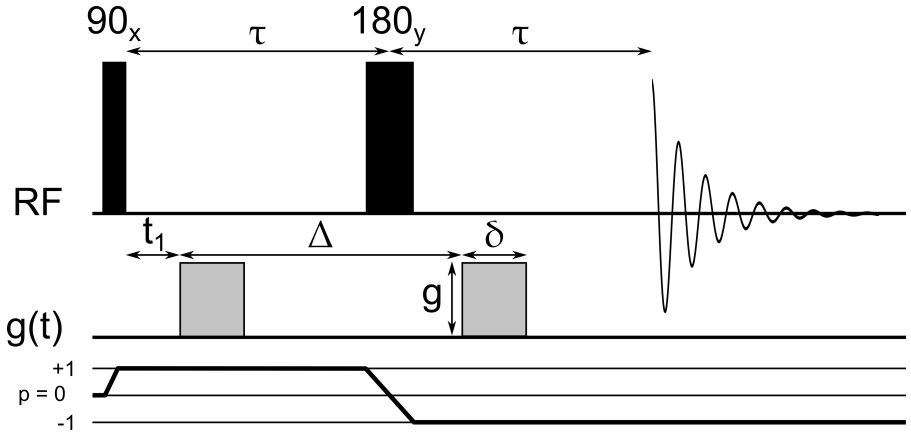

Figure 2.5: The pulse sequence and coherence transfer pathway for a pulsed gradient spin echo (PGSE) experiment. In this figure the narrow black rectangle is a 90°_x-pulse and the wide black rectangle is a 180°_y-pulse. The grey rectangles represent magnetic gradient field pulses of length δ, a diffusion time Δ and $\mathbf{g}$ is the strength of the magnetic gradient field.

the pulsed gradient spin echo (PGSE) which was first proposed by Stejskal and Tanner [51]. In figure 2.5 the pulse sequence and coherence pathway for a PGSE experiment can be seen. In this experiment a two constant gradients g is applied for a length δ on either side of a 180°-pulse where after an echo is recorded at 2τ. This ensures that the resonances will only acquire phase if the spins giving rise to the resonances are diffusing. To establish how the length of the magnetic gradient affects the spins we first differentiate equation 2.111 with respect to time

$$\frac{\partial M_+(\mathbf{r},t)}{\partial t} = -\imath\gamma\mathbf{r}\cdot\mathbf{G}M_+(z_0,t)\exp(\imath\gamma\mathbf{r}\cdot\mathbf{G}t) \tag{2.114}$$

$$= -\imath\gamma\mathbf{r}\cdot\mathbf{G}M_+(\mathbf{r},t). \tag{2.115}$$

Equation 2.115 can be integrated as an differential equation

$$\int_{M_0}^{M_+}\frac{\partial M}{M} = \int_0^t -\imath\gamma\mathbf{r}\cdot\mathbf{G}\partial t' \tag{2.116}$$

$$\ln M|_{M_0}^{M_+} = -\imath\gamma\mathbf{r}\cdot\int_0^t \mathbf{G}(t')\partial t \tag{2.117}$$

$$M_+ = M_0\exp(-\imath\gamma\mathbf{r}\cdot\mathbf{F}(t)) \tag{2.118}$$

where

$$\mathbf{F}(t) = \int_0^t \mathbf{G}(t')\partial t \tag{2.119}$$

The above equation describes how for a given time varying gradient affects the magnetisation. We then incorporate diffusion into these equitations by applying Fick's law as we have seen it in section 2.104 and treating the coherence M_+ as a diffusing entity

$$\frac{\partial M_+(\mathbf{r},t)}{\partial t} = D\nabla^2 M_+(\mathbf{r},t) \tag{2.120}$$

In combination with equation 2.115 this yeilds the master equation which needs to be solved

$$\frac{\partial M_+(\mathbf{r},t)}{\partial t} = -\imath\gamma\mathbf{r}\cdot\mathbf{G}M_+(\mathbf{r},t) + D\nabla^2 M_+(\mathbf{r},t) \tag{2.121}$$

This equation is called the Bloch-Torrey equation and was first proposed by Torrey in 1956 [77]. Relaxation terms can be included in this equation but they to not change the final dependence of the magnetisation on the magnetic gradient field and therefore it will be omitted for simplicity. We have already seen that without any diffusion equation 2.118 is a solution to the Bloch-Torrey equation. The full solution is likely related to this partial solution. However, before continuing we must make a few modifications. The magnitude of the transverse relaxation M_0 is replaced by $M_0(t)$ such that immediately following the initial 90°-pulse is $M_+(\mathbf{r},0) = M_0(0)$. Furthermore, due to the 180°-pulse the magnetisation precession changes direction half way through the experiment. This changes the sign of the phase which is acquired due to the magnetic gradient. This can be incorporated into our proposed solution by considering the coherence order p which changes from $p = +1$ to $p = -1$ after the 180°-pulse. Thus we replace $\mathbf{F}(t)$ with $\mathbf{F}(t)p$ where p takes the value $+1$ from $0 \leq t < \tau$ and -1 from $\tau \leq t < 2\tau$ [61, 78, 79]. Thus our final proposed solution is

$$M_+(\mathbf{r},t) = M_0(t)\exp(-\imath\gamma\mathbf{r}\cdot\mathbf{F}(t)p) \tag{2.122}$$

The above solution is then tested by inserted into the Bloch-Torrey equation and differentiated with respect to time

$$\frac{\partial M_+(\mathbf{r},t)}{\partial t} = \left[\frac{\partial M_0(\mathrm{t})}{\partial t} - \imath\gamma\mathbf{r}\cdot\frac{\partial \mathbf{F}(t)p}{\partial t}M_0(\mathrm{t})\right]\exp(-\imath\gamma\mathbf{r}\cdot\mathbf{F}(t)p) \tag{2.123}$$

remembering that

$$\frac{\partial \mathbf{F}(t)}{\partial t} = \mathbf{G}(t). \tag{2.124}$$

The proposed solution in equation 2.122 is differentiated with respect to the Laplace double derivative of the spacial vector $\mathbf{r}$

$$\begin{aligned} D\nabla^2 M_+(\mathbf{r},t) &= DM_0(t)\nabla^2\exp(-\imath\gamma\mathbf{r}\cdot\mathbf{F}(t)p) \\ &= -DM_0(t)\left[\gamma\mathbf{F}(t)p\right]^2\exp(-\imath\gamma\mathbf{r}\cdot\mathbf{F}(t)p). \end{aligned} \tag{2.125}$$

The latter equation is then substituted into the Bloch-Torrey equation

$$\frac{\partial M_+(\mathbf{r},t)}{\partial t} = -\left(\imath\gamma\mathbf{r}\cdot\mathbf{G} + D\left[\gamma\mathbf{F}(t)p\right]^2\right)M_0(t)\exp(-\imath\gamma\mathbf{r}\cdot\mathbf{F}(t)p) \tag{2.126}$$

Equating the Bloch-Torrey equations with respect to time and spatial derivative in equations 2.123 and 2.126 respectively

$$\begin{aligned} &\left[\frac{\partial M_0(\mathrm{t})}{\partial t} - \imath\gamma\mathbf{r}\cdot\mathbf{G}M_0(\mathrm{t})\right]\exp(-\imath\gamma\mathbf{r}\cdot\mathbf{F}(t)p) \\ &= -\left(\imath\gamma\mathbf{r}\cdot\mathbf{G} + D\left[\gamma\mathbf{F}(t)p\right]^2\right)M_0(t)\exp(-\imath\gamma\mathbf{r}\cdot\mathbf{F}(t)p) \end{aligned} \tag{2.127}$$

The above equation is then simplified by dividing both sides by the exponential and cancelling identical terms

$$\frac{\partial M_0(\mathrm{t})}{\partial t} = -D\left[\gamma\mathbf{F}(t)p\right]^2 M_0(t) \tag{2.128}$$

This differential equation can easily be solved to give

$$\int_{M_0(0)}^{M_0(2\tau)} \frac{dM_0(t)}{M_0(t)} = -D\gamma \int_0^{2\tau} [\mathbf{F}(t)p]^2 \, dt \tag{2.129}$$

which for the PGSE sequence evaluates into the Stejskal-Tanner equation

$$\frac{M_0(2\tau)}{M_0(0)} = \exp[-D\gamma^2 g^2 \delta^2 (\Delta - \delta/3)] \tag{2.130}$$

where the parameters δ, Δ and g are under experimental control and increasing any one of these modulates the original signal by an exponential attenuation. This makes the Stejskal-Tanner a function of $M_0(\delta, \Delta, g)$. However, in practice when determining a diffusion coefficient D only g is varied while δ and Δ are kept constant. This results in the experiment becoming time constant as the attenuation of the magnetisation is determined as a function of g. This has the advantage that every experiment experiences the same amount of relaxation and so does not affect the attenuation of the experiment. This also justifies the choice not to include relaxation in the Bloch-Tanner equation.

The step between equations 2.129 and 2.130 is achieved by considering the differential equation between these discrete time intervals where the magnetic gradient strength can be directly read from figure 2.5

$$\mathbf{G}(t) = \begin{cases} 0, & 0 < t < t_1 \\ g, & t_1 < t < t_1 + \delta < \tau \\ 0, & t_1 + \delta < t < t_1 + \Delta \\ g, & t_1 + \Delta < t < t_1 + \Delta + \delta < 2\tau \\ 0, & t_1 + \Delta + \delta < t \end{cases}$$

The evaluation of these integrals can be found both in the original paper by Stejskal and Tanner [51] as well as later publications [61, 78, 79]. It should also be noted that due to this treatment, equation 2.129 is in fact a completely general solution where one only needs to use different time intervals and gradient strengths in order to calculate the attenuation factor comparable to the

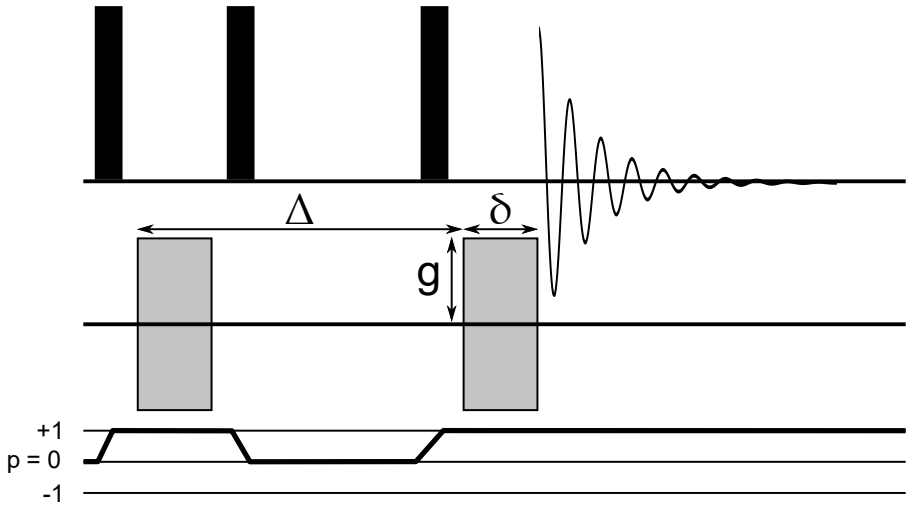

Figure 2.6: The pulse sequence and coherence transfer pathway for a stimulated echo pulsed field gradient (STE-PFG). In this figure the black rectangles represent 90°-pulses and gray rectangles represent gradient pulses where δ is the length of the gradient pulse, Δ is the diffusion time and **g** is the maximum gradient strength.

Stejskal-Tanner equation but for another arrangement of gradient pulses.

Diffusion experiments in this work have not been performed using the PGSE sequence but the stimulated echo pulsed field gradient (STE-PFG) experiment shown in figure 2.6. This experiment was introduced by Tanner in 1970 [80] and is very similar to PGSE except a single 180°-pulse has been replaced by two 90°-pulses which does cause the STE variant to have an automatic factor of 2 less signal. For the purposes of measuring diffusion this arrangement of radio frequency pulses yields the same Stejskal-Tanner equation for the attenuation of transverse magnetisation. The main benefit of the STE pulse sequence is that magnetisation is stored along the z axis during the diffusion time Δ which means the magnetisation is not affected by T_2 relaxation during this time. This is very valuable when samples are solid as strong dipolar coupling makes T_2 relaxation very fast and thus overall one achieves an increase in signal magnitude by using a STE sequence over SE.

2.10.4 Two Region Exchange and Diffusion

Often diffusion is not uniform across a whole material but over the course of the duration of the PFG experiment the diffusion many times averages to a single diffusion coefficient. However, the situation also arises when diffusion occurs over several subregions which have different diffusion coefficients and the time-scale of the experiment is so short that these diffusing particles have not mixed sufficiently to average the signal detected by PFG NMR. This can be addressed by treating diffusion coefficient detected by the echo attenuation as a linear superposition of diffusion coefficients D_i for each subregion with a relative weighting P_i where $\sum_i P_i = 1$ [81, 82],

$$E(g,\Delta) = \exp(-\gamma^2\delta^2 g^2 \overline{D}\Delta) \tag{2.131}$$

where $E(g,\Delta)$ is the equivalent to $\frac{M_0(2\tau)}{M_0(0)}$ in equation 2.130. This leads to the following coupled differential equations for a two region problem [82–85]

$$\frac{dE_1(g,t)}{dt} = -\gamma^2\delta^2 g^2 D_1 E_1(g,t) - \frac{E_1(t)}{\tau_1} + \frac{E_2(g,t)}{\tau_2} \tag{2.132}$$

and

$$\frac{dE_2(g,t)}{dt} = -\gamma^2\delta^2 g^2 D_2 E_2(g,t) - \frac{E_2(t)}{\tau_2} + \frac{E_1(g,t)}{\tau_1} \tag{2.133}$$

where τ_1 and τ_2 are the dwell times in regions 1 and 2 respectively. They represent the amount of time which the particle spends in each region.

Solving these differential equations with the initial conditions

$$E_{1,2}(g,0) = P_{1,2} \quad \text{and} \quad \left.\frac{dE_{1,2}(g,t)}{dt}\right|_{t=0} = -\gamma^2\delta^2 g^2 D_{1,2} \tag{2.134}$$

gives the following solution [82, 83]

$$E(g,\Delta) = a_1 \exp(\gamma^2\delta^2 g^2 D_1^{'}\Delta) - a_2 \exp(\gamma^2\delta^2 g^2 D_2^{'}\Delta) \tag{2.135}$$

where

$$D_1^{'}, D_2^{'} = \frac{1}{2}\Bigg\{D_1 + D_2 + \frac{1}{\gamma^2\delta^2 g^2}\left(\frac{1}{\tau_1} + \frac{1}{\tau_2}\right) \mp \left[\left(D_1 - D_2 + \frac{1}{\gamma^2\delta^2 g^2}\left(\frac{1}{\tau_1} - \frac{1}{\tau_2}\right)\right)^2 + \frac{4}{\gamma^4\delta^4 g^4 \tau_1 \tau_2}\right]^{1/2}\Bigg\} \quad (2.136)$$

and

$$a_1 = \frac{1}{D_2^{'} - D_1^{'}}[D_2^{'} - D_{av}] \quad (2.137)$$

$$a_2 = \frac{1}{D_2^{'} - D_1^{'}}[D_1^{'} - D_{av}] \quad (2.138)$$

where

$$D_{av} = P_1 D_1 + P_2 D_2 \quad (2.139)$$

These equations reduce to the well known and simple limiting cases. When $\Delta \gg \tau_1, \tau_2$ which means that the diffusion time is much longer than the time a particle spends in a given region before moving to the other. This means there is sufficient time to mix and average the diffusion of each region and we get that the attenuation of the resonance is the mono-exponential with an apparent diffusion coefficient as seen in equation 2.131 which is in fact the average diffusion coefficient as defined in equation 2.139 and therefore becomes

$$E(g, \Delta) = P_1 \exp(-\gamma^2\delta^2 g^2 (P_1 D_1 + P_2 D_2)\Delta). \quad (2.140)$$

Conversely if $\Delta \ll \tau_1, \tau_2$ then the particles have only been observed in a single region during the diffusion time and both diffusion coefficients are observed independently. In this case the attenuation of the resonance observed becomes a linear superposition of two exponentials with a pre-exponential weighting by the relative populations of each region

$$E(g, \Delta) = P_1 \exp(-\gamma^2\delta^2 g^2 D_1 \Delta) + P_2 \exp(-\gamma^2\delta^2 g^2 D_2 \Delta). \quad (2.141)$$

There is another less common set of conditions which we will need to use in this work which leads to different attenuation of the resonance. We will assume that there exits small regions with high diffusion such that $P_1 \ll P_2$ and $D_1 \gg D_2$ which simplifies the above equations to [61, 82]

$$E(g) = \exp(-\gamma^2\delta^2 g^2 \left[D_2 + \frac{P_1 D_1}{\gamma^2\delta^2 g^2 \tau_2 P_1 D_1 + 1} \right] \Delta). \tag{2.142}$$

This equation has been used to model defects between crystallites where one diffusion constant represents the intra-crystalline diffusion and the other inter-crystalline diffusion [86]. We will use this equation in both chapters 3 and 4 to simulate proton diffusion in a hybrid of a metal oxide framework and an organic polymer.

2.10.5 Pulsed Field Gradient NMR under MAS

In this work we determine the diffusion coefficient of samples using pulsed field gradient while simultaneously spinning the sample in a rotor at the magic angle to remove dipolar and chemical shift anisotropy. This is achieved using a standard narrow-bore probe and attaching a micro-imaging unit over the stator where the sample is spinning. This micro-imaging unit then applies a gradient field across the sample but instead of a gradient only along the z axis it is applied equally strong in all three spatial dimension such that

$$G_z = G_y = G_x. \tag{2.143}$$

This means that the gradient field which is normally orientated along the z-axis is now tilted at an angle of 54.74° to this axis and is coincident with the axis of the magic angle spinning. Diffusion is then measured along the magic angle which rotor spins around. This means that one can apply the exact same pulse sequences such as PGSE and STE-PFG previously described as the physical set up [87]. This experimental setup has been used to investigate lateral membrane diffusion of lipid bilayers [88] as well as proton diffusion in Si-MCM-41

functionalised with sulfate [58].

Chapter 3

Mesoporous Titanium Oxide Doped with Naphthalene Sulfonate Formaldehyde

3.1 Introduction

Nafion 117 is currently the commercial leader for proton exchange membranes due to its fast proton conductivity and mechanical stability. The current model for the proton conduction in Nafion is the channel model [31, 89, 90]. It holds that the hydrated Nafion membrane forms channels filled with water. The hydrophobic fluorinated backbone are pushed against one another to prevent contact with water whereas the hydrophilic sulfonate groups point into the channel. The water molecules then act as bridges between the sulfonate groups for protons to travel between as part as their diffusion. This arrangement is vulnerable to loss of water which effectively prevents the proton diffusion. Its has been shown that when the temperature is raised above 80 °C the conductivity of Nafion 117 is significantly reduced [53]. This is a problem for the platinum catalyst which breaks the bond to hydrogen and suffers from carbon monoxide poisoning when temperature is under 140 °C. However, as there is a large entropy contribution to the Gibbs free energy of carbon monoxide adsorption on

the platinum the carbon monoxide can be eliminated by raising the temperature above 140 °C [16, 91].

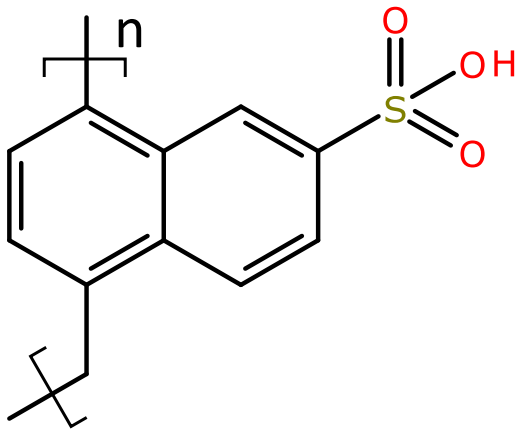

Figure 3.1: The structure of NSF with n naphthalene units each with a single acidic sulfonate group (-SO_3H) which can participate in a hydrogen bond network leading to proton diffusion.

Solid acid electrolytes without a liquid phase have therefore garnered significant attention [92]. These process proton diffusion without any physical movement of a vehicle such as water but rather by transferring protons between fixed hydrogen bonded sites [89]. This process is often referred to as the Grotthuss mechanism [27] and the transfers between hydrogen bonded sites as jumps. This is the environment which mesoporous metal oxides impregnated with naphthalene sulfonate formaldehyde (NSF) the structure of which is shown in figure 3.1. This was done in order to use the sulfate (-SO_4H) and sulfonate (-SO_3H) acids present to mediate proton diffusion without the presence of water mediating the proton diffusion. The pores in the metal oxide act as channels through which the protons can permeate. Sulfate is anchored to the surface of the pores by covalent bonds to increase the acidity as well as anchoring hydrogen bonding sites when raising the temperature. The impregnated NSF with an attached sulfonate group is postulated to be in close contact with the pore walls which can participate in the proton conduction with less thermal vulnerability to water evaporation. The aim being to create an environment where the acidic sites on the pore wall will bridge any gaps between sulfonate groups on NSF increasing the concentration of hydrogen bonding which participate in diffusion and thereby increasing its natural conductivity.

It has been shown that mesoporous titanium oxide impregnated with NSF resin using diethyl ether labelled mTiO_2(NSF)-DEE have better proton conductivity than Nafion 117 at 75 and 100 °C. However, when the temperature rises

above 125 °C the conductivity of both materials drop significantly [25]. However, it is unclear how proton diffusion happens at an atomic level and why proton conductivity drops when the temperature rises above 100 °C. Impregnating the NSF resin into the titanium oxide using water, $mTiO_2$(NSF)-H_2O, results in a significant reduction in proton conductivity compared to both Nafion 117 and $mTiO_2$(NSF)-DEE though the conductivity is greater than pure NSF resin [24]. Of particular interest is how the pores affect the proton diffusion in NSF. Does the pore surface participate in the diffusion or does it merely change the arrangement of NSF to increase diffusion and how does this affect the hydrogen bonding experienced by the diffusing protons?

Solid state NMR is uniquely suited to probe the hydrogen bonding which leads to proton diffusion at the atomic level [93,94]. Hydrogen bonding protons can be distinguished from other protons by their chemical shift using solid state NMR [33]. The motion of such protons affect the chemical shift and relaxation. The rates of T_1 and T_2 relaxation are affected differently by proton movement rates and thus the manner which the chemical shift and relaxation change with increases in temperature depends on the proton motion [33, 94]. Additionally, the rate of diffusion at the molecular level can be measured using pulsed field gradients (PFG) which when measured across a range of temperatures can be used to calculate the energy barrier to diffusion at a molecular level.

Therefore $mTiO_2$(NSF) samples were investigated using ^{1}H spin echoes to identify the chemical shifts of protons moving through the hydrogen bonded network and how it changes with temperature [38]. The dynamical nature of these protons was investigated using longitudinal relaxation T_1 [36, 47, 95, 96] and transverse relaxation T_2 [37,38,94] as well as PFG MAS [52,53,58]. These are each affected differently by proton motion and can be used to elucidate different aspects of proton motion which leads to diffusion.

3.2 Experimental Details

Materials

Mesoporous titanium oxide $mTiO_2$ impregnated with NSF resin were obtained from Jonathan P. Turley at the University of South Wales. The mesoporous titanium oxide was synthesised by Jonathan P. Turley using amines with linear carbon chains as templates [97]. This resulted in pore sizes of 20 Å [24] as measured by Barett-Joyner-Halenda (BJH) analysis [98] and can be seen in table 4.1. The NSF resin impregnated into the metal oxides has a molecular weight between 400 and 1000 g mol^{-1} corresponding to a resin chain length between 2 to 6 units [25, 99, 100]. The short chain length of the NSF resin allows for facile impregnation of the metal oxide pores. The pores of the titanium oxide were impregnated with NSF resin while in diethyl ether labelled $mTiO_2$-NSF-DEE or water labelled $mTiO_2$-NSF-H_2O [24]. All samples of $mTiO_2$(NSF) were center packed with a layer approximately 2 mm thick in 3.2 mm rotors. A layer of Teflon tape was put on either side of the metal oxides which isolated the samples from a layer of lead nitrate, $Pb(NO_3)_2$, at the top and bottom of the rotor. This was used used to determine the temperature of the samples in situ as the change in chemical shift of ^{207}Pb is proportional to the change in temperature [101–103]. Furthermore, this enabled the measurement of the temperature on both sides of the sample by measuring the chemical shift of the two resonances in the ^{207}Pb spectrum by taking their average. The temperature gradient across the sample [101] was estimated by calculating the difference between the chemical shift of the ^{207}Pb resonances.

Solid State NMR

All three samples were studied using ^1H saturation recovery MAS NMR and spin echo MAS NMR spectra which were acquired on a Bruker Avance III spectrometer operating at 11.75 T corresponding to a proton Larmor frequency of $\omega_0 = 500.10$ Hz. A Bruker 3.2 mm triple channel probe operating in dual channel mode was used and a MAS frequency of 10 kHz was achieved. The sequence

used to measure ^{1}H T_1 relaxation was a saturation recovery with spin echo acquisition $[\tau_S - \pi]_n - t_1 - \pi/2 - \tau_R - \pi - \tau_R -$ acquire. The length of the $\pi/2$ pulse is 2.5 μs while the π pulse is 5 μs and is used both in the saturation pulse train and the echo acquisition. The length of delay in the saturation pulse train is τ_S is 20 μs while the saturation train was repeated 151 times. The length of the echo delay is $1/\nu_R = \tau_R = 100$ μs. The length of the T_1 recovery delay was varied between in 32 steps between 1 μs and 10 s and at each delay 16 experiments were co-added. The recovery time of the spin echo MAS experiments were 10 s. Both saturation recovery and spin echo spectra were acquired every 10 °C between the temperatures of -30 °C and 120 °C. All the ^{1}H chemical shift are referenced to the ^{1}H solid reference of alanine at δ 1.3, 3.5 and 8.3 ppm which is a secondary reference to TMS at δ 0.0 ppm.

The samples of NSF and mTiO_2 NSF DEE were studied using ^{1}H stimulated echo pulsed field gradient under magic angle spinning (STE-PFG MAS) spectra which were acquired on a wide bore Bruker Avance III spectrometer operating at 17.62 T corresponding to a proton Larmor frequency of $\omega_0 = 750.0$ MHz. A narrow bore Bruker 3.2 mm dual channel probe was used and a MAS frequency of 20 kHz was achieved. The sequence used for the STE-PFG MAS with z-filtered acquisition $\pi/2 - \delta - \pi/2 - \Delta - \pi/2 - \delta - \pi/2 - \pi/2 - \tau_z - \pi/2 -$acquire. The length of all $\pi/2$ pulses was 2.5 μs. The diffusion times Δ of 50, 100, 200 and 400 ms were used and the length of the applied δ (field gradient pulse) was varied to keep overall attenuation constant across all diffusion times while keeping the maximum field gradient pulse at 600 G cm^{-1}. A recycle delay of 3 s was used. All the ^{1}H chemical shifts are referenced to the primary reference TMS at δ 0.0 ppm.

3.3 Proton Chemical Shift & Relaxation

3.3.1 Chemical Shift

Naphthalene Sulfonate Formaldehyde

In figure 3.2a is shown the ^{1}H spectra of pure NSF at temperatures ranging between -24 °C to 113 °C. Three resonances are present at varying intensities between these temperatures. The ^{1}H resonance at $\delta \approx 1$ ppm is assigned to protons attached to the carbon linking two naphthalene units together. The resonance is only present in the spectra at temperatures below 10 °C. This suggests that the NSF resin experiences significant motion when the temperature is raised. Therefore the intensity of this resonance is reduced due to motional averaging.

Two resonances appear at $\delta \approx 5$ and 6 ppm at a temperature of -24 °C marked with an asterisk ($*$) and an hash ($\#$) respectively. The resonance labelled with an asterisk is assigned as the proton resonance from the conductive proton from the sulfonate as it is the resonance which appears in a MAS PFG diffusion experiment. This is a very low chemical shift to find a resonance from a hydrogen bonded proton.

However, the ^{1}H chemical shift of the sulfonate proton in the solid state has been shown to vary greatly. Ye *et al.* [104] have investigated the proton chemical shift of poly(vinazene-propyl sulfonate) and poly(vinazene-butyl-sulfonate) wherein the sulfonate proton change from ^{1}H δ 6 ppm to 9 ppm. These differences in chemical shift are attributed to changes in the hydrogen bonding network due to changes in the conformation. This means a proton chemical shift of 5 ppm is not at all improbable for NSF. Additionally, it has previously been shown that chemical shift of hydrogen bonded protons changes significantly with temperature [33,94]. The same temperature effect is also seen in hydrogen bonding in sulfonate [104].

The resonance at 6 ppm is an amalgamation of two resonances even at -24 °C but becomes particularly clear when temperatures around 90 °C are

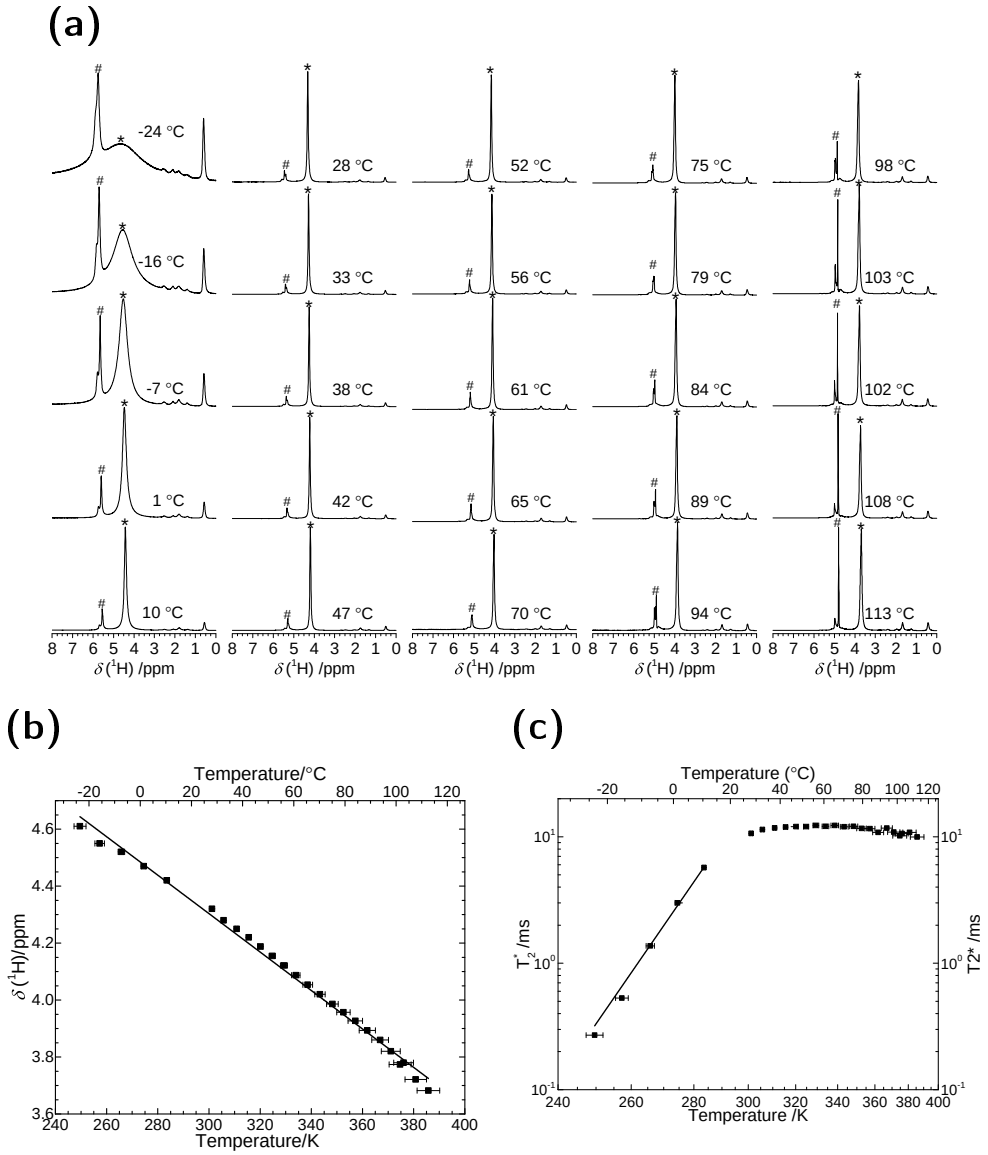

Figure 3.2: The ^{1}H spin echo MAS spectra of (a) NSF between the temperatures of −24 °C and 113 °C. The (b) chemical shift and (c) T_2^* of the resonance assigned to the sulfonate conduction proton in NSF which is labelled with an asterisk (∗) in figure (a).

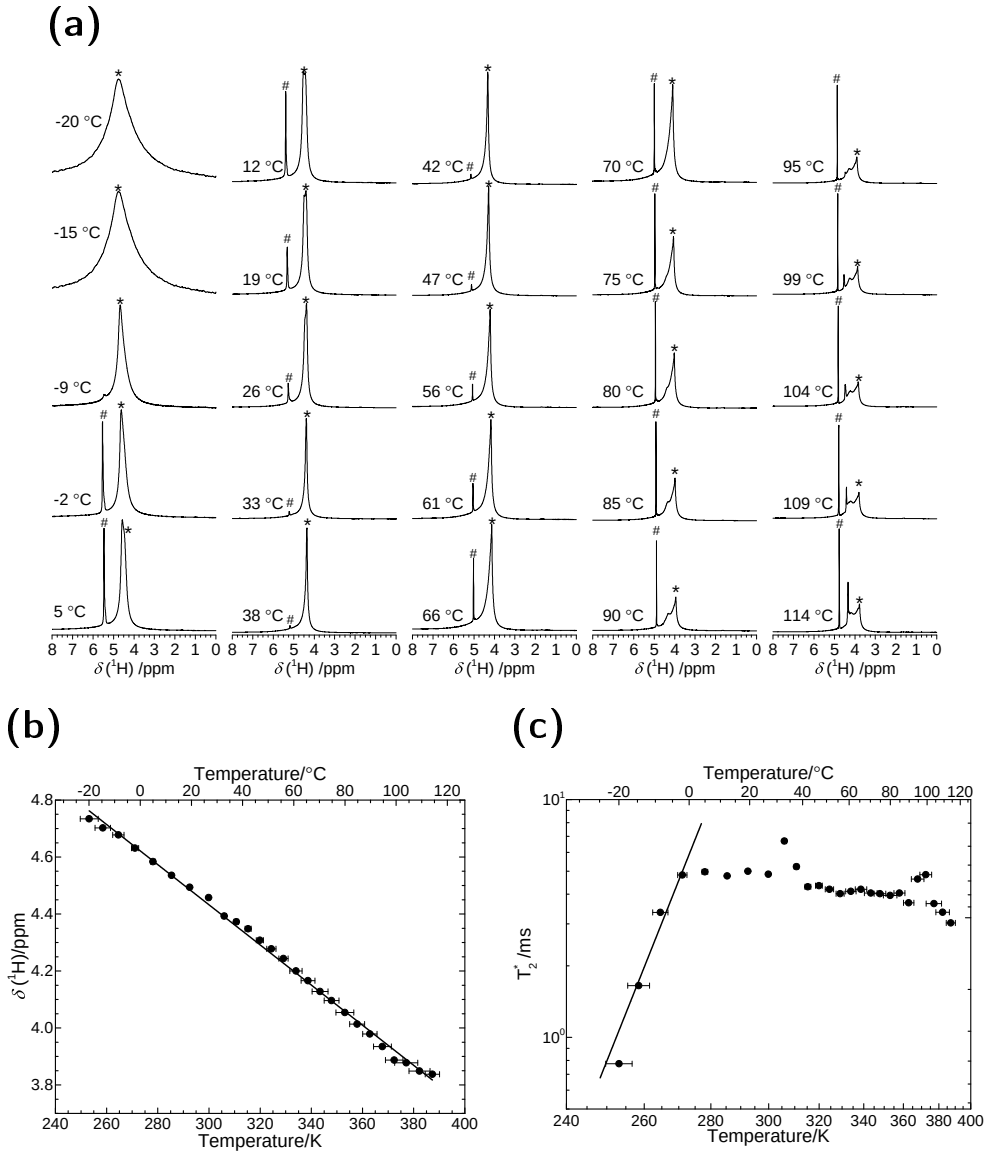

Figure 3.3: The ^{1}H spin echo MAS spectra of (a) mTiO_2(NSF)-H_2O between the temperatures of −20 °C and 124 °C. The (b) chemical shift and (c) T_2^* of the resonance assigned to the sulfonate conduction proton in NSF which is labelled with an asterisk (∗) in figure (a).

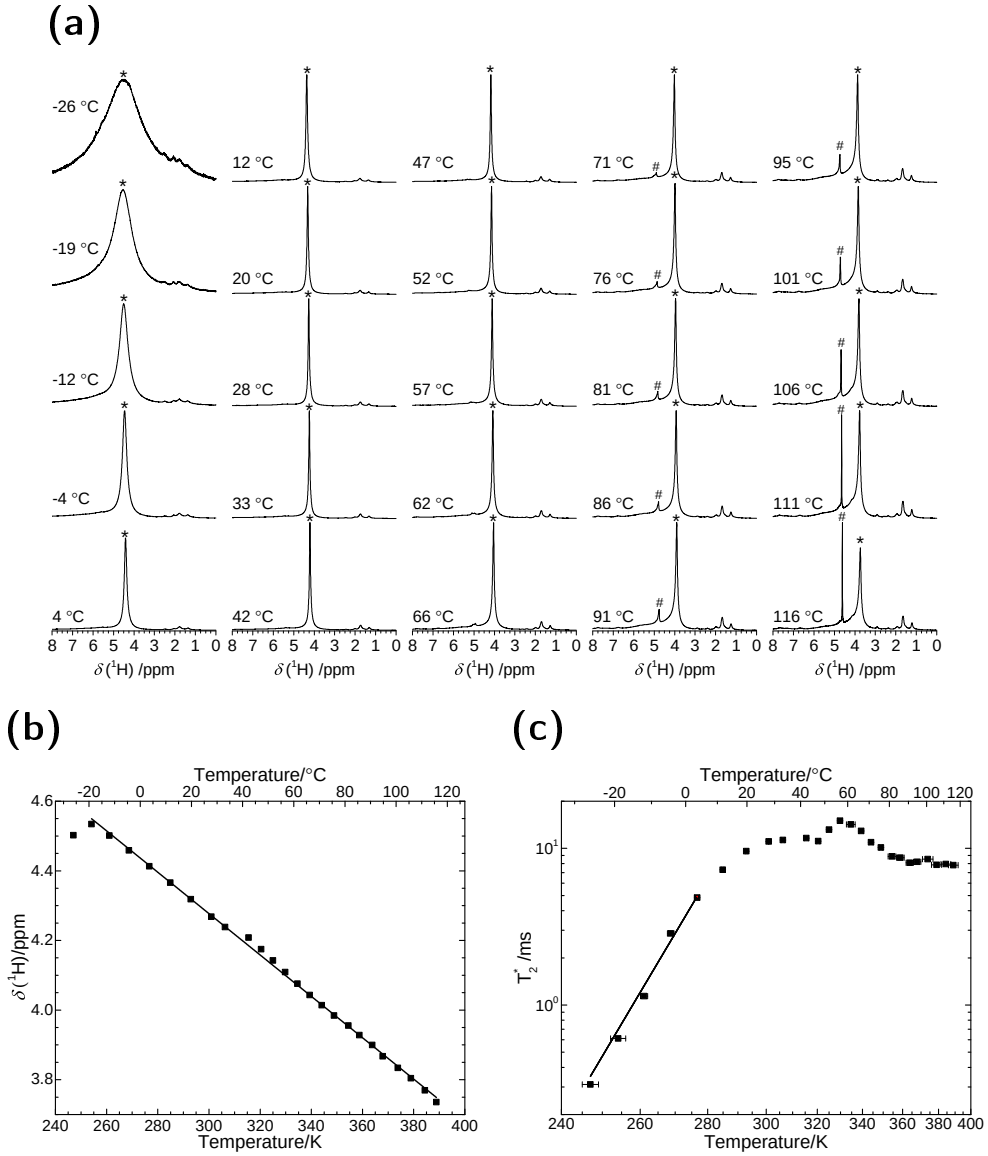

Figure 3.4: The ^{1}H spin echo MAS spectra of (a) mTiO_2(NSF)-DEE between the temperatures of −26 °C and 116 °C. The (b) chemical shift and (c) T_2^* of the resonance assigned to the sulfonate conduction proton in NSF which is labeled with an asterisk (∗) in figure (a).

reached. By elimination these resonances should belong to protons attached to the aromatic carbon ring. The chemical shift of the resonances are in the correct region traditionally assigned to such protons. However, protons are usually very rigidly attached to aromatic carbons which leads to such protons having limited motional averaging and therefore have a wide linewidth due to homogeneous broadening by homonuclear dipolar coupling between protons. The possibility that these resonances instead belong to non diffusing sulfonate protons or protons in residual water should therefore not be discounted. However, it is of little consequence for the analysis of proton diffusion as their absence in the MAS PFG experiments makes it certain protons in this environment do not participate in diffusion.

mTiO$_2$(NSF)-H$_2$O

The ^{1}H spectra of mTiO$_2$(NSF)-H$_2$O acquried between the temperatures of −20 °C and 114 °C are shown in figure 3.3a. These spectra are very similar to those of pure NSF though there are a few important differences. The resonance from the protons attached to the linker carbon in pure NSF is no longer observed at 1 ppm in mTiO$_2$(NSF)-H$_2$O. This is likely due to the dilution of NSF with mTiO$_2$ reduces an already weak resonance sufficiently that is no longer observable.

The resonance arising from the conduction protons in mTiO$_2$(NSF)-H$_2$O is labelled with an asterisk. It appears at the same chemical shift of $\delta \approx 5$ ppm as observed in pure NSF at −20 °C. However, when the temperature rises more than 80 °C the resonance in mTiO$_2$(NSF)-H$_2$O is observed to broaden and split into several distinct resonances. This is likely to be due to thermal motion of the NSF resin inside the mTiO$_2$ pores which changes the chemical environment of the hydrogen bonded sulfonate proton.

The chemical shift of the conduction resonance is tracked in figure 3.3b. When the resonance becomes broadened the most shifted resonance is tracked. The trend over this temperature range is a constant linear decline from 4.7 ppm at −20 °C to 3.8 ppm at 114 °C. This trend is virtually identical to that seen in figure 3.2b of pure NSF where a decline from 4.6 ppm at −24 °C to 3.7 ppm at

113 °C is observed. This suggests that the impregnation of NSF into the pores of $mTiO_2$ does not change the chemical environment of the hydrogen bonded sulfonate proton. This is significant because it was hoped that the sulfonate proton would interact with the pore walls.

$mTiO_2$(NSF)-DEE

The ^1H spectra of $mTiO_2$(NSF)-DEE between the temperatures of −26 °C and 116 °C are shown in figure 3.4a. The spectra are again very similar to those of both pure NSF resin and $mTiO_2$(NSF)-H_2O. The aliphatic proton observed in pure NSF under $\delta \approx 1$ ppm is again not present in the spectra of $mTiO_2$-NSF-DEE. However, one can observe two resonances between δ 1 and 2 ppm which are characteristic proton chemical shifts of diethyl ether which was used to impregnate the NSF resin into the pores in this sample.

The resonance labelled with a hash only appears above 80 °C whereas they are present at −24 °C in spectra of pure NSF resin and at −2 °C in the spectra of $mTiO_2$-NSF-H_2O. If this resonance is due to hydrogen bonded protons which no longer participate in diffusion as postulated previously their appearance at a higher temperature suggests the proton diffusion in $mTiO_2$(NSF)-DEE has greater thermal stability.

The chemical shift evolution with temperature of the conduction proton (labelled $*$) is shown in figure 3.4b. Unlike both pure NSF and $mTiO_2$(NSF)-H_2O the chemical shift does not exclusively decline as the temperature rises. When the temperature increases between the two lowest data points the chemical shift increases. At −20 °C the chemical shift is $\delta \approx 4.55$ ppm which decreases to 3.75 ppm at 116 °C. This is very similar to the trend seen with both pure NSF resin and mTiO2-NSF-DEE in figures 3.2b and 3.3b. This suggests that the proton diffusion mechanism is unlikely to involve the pore surface as this is expected to entail a significantly larger change in the chemical shift.

3.3.2 Longitudinal & Transverse Relaxation

Naphthalene Sulfonate Formaldehyde

The longitudinal T_1 proton relaxation was measured using a saturation recovery experiment between the temperatures of −30 °C and 120 °C. The resulting T_1 recovery curves were fitted using a single exponential relaxation component of the form

$$M(t) = M(0)[1 - \exp(-t/T_1)]. \tag{3.1}$$

Where $M(t)$ is the intensity of magnetisation after a recovery time t while $M(0)$ is the intensity of the magnetisation at equilibrium and T_1 is the longitudinal relaxation constant.

The longitudinal T_1 relaxation times of NSF resin between the temperatures of −25 °C and 115 °C are shown in figure 3.5. This relaxation data is fitted to three different variations of the Bloembergen, Pound & Purcell model for the relationship between temperature and T_1 relaxation [65]. The variations are a stretched BPP and double energy barrier. Each of these models are described in detail in section 2.7. The energy barrier to the movement causing the T_1 relaxation based on these models are shown in table 3.1.

The linewidth of the resonance due to the conduction proton labelled with an asterisk in figure 3.2a was simulated using a Gaussian lineshape in DMFit [105]. The linewidth is shown as function of temperature in figure 3.2c and the trend is analysed using an Arrhenius fit. The resulting energy barriers to movement calculated from linewidth data is shown in table 3.1.

The linewidth of the resonance of the conductive proton in NSF shown in figure 3.2c. From -20 °C to 20 °C the linewidth narrows by nearly two orders of magnitude. This is consistent with ambient thermal energy activating the proton diffusion which leads to averaging of the homonulcear dipolar coupling through motion and thus significantly narrows the resonance. This change in linewidth can be simulated very accurately using the Arrhenius model. Us-

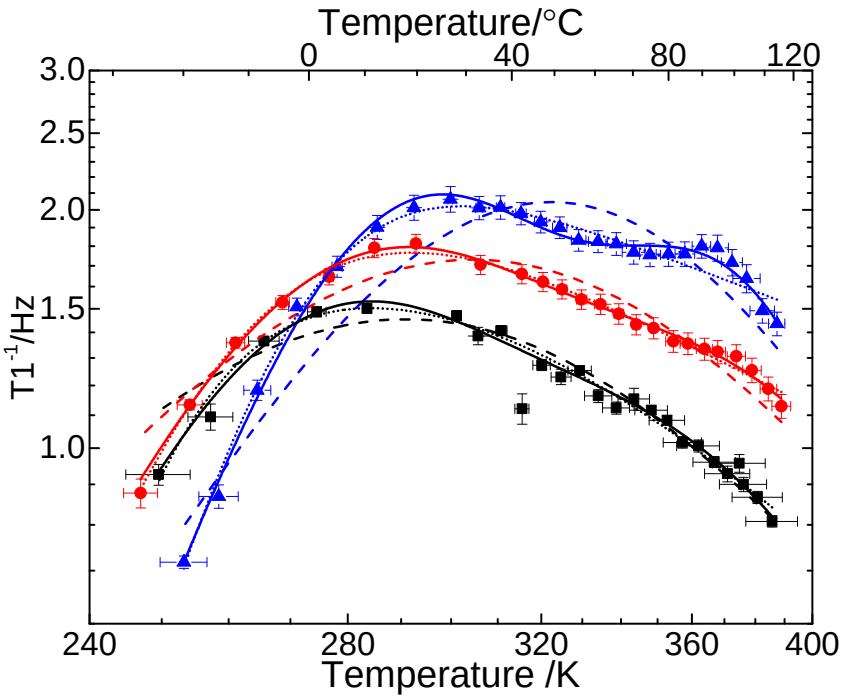

Figure 3.5: The evolution of the T_1 of NSF (black), mTiO_2-NSF-H_2O (red) and DEE (blue). The dashed line represents a standard BPP fit, the solid line a BPP fit with two energy barriers and the dotted line an empirical modification to BPP model called the stretched BPP model where the exponent is allowed to differ from two.

ing this model yields an activation energy to the motion averaging the dipolar coupling of 50 ± 2 kJ mol^{-1}. This is much higher than the barrier measured from T_1. It is also significantly higher than the activation energy measured using impedance spectroscopy [24] which is calculated to be 10 ± 2 kJ mol^{-1} using an Arrhenius model. This suggests that activation energy for the motion which leads to the averaging of the homonuclear dipolar coupling is not the same as the activation energy which must be overcome for diffusion to occur. Therefore the protons which diffuse also undergo another form of motion which is the primary cause of the averaging of homonuclear dipolar coupling. Above 20 °C the resonance does not narrow further and keeps a constant value until the maximum measured temperature of 115 °C.

In figure 3.5 is shown the longitudinal relaxation data for NSF as a function of temperature. The shape of this data is best described as an asymmetric

parabola i.e. the slopes on the low temperature and high temperature sides are different. This asymmetry is very important as the simplest model describing such T_1 data the BPP model is always symmetric. Therefore, it is immediately clear that additional elements must be added to the model to accurately simulate the T_1 data as a function of temperature. However, a simulation of the T_1 data using the BPP model is shown in figure 3.5. As expected neither the low temperature nor the high temperature behaviour is properly simulated using this model. An empirical modification called a stretched exponential is commonly used to introduce this asymmetry. Its mathematical basis is described in section 2.7.3. This model simulates the observed T_1 data much more accurately both at high and low temperature. This model yields an activation energy of 6.8 ± 0.4 kJ mol^{-1}. This is nearly an order of magnitude lower than measured from the linewidth which suggests that the activation energy of two different types of movement is measured. This is expected as the these measurements are sensitive to motion with different characteristic frequencies. This suggests that proton diffusion involves the traversal of more than one type of barrier with different activation energies associated with them.

A simulation using two independent BPP models is also presented. This yields activation energies of 22 ± 4 and 20 ± 7 kJ mol^{-1}. However, in this case two BPP models do not appear to improve the fit significantly over the stretched BPP model. Additionally, the activation energies appear to be higher than that calculated from impedance measurements. An Arrhenius analysis could not be performed on the NSF impedance data in figure 3.6 the inflection point were the impedance starts decreasing is at 50 °C which does not leave enough data to perform linear regression on.

mTiO_2(NSF)-H_2O

The T_1 relaxation data for mTiO_2(NSF)-H_2O is shown as the red data in figure 3.5. The inflexion point of the T_1 data of this sample has moved to shorter T_1 at higher temperature. Following the BPP model and all else being equal this suggests that the characteristic motion rate of the motion causing the relaxation

has become shorter. This would mean that the $mTiO_2$ has not modified and does not participate meaningfully in the proton diffusion.

The standard BPP model gives a activation energy of 13.0 ± 0.6 kJ mol^{-1}. However, like for NSF this model does not simulate the $mTiO2_2$-NSF-H_2O T_1 data accurately as it is clear that the T_1 data has different slopes on the high and low temperature side of the inflection point. A more accurate fit is achieved using a stretched BPP model which accurately reflects the asymmetrical nature of the low temperature and high temperature behaviour of the T_1 data. This model yields an activation energy of 4.8 ± 0.2 kJ mol^{-1}. Additionally, two independent BPP models were simulated. This model also fits the data well and even accounts for a small oscillation in the T_1 data at high temperature. However, it yields a significantly higher activation energies of 20 ± 1 and 21 ± 6 kJ mol^{-1}. The value for the activation energy calculated from impedance spectroscopy is 11 ± 5 kJ mol^{-1}. The activation energy from the stretched BPP model is lower than the activation energy from impedance spectroscopy. This is expected as the short time scale of the NMR experiment means that the proton experience less of the different environments present compared to impedance spectroscopy [94].

$mTiO_2$(NSF)-DEE

The T_1 relaxation for $mTiO_2$(NSF)-DEE is shown as the blue data in figure 3.5. The inflection point of this data is shifted to shorter T_1 and higher temperature when compared to both pure NSF and $mTiO_2$(NSF)-H_2O under identical conditions. This suggests that the overall mobility of the diffusing protons is increased compared to these other samples. Furthermore, there is a pronounced second local maximum at the high temperature range. This suggests that there is a second type of motion with a different characteristic rate constant which dominates the proton relaxation. This is also seen in the simulations of the data as the standard BPP model cannot fit both the low and high temperature sides while the stretched BPP model cannot simulate the second local maximum at high temperature.

Only a model using two independent BPP models can simulate this change

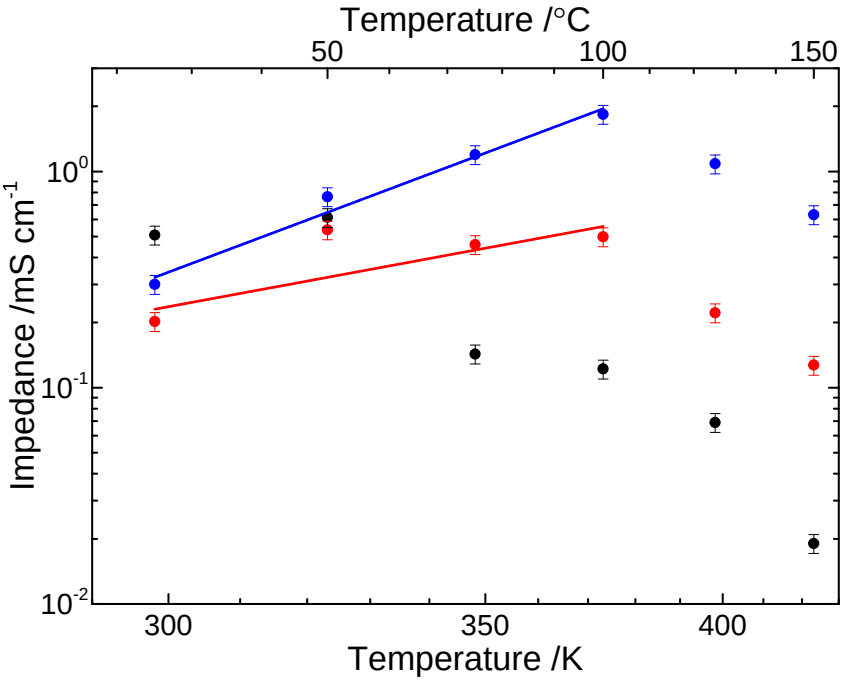

Figure 3.6: The proton conductivity of NSF (black), mTiO$_2$-NSF-H$_2$O (red) and mTiO$_2$-NSF-DEE (blue) measured using impedance spectroscopy. The data was collected by Jonanthan Turley [24]. The solid lines represent Arrhenius fits to the impedance data.

in the mobility of the protons at high temperature from 22 ± 1 to 27 ± 5 kJ mol^{-1}. This change in mobility happens at approximately 80 °C which suggests it is linked to the observed reduction in the proton diffusion rate seen above 60 °C seen in figure 3.7 as well as the reduction in proton conductivity by impedance spectroscopy above 100 °C seen in figure 3.6. These phenomena could all be explained by a phase change of the NSF around this temperature which destroys the proton conduction pathways. This change could involve an increase in the mobility of NSF which is sufficient to leave the mTiO$_2$ pores thereby breaking the proton diffusion pathway.

3.4 Proton Pulsed Field Gradient

The proton PFG-STE NMR experiments of pure NSF exhibit only a single resonance at ^{1}H $\delta \approx 4$ ppm. This suggests that only one of the resonances which are assigned to hydrogen bonded protons in the 1D spectra shown in figure 3.2a contributes to the diffusion as measured by NMR. This suggests there could be structural differences across the NSF resin which prevents certain protons from participating in diffusion. The diffusion rates measured between 20 °C and 100 °C show constant increase as the temperature rises. This is in contrast to impedance spectroscopy of NSF where the measured impedance starts to decline when the temperature rises above 50 °C. This suggests that there is a macroscopic breakup of NSF which prevents longer distance proton mobility but at the small distances probed by NMR PFG proton mobility continues to increase. The attenuation of the signal in the PFG-STE experiment is linear and can therefore be simulated with a single diffusion coefficient. The diffusion coefficients are shown in figure 3.8 which have been simulated using an Arrhenius model to estimate the thermal activation energy to proton diffusion which yielded a value of 31 ± 2 kJ mol^{-1}.

The attenuation curves due to diffusion of mTiO_2(NSF)-DEE was measured using STE-PFG NMR of proton while spinning at a MAS frequency of 20 kHz. Magic angle spinning was used as static ^{1}H STE-PFG was found to yield insufficient signal due to large losses from T_2 relaxation caused by the strong homonuclear dipolar coupling between protons. The longer T_2 and narrower resonances available from MAS were absolutely necessary to acquire sufficient signal.

The attenuation curves due to diffusion were measured between 20 and 100 °C which were the physical limits of the probe. The effect of changing the diffusion time, Δ, between 50, 100, 200 and 400 ms was examined. The experiment at 20 °C and with a diffusion time of 50 ms could not be acquired as the duration of the gradient pulse to detect the diffusion rate became too long for a viable experiment. Therefore this data point had to be abandoned. In all cases the attenuation in the PFG diffusion experiment is not a straight line and

must therefore be described by a model which incorporates more than one diffusion coefficient. The most common circumstance which can yield two diffusion coefficients occurs when the proton diffusion pathway includes two different proton transfers with different activation energies and rate constants. However, this mode predicts that as the diffusion time is increased an averaging of the two diffusion rates will occur as each proton experiences both types of transfers. This effect is not seen in this data. The model which best describes this data is the exchange and diffusion between two regions [61]. The assumptions and mathematical description of this model is found in section 2.10.4. It is shown that under these circumstances the attenuation due to diffusion can be written as follows

$$E(g) = \exp\left(-\gamma^2\delta^2 g^2 \Delta\left[D_2 + \frac{P_1 D_1}{\gamma^2\delta^2 g^2 \tau_2 P_1 D_1 + 1}\right]\right), \tag{3.2}$$

where γ is the proton gyromagnetic ratio, δ is the length of the gradient pulse, g is the maximum strength of the gradient pulse and Δ is the length of time protons diffuse. D_2 is the diffusion rate in region two, P_1D_1 is the diffusion rate in region one multiplied by the probability of finding the proton in this region and τ_2 is the average time a proton spends in region two. The latter three parameters are used to fit the model to the experimental data.

This model describes attenuation in PFG-STE experiment of a species diffusing between two types of sub-regions with different diffusion rates which are randomly distributed in a larger area. More precisely the assumption is that diffusion in the first sub-region, D_1, is substantially quicker than in the second, D_2. Under these conditions it is only possible to extract the slower of two diffusion coefficients, D_2. The faster diffusion coefficient, D_1, can only be extracted as a product with P_1, the probability of finding the proton in the fast diffusing sub-region. However, this does give a lower limit on this diffusion rate as P_1 being a probability will always be less than 1.

This model of fast and slow diffusing regions is consistent with the observation that protons diffuse primarily between NSF sulfonate moieties with the sulfates on the $mTiO_2$ pore wall providing a bridge between the NSF moieties.

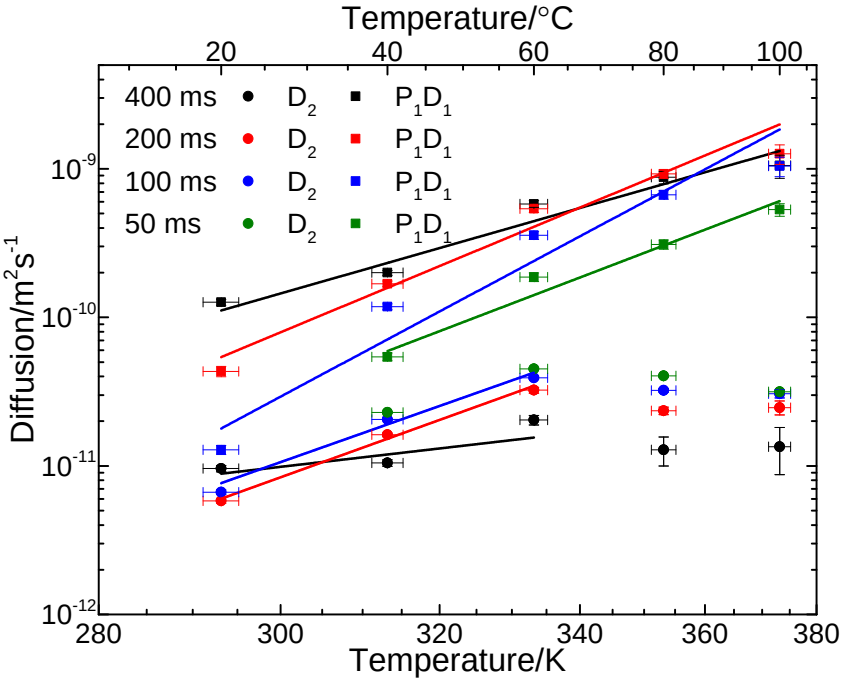

Figure 3.7: Proton MAS PFG Arrhenius plot of $mTiO_2$(NSF)-DEE with diffusion times (Δ) of 50 ms (green), 100 ms (blue), 200 ms (red) and 400 ms (black). There spectra were acquired on a Bruker Avance III operating at a ^{1}H Larmor frequency of 750.10 MHz using a narrow bore Bruker 3.2 mm HXY probe with an imaging gradient coils spinning at a frequency of 20 kHz.

In this scenario the interaction between NSF and the pore wall is weak in certain regions and thus this bridging cannot occur and proton diffusion is forced to proceed mostly directly between NSF moieties. By contrast there are regions where the NSF is arranged such that there is a strong interaction between it and the pore wall. This allows the pore wall bridging between NSF moieties to occur frequently and assuming this type of proton transfer is faster and leads to a higher proton diffusion rate. This interpretation is also consistent with the observation that the D_2 diffusion pathway is less thermally stable than P_1D_1 as would be expected if the interactions between the $mTiO_2$ pore wall and the NSF are weaker and therefore more easily disrupted thermally.

Both the fast P_1D_1 and slow D_2 diffusion rates are shown in figure 3.7 and the data has been simulated using the Arrhenius model. The diffusion rates are shown in table 3.3 and the activation energy calculated using the Arrhenius

Table 3.1: The activation energy calculated using the BPP model from spin lattice T_1 relaxation shown in figure 3.5 as well as the activation energy calculated using an Arrhenius fit of the linewidth of the resonance from conduction protons shown in figures 3.2c, 3.3c and 3.4c. The impedance spectroscopy data was collected by Jonathan Turley [24] but not the Arrhenius analysis presented here.

Sample	$mTiO_2$(NSF)-DEE /kJ mol^{-1}	$mTiO_2$(NSF)-H_2O /kJ mol^{-1}	NSF /kJ mol^{-1}
Low temperature BPP T_1	27±1	20±1	22±4
High temperature BPP T_1	32±5	21±6	20±7
Single BPP T_1	16.8±0.9	13.0±0.6	12.3±0.5
Stretched Single BPP T_1	11±7	4.8±0.2	6.8±0.4
Linewidth Arrhenius	50±4	49±8	50±2
Impedance Spectroscopy	22±2	11±5	-

model are shown in table 3.2. The activation energies have been calculated for the fast diffusion rate, P_1D_1, assuming that P_1 the probability of finding the proton in the fast diffusing region does not change with the diffusion time and temperature.

The activation energies calculated from the fast diffusion component P_1D_1 vary between 28 ± 5 to 53 ± 8 kJ mol^{-1} depending on which values for the diffusion time, Δ, was used during acquisition. Initially, when increasing the diffusion time from $\Delta = 50$ to 100 ms the activation energy increases from 38 ± 5 to 53 ± 8 kJ mol^{-1} before decreasing between 200 and 400 ms to 28 ± 5 kJ mol^{-1}.

Table 3.2: The activation energy of NSF and $mTiO_2$(NSF)-DEE calculated from PFG MAS experiments performed at temperatures between 20 and 100 °C. This data is shown in figure 3.7 and in table 3.3.

	$mTiO_2$(NSF)-DEE		NSF
Δ /ms	P_1D_1 /kJ mol^{-1}	D_2 /kJ mol^{-1}	D /kJ mol^{-1}
50	38 ± 5		
100	53 ± 8	35 ± 3	
200	41 ± 4	35 ± 2	31 ± 2
400	28 ± 5	11 ± 4	

Table 3.3: The diffusion coefficients of $mTiO_2$(NSF)-DEE measured by MAS PFG using a STE sequence. The data is shown in figure 3.7

Δ /ms	Temperature /C	$mTiO_2$(NSF)-DEE D_2 /m^2s^{-1}	$mTiO_2$(NSF)-DEE P_1D_1 /m^2s^{-1}
50	20		
	40	$2.29 \pm 0.02 \times 10^{-11}$	$5.43 \pm 0.3 \times 10^{-11}$
	60	$4.50 \pm 0.05 \times 10^{-11}$	$1.87 \pm 0.1 \times 10^{-10}$
	80	$4.03 \pm 0.06 \times 10^{-11}$	$3.10 \pm 0.2 \times 10^{-10}$
	100	$3.16 \pm 0.06 \times 10^{-11}$	$5.31 \pm 0.5 \times 10^{-10}$
100	20	$6.7 \pm 0.2 \times 10^{-12}$	$1.28 \pm 0.009 \times 10^{-11}$
	40	$2.06 \pm 0.03 \times 10^{-11}$	$1.18 \pm 0.05 \times 10^{-10}$
	60	$3.92 \pm 0.09 \times 10^{-11}$	$3.57 \pm 0.02 \times 10^{-10}$
	80	$3.23 \pm 0.09 \times 10^{-11}$	$6.69 \pm 0.4 \times 10^{-10}$
	100	$3.1 \pm 0.2 \times 10^{-11}$	$1.04 \pm 0.2 \times 10^{-9}$
200	20	$5.8 \pm 0.2 \times 10^{-12}$	$4.33 \pm 0.3 \times 10^{-11}$
	40	$1.62 \pm 0.05 \times 10^{-11}$	$1.69 \pm 0.07 \times 10^{-10}$
	60	$3.2 \pm 0.1 \times 10^{-11}$	$5.38 \pm 0.3 \times 10^{-10}$
	80	$2.35 \pm 0.1 \times 10^{-11}$	$9.25 \pm 0.6 \times 10^{-10}$
	100	$2.5 \pm 0.3 \times 10^{-11}$	$1.26 \pm 0.2 \times 10^{-9}$
400	20	$9.6 \pm 0.5 \times 10^{-12}$	$1.26 \pm 0.06 \times 10^{-10}$
	40	$1.05 \pm 0.05 \times 10^{-11}$	$2.00 \pm 0.08 \times 10^{-10}$
	60	$2.0 \pm 0.2 \times 10^{-11}$	$5.81 \pm 0.3 \times 10^{-10}$
	80	$1.3 \pm 0.3 \times 10^{-11}$	$8.77 \pm 0.9 \times 10^{-10}$
	100	$1.3 \pm 0.5 \times 10^{-11}$	$1.05 \pm 0.2 \times 10^{-9}$

This means that the activation energy of $mTiO_2$(NSF)-DEE changes between being just under the activation energy of pure NSF to nearly double as measured by PFG NMR. This large variation in the measurements for $mTiO_2$(NSF)-DEE is likely because the simulation fits P_1D_1 which is the probability of finding the particle in region 1 multiplied with the diffusion rate and not just the diffusion rate, D_1. This suggests that P_1, the probability of finding a proton in this region, is not constant as the diffusion time Δ is changed during the experiments. This is not unexpected as when the regions are sufficiently large that the diffusion time is insufficient for the proton to diffuse through multiple regions subsequently. This leaves the protons predisposed to be found preferentially in one or the other region hence leading to a P_1 which changes depending on which diffusion time was used to acquire the data. This limits the information available for the fast component of the diffusion pathway. However, this also increases confidence in the exchange and diffusion model between two regions as alternative models either predict averaging and merging of D_1 and D_2 as Δ increase or no dependence on Δ for either D_1 and D_2.

The activation energy of $mTiO_2$(NSF)-DEE calculated for D_2 using the Arrhenius model gives 35 ± 3 and 35 ± 2 kJ mol^{-1} for $\Delta = 100$ and 200 ms respectively. This is very similar to the value calculated for NSF of 31 ± 2 kJ mol^{-1} which suggests that the primary proton diffusion pathway remains unchanged through NSF. It should be noted that at $\Delta = 400$ ms the activation energy calculated is significantly lower at 11 ± 4 kJ mol^{-1}. However, this is due to the first diffusion rate measured at 20 °C which is significantly higher than the equivalent points measured for $\Delta = 100$ and 200 ms while at 20 °C. Furthermore, the diffusion rates with $\Delta = 400$ ms at 40 and 60 °C are in agreement with those measured at Δ100 and 200 ms. It is therefore reasonable to exclude the activation energy for $\Delta = 400$ ms.

The activation energies observed using PFG diffusion experiments on NSF and the D_2 component of $mTiO_2$(NSF)-DEE are 31 ± 2 and 35 ± 2 kJ mol^{-1} respectively. However, these values do not appear to be in agreement with those measured by T_1 relaxation or linewidth (T_2^*). The T_1 activation energy for these samples are lower at between 11 ± 7 and 32 ± 5 kJ mol^{-1} depending on the

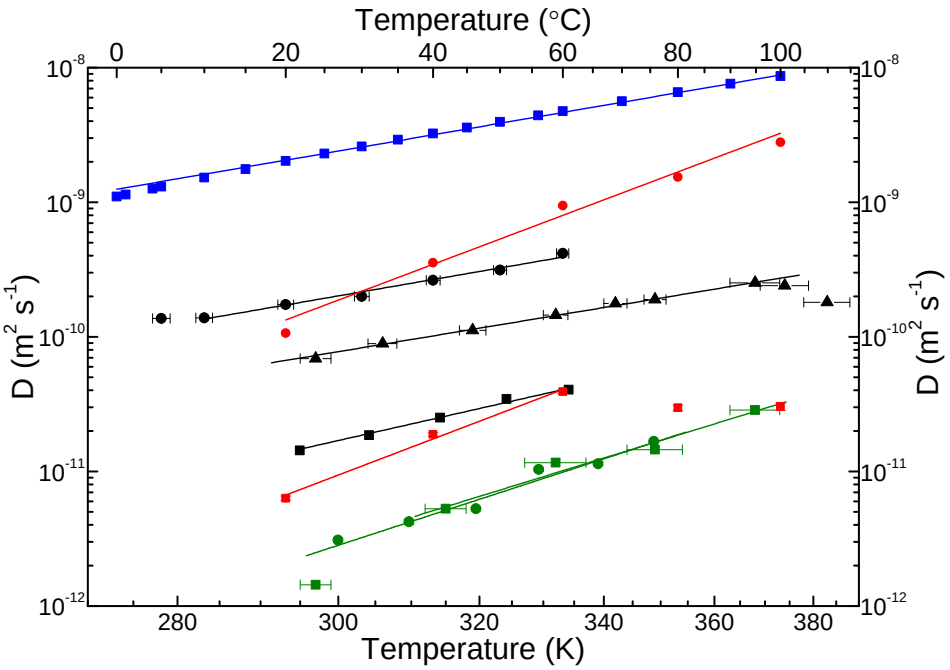

Figure 3.8: The Arrhenius plot of NSF (dark green) acquired on two systems a 500 MHz in Warwick (circles) and a 400 MHz in Orleans (squares), mTiO_2(NSF) with $\Delta = 400$ ms (red), water (blue) and Nafion (black) acquired in Warwick (circles), in Orleans (squares) and from literature (triangles) [53].

model used while T_2^* activation energy measurements are higher at 50 kJ mol^{-1}. However, both T_1 and T_2^* relaxation are very sensitive to the correlation time of motion but each is sensitive to a different range of correlation times. Given the amorphous nature of NSF there is likely a distribution of energy barriers in the proton diffusion pathway which in turn leads to a distribution of associated correlation frequencies. This would lead to T_1 and T_2^* measurements of different activation depending on their associated correlation time. By contrast measurements by PFG diffusion does not depend on the correlation time and therefore is an average of the activation energies.

The above observation further implies a reason for the discrepancy between the activation energy of the PFG diffusion of 35 ± 2 kJ mol^{-1} compared to impedance spectroscopy proton conductivity of 22 ± 2 kJ mol^{-1}. This suggests that there are proton diffusion pathways which are characterised by higher activation energy which do not contribute to overall proton conductivity. The values

for the impedance spectroscopy most closely resemble those of the T_1 relaxation which suggest that this measurement could be a probe in NSF for the activation energy of the proton conductivity.

3.5 Conclusion and Further Work

The chemical shift of diffusing protons in both pure NSF and $mTiO_2$(NSF) was found to be ^{1}H $\delta \approx 4$ ppm at 20 °C using 1D NMR and PFG NMR spectroscopy. This suggests the hydrogen bonding network in NSF is similar in these samples after adsorption by $mTiO_2$(NSF). Furthermore, it suggests that the whole hydrogen bonding network is connected and exchanging. The activation energy of this resonance was calculated using T_1, linewidth and PFG NMR data from experiments at variable temperature. A two region diffusion and exchange model was used to simulate PFG attenuation data from $mTiO_2$(NSF)-DEE with two diffusion coefficients both of which are higher than pure NSF. This contrasts with only needing a single diffusion coefficient which suggests that the $mTiO_2$ pore walls interacts with the NSF diffusion mechanism differently in regions.

The activation energies calculated from T_1, diffusion and impedance experiments are not in agreement with each other. It is suggested that this arises due to a difference in their dependence on the correlation time. This suggests that NSF possess a distribution of correlation times and by extension activation energies for proton motion due to the amorphous nature of the material. The difference between the activation energy of diffusion in PFG and conductivity in impedance spectroscopy suggests that longer range transport of proton measured using impedance spectroscopy is different to that over shorter periods measured by PFG diffusion.

Further investigation would involve lengthening the diffusion time Δ used for MAS STE-PFG experiments on $mTiO_2$(NSF)-DEE with the goal of finding a value beyond which is observed the averaging of the two coefficients into a single one. However, this will prove difficult due to T_1 signal loss during the STE-PFG experiment. Performing the same experiments on $mTiO_2$(NSF)-H_2O

as has been performed on mTiO_2(NSF)-DEE would further solidify trust in the validity of the two region diffusion and exchange model.

Chapter 4

Mesoporous Tantalum and Niobium Oxide with Naphthalene Sulfonate Formaldehyde

4.1 Introduction

It has been shown that mesoporous niobium oxide (mNb_2O_5) tantalum oxide and mesoporous (mTa_2O_5) impregnated with NSF have better proton conductivity than Nafion at 80 °C. However, when the temperature rises above 125 °C the conductivity drops significantly [25]. However, it is unclear how proton diffusion happens at an atomic level and why proton conductivity stops above 125 °C. Of particular interest is how the mesopores affect the proton diffusion in NSF. Does the pore surface participate in the diffusion or does it merely change the arrangement of NSF to increase diffusion and how does this affect the hydrogen bonding experienced by the diffusing protons.

Solid state NMR is uniquely suited to probe the hydrogen bonding which leads to proton diffusion at the atomic level [93, 94]. Hydrogen bonding protons can be distinguished from other protons by their chemical shift using solid state NMR. The motion of such protons affect the chemical shift and relaxation. The manner which the chemical shift and relaxation change with increases in

temperature depends on the proton motion. Additionally, the rate of diffusion at the molecular level can be measured using pulsed field gradients (PFG) which when measured across a range of temperatures can be used to calculate the energy barrier to diffusion at a molecular level.

Therefore mTa_2O_5(NSF) and mNb_2O_5(NSF) samples were investigated using ^{1}H spin echoes to identify the chemical shifts of protons moving through the hydrogen bonded network and how it changes with temperature. The dynamical nature of these protons was investigated using longitudinal relaxation T_1 [36, 95] as well as PFG MAS [52, 53, 58]. These are each affected differently by proton motion and can be used to elucidate different aspects of proton motion which leads to diffusion. Additionally, the oxygen environment of the sulfonate and metal oxide pore walls which form the hydrogen bond network together with the protons were investigated using ^{17}O spin echo spectra.

4.2 Experimental Details

4.2.1 Materials

Mesoporous niobium oxide, mNb_2O_5, and tantalum oxide, mTa_2O_5 doped with sulfate and impregnated with NSF resin were obtained from Jonathan P. Turley at the University of South Wales. The mesoporous metal oxides, mM_2O_5, were synthesised by Jonathan P. Turley using amines with varying length of linear carbon chains as templates [97]. The lengths of the carbon alkane chains of these templates are 6, 12 and 18 for samples labeled C6, C12 and C18 respectively. This resulted in pore sizes between 20 and 35 Å [25] as measured by Barett-Joyner-Halenda (BJH) analysis [98] and can be seen in table 4.1. The surface of the metal oxides were then functionalised with sulphate [25].

The NSF resin impregnated into the metal oxides has a molecular weight between 400 and 1000 g mol^{-1} corresponding to a resin chain length between 2 to 6 units [25, 99, 100]. The short chain length of the NSF resin allows for facile impregnation of the metal oxide pores. The pores of the metal oxides

were impregnated with NSF resin while in diethyl ether [25].

All samples mTa_2O_5(NSF) and mNb_2O_5(NSF) were centre packed with a layer approximately 2 mm thick in 3.2 mm rotors. A layer of Teflon tape was put on either side of the metal oxides which isolated the samples from a layer of lead nitrate, $Pb(NO_3)_2$, at the top and bottom of the rotor. This was used used to determine the temperature of the samples in situ as the change in chemical shift of ^{207}Pb is proportional to the change in temperature [101–103]. Furthermore, this enabled the measurement of the temperature on both sides of the sample by measuring the chemical shift of the two resonances in the ^{207}Pb spectrum by taking their average. The temperature gradient across the sample [101] was estimated by calculating the difference between the chemical shift of the ^{207}Pb resonances.

All samples labelled by ^{17}O were packed under a nitrogen atmosphere to avoid exchange between the oxygen in the air and that in the metal oxide of the sample as this would dilute the labelling of the sample.

4.2.2 Solid State NMR

Samples of C6-, C12- and C18-mTa_2O_5(NSF) and mNb_2O_5(NSF) were studied using ^{1}H saturation recovery MAS NMR and spin echo MAS NMR spectra which were acquired on a Bruker Avance III spectrometer operating at 11.75 T corresponding to a ^{1}H Larmor frequency of $\omega_0 = 500.10$ Hz. A Bruker 3.2 mm triple channel probe operating in dual channel mode was used and a MAS frequency of 10 kHz was achieved. The sequence used to measure ^{1}H T_1 relaxation was a saturation recovery with spin echo acquisition $[\tau_S - \pi]_n - t_1 - \pi/2 - \tau_R - \pi - \tau_R -$acquire. The length of the $\pi/2$ pulse is 2.5 μs while the π pulse is 5 μs and is used both in the saturation pulse train and the echo acquisition. The length of delay in the saturation pulse train is $\tau_S = 20$ μs while the saturation train was repeated 151 times. The length of the echo delay is $1/\nu_R = \tau_R = 100$ μs. The length of the T_1 recovery delay was varied in 32 steps between 1 μs and 10 s and at each delay 16 experiments were co-added. The recovery time of the spin echo MAS experiments were 10 s. Both saturation recovery and spin echo

spectra were acquired every 10 °C between the temperatures of -30 °C and 120 °C. All the ^{1}H chemical shifts are referenced to the ^{1}H solid reference of alanine at δ 1.3, 3.5 and 8.3 ppm which is a secondary reference to TMS at δ 0.0 ppm.

The samples of C12- and C18-mNb_2O_5(NSF) were studied using ^{1}H stimulated echo pulsed field gradient under magic angle spinning (STE-PFG MAS) spectra which were acquired on a wide bore Bruker Avance III spectrometer operating at 17.62 T corresponding to a proton Larmor frequency of $\omega_0 = 750.0$ MHz. A narrow bore Bruker 3.2 mm dual channel probe was used and a MAS frequency of 20 kHz was achieved. The sequence used for the STE-PFG MAS with z-filtered acquisition $\pi/2-\delta-\pi/2-\Delta-\pi/2-\delta-\pi/2-\pi/2-\tau_z-\pi/2-$acquire. The length of all $\pi/2$ pulses was 2.5 μs. The diffusion time Δ of 50 ms was used and the length of the applied δ (field gradient pulse) was varied to keep overall attenuation constant across all diffusion times while keeping the maximum field gradient pulse at 600 G cm^{-1}. A recycle delay of 3 s was used. All the ^{1}H chemical shifts are referenced to the primary reference TMS at δ 0.0 ppm.

Samples of C6, C12 and C18-mNb_2O_5(NSF) as well as C12-mTa_2O_5(NSF) doped with NSF were studied using ^{17}O 1D spin echo MAS and 2D MQMAS NMR measurements.

The 1D spin echo measurements were acquired on a 7.05 T Infinity+ spectrometer operating at a ^{17}O Larmor frequency of $\omega_0 = 40.69$ MHz, a 11.75 T Bruker Avance III spectrometer operating at a ^{17}O Larmor frequency of $\omega_0 = 67.78$ MHz and a 14.05 T Bruker Avance II+ spectrometer operating at a ^{17}O Larmor frequncy of $\omega_0 = 81.37$ MHz. At all fields these experiments were implemented using a Bruker 3.2 mm HXY probe operating in double channel mode which enabled a MAS frequency of 20 kHz in all cases. Each solid echo measurement was undertaken using a $\theta-\tau-\theta-\tau-$acquire experiment (with $\theta = \pi/4$) with $\pi/4$ pulse lengths of length 1 μs duration, and a short recycle delay of 100 ms. This short recycle delay was compared against similar experiments with much longer recycle delays of up to 5 s to ascertain the true quantitative nature of the data.

The 2D MQMAS measurements were acquired on a 11.75 T Bruker Avance

III spectrometer operating at $\omega_0 = 67.78$ MHz used the four pulse z-filtered $3\pi/2 - t1 - \pi/2 - (\pi/2 - \tau - \pi/2) -$ acquire experiment where the final two $\pi/2$ pulses constitute the soft z-filter. This experiment utilised hard $3\pi/2$ triple quantum excitation pulses and $\pi/2$ conversion pulses of 3.6 and 1.2 μs length, respectively, in addition to the selective (soft) z-filter $\pi/2$ pulses of 12 μs duration with a 20 μs delay between them and a recycle delay 100 ms. All ^{17}O chemical shifts were referenced to the ^{17}O primary reference H_2O at δ 0.0 ppm.

4.3 Proton Chemical Shift & Longitudinal Relaxation

4.3.1 Chemical Shift

In figures 4.1a, 4.2a, 4.3a, 4.4a, 4.5a and 4.6a can be seen the ^1H spin echo NMR MAS spectra of C6-, C12- and C18-mTa_2O_5(NSF) and mNb_2O_5(NSF) acquired at temperatures between -30 °C and 120 °C. Over this temperature range the linewidth of the resonances change significantly. All the spectra all contain the same type of resonances though the details are different for each samples. At ^1H $\delta \approx 1$ ppm there are two resonances which are consistent with the methylene linking between naphthalene units. This resonance only appears at about 10 °C for C6- and C12-Ta_2O_5(NSF) and C6-Nb_2O_5(NSF). For the rest it is present in all the spectra acquired regardless of temperature.

When the temperature exceeds 50 °C several narrow resonances between ^1H $\delta \approx 6$ to 8 ppm appear in the spin echo. These resonances are consistent with aromatic protons on the naphthalene rings. Usually these resonances are not expected to be observed individually as being this narrow due to the very strong homonulcear dipolar coupling between them. However, the dipolar coupling appears to be greatly reduced when the temperature rises above 50 °C. The only phenomenon which can cause this molecular mobility which averages the dipolar coupling to virtually nothing resulting in a narrow resonance.

The ^1H chemical shift of the sulfonate proton in the solid state has been shown to vary greatly. Ye et al. [104] have investigated the proton chemical shift

of poly(vinazene-propyl sulfonate) and poly(vinazene-butyl-sulfonate) wherein the sulfonate proton change from ^{1}H δ 6 ppm to 9 ppm. These differences in chemical shift are attributed to changes in the hydrogen bonding network due to changes in the conformation. Furthermore, the chemical shift of hydrogen bonded protons are very sensitive to changes in temperature [93]. The chemical shift of such protons will change significantly as the temperature is raised while the chemical shift of protons which are covalently bonded will be constant. The resonances in each spin echo spectra labelled with and an asterisk ($*$) or a hash (#) are therefore the hydrogen bonded proton which are the cause of the proton conductivity.

The ^{1}H chemical shift evolution of the resonance assigned to hydrogen bonded protons can be seen in figures 4.1b, 4.2b, 4.3b, 4.4b, 4.5b and 4.6b. In all cases the chemical shift of this resonance initially declines rapidly until between 20 °and 40 °C. The resonance due to conduction protons splits from a single resonance into two resonances when the temperature rises above 20 °C to 40 °C. One of these resonances which in this work has always been labelled hash (#) appears at/or rises to 9 ppm. Thereafter it quickly diminishes in intensity and disappears completely when the temperature reaches between 60 °C and 70 °C. The other resonance which is labelled with an asterisk shows more varied behaviour in the ^{1}H chemical shift. Both C6-Ta_2O_5(NSF) and C6-Nb_2O_5(NSF) show an increase in chemical shift subsequent to splitting whereas the rest of the samples have a ^{1}H chemical shift which continues to decline.

These resonances represent protons which are hydrogen bonded differently. The resonance labelled with an $*$ is assigned to the proton associated with the sulfonate group as it appears to have a near one to one correspondence with the aromatic protons which appear above 50 °C. The resonance labelled with a hash which is assigned to protons on the pore walls of the metal oxides. This suggests that around this temperature the protons on the pore surface and the NSF are isolated. If there were fast proton exchange between these sites only a single resonance would be detected like when the sample is below 20 °C. The appearance of two resonances suggests that the exchange between these sites is inhibited. The resonance labelled with a hash disappearing when the tem-

Table 4.1: The average pore sizes of mNb_2O_5(NSF) and mTa_2O_5(NSF) measured using BJH analysis [98] by Jonathan P. Turley [25]

Template	mNb_2O_5(NSF) \Å	mTa_2O_5(NSF) \Å
C6	-	34.6
C12	32.7	28.2
C18	24.8	39.3

perature is above 60 °C. As these resonances are assigned to sulfonate groups which are anchored with covalent bonds it is unlikely these protons have physically evaporated. This suggests that the protons are simply immobile but dipolar broadening prevents their detection.

This phenomenon is likely to be connected to the appearance of aromatic resonances around 50 °C. The protons associated to these resonances would traditionally have a large dipolar coupling between them. These narrow aromatic resonances are therefore likely caused by motion of the molecular NSF. This motion is likely to disrupt any association between the sulfonate on NSF and the pore wall. This suggests the reason for the appearance of resonances for two hydrogen bonded protons. When the NSF begins to gain molecular mobility due to thermal activation the proton exchange between these environments are disrupted and two resonances emerge. This split happens at the highest temperature at just above 40 °C for C12-mTa_2O_5(NSF) and C18-mNb_2O_5(NSF) which suggest that these samples should be most resistant to thermal destruction and this is consistent with proton impedance measurements [25]. These samples are found to have very similar pore size of around 30 Å suggesting this is the size which best encloses the NSF.

In the spin echo NMR MAS spectra samples of C6- and C12-mTa_2O_5(NSF) and mNb_2O_5(NSF) seen in figures 4.4a, 4.5a, 4.1a and 4.2a an additional resonance appears at $\delta \approx 4$ ppm when the temperature rises above 100 °C. The chemical shift and very narrow nature of this resonance suggests that this is residual water evaporating from the sample. In the spectra of C12-mNb_2O_5(NSF) where this water resonance is observed to merge with the resonance from hydrogen

bonded sulfonate protons when the temperature rises above 115 °. This suggests that if physio absorbed water were participating in proton diffusion at lower temperature the observed chemical shift of such a resonance would arise at a lower chemical shift. This is consistent with mTa_2O_5(NSF) and mNb_2O_5(NSF) proton diffusion not being reliant on hydration.

4.3.2 Longitudinal Relaxation

Longitudinal T_1 relaxation was measured using a saturation recovery for C6-, C12- and C18-mTa_2O_5(NSF) and mNb_2O_5(NSF) at temperatures between -30 and 120 °C. In all cases the T_1 recovery was found to fit to two relaxation components of the form

$$M(t) = A_{\mathrm{a}}[1-\exp(-t/T_{1,\mathrm{a}})] + A_{\mathrm{b}}[1-\exp(-t/T_{1,\mathrm{b}})].$$

These values for T_1 were then plotted as a function of temperature and can be seen in figures 4.1c, 4.2c, 4.3c, 4.4c, 4.5c and 4.6c for C6-, C12- and C18-mTa_2O_5(NSF) and mNb_2O_5(NSF) respectively. Both components for each sample follow very similar patterns and the data from the fast relaxation rate will therefore be discussed although the second component is also shown. The data was then fitted to a BPP model for T_1 relaxation and the calculated values for the energy barriers to the motion causing T_1 relaxation can be seen in table 4.2.

It can be seen in figures 4.1c, 4.4c and 4.6c that there are two maxima in the T_1. The BPP model gives rise to a single maximum when it is used in its standard form (seen in section 2.7.2) which assumes the relaxation is caused by a single motion with a characteristic energy barrier. Therefore, fitting this data requires two BPP models with separate parameters in order to fit the data. This means that there are two regimes of motion affecting the T_1 relaxation of the diffusing protons which have been assumed to be independent so that the separate contributions to the T_1 relaxation can be made by a linear superposition as shown in section 2.7.2. One component is the dominant effect on relaxation

Table 4.2: The energy barrier calculated using a BPP T_1 model [65] assuming two different types of proton motion causing T_1 relaxation. The parameters for simulating either motion were allowed to vary independently. The T_1 of mNb_2O_5(NSF) and mTa_2O_5(NSF) samples were measured by saturation recovery.

Sample	Low temperature BPP T_1 \kJ mol^{-1}	High temperature BPP T_1 \kJ mol^{-1}	Impedance \kJ mol^{-1}	Diffusion P_1D_1 \kJ mol^{-1}	Diffusion D_2 \kJ mol^{-1}
C6-mTa_2O_5(NSF)	17.3 ± 0.7	26 ± 2	14 ± 8		
C12-mTa_2O_5(NSF)	17 ± 1	-	19 ± 3		
C18-mTa_2O_5(NSF)	-	-	13 ± 8		
C6-mNb_2O_5(NSF)	22 ± 2	66 ± 12			
C12-mNb_2O_5(NSF)	18 ± 1	-	44 ± 7		
C18-mNb_2O_5(NSF)	33 ± 4	54 ± 28			

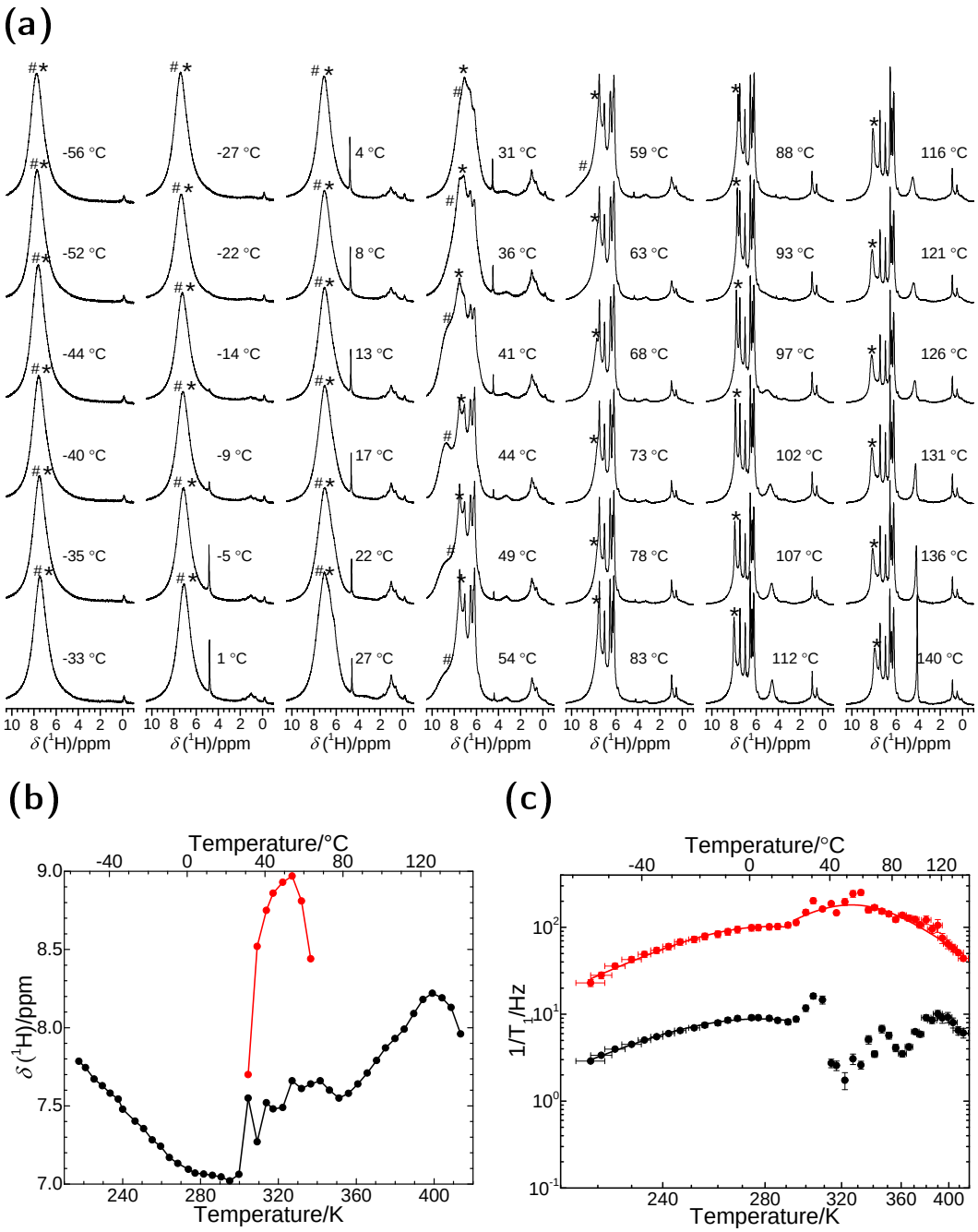

Figure 4.1: The ^{1}H spin echo MAS data of C6-mTa_2O_5(NSF) between -56 °C and 140 °C is shown in (a), where the resonance assigned to the conduction ^{1}H species associated with the NSF SO_3H moieties and conduction H species from the Ta_2O_5 pore wall are labelled with with an asterisk (∗) and a hash (#). The change in ^{1}H chemical shift with temperature of the asterisk and hash marked resonances are shown in (b) in black and red, respectively. The change in T_1 with temperature of the asterisk labelled resonance is shown in (c) with the two T_1 components of this resonance shown in black and red. The T_1 data has been fitted to the BPP model.

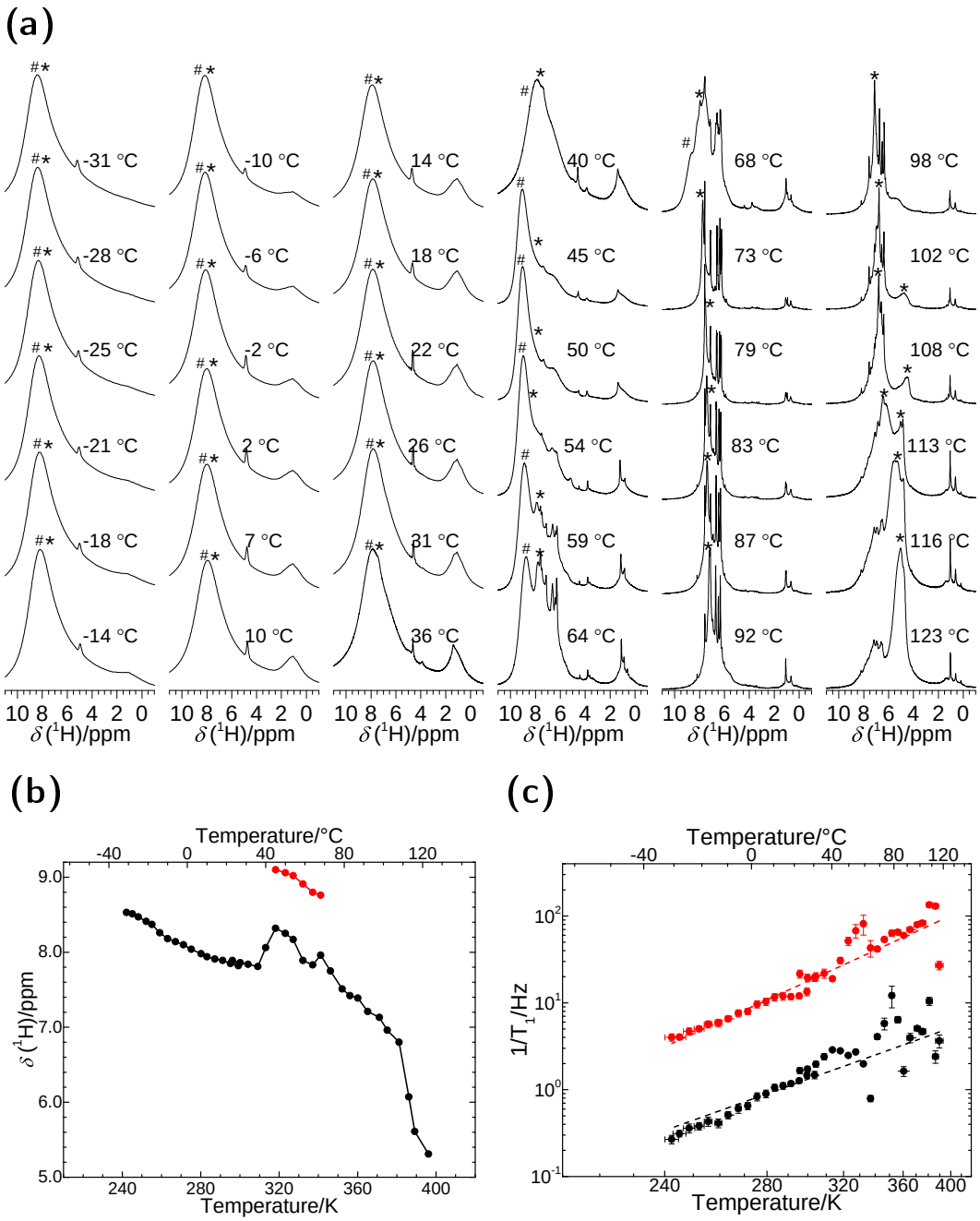

Figure 4.2: The ^{1}H spin echo MAS data of C12-mTa_2O_5(NSF) between -31 °C and 124 °C is shown in (a), where the resonance assigned to the conduction ^{1}H species associated with the NSF SO_3H moieties and conduction H species from the Ta_2O_5 pore wall are labelled with with an asterisk (∗) and a hash (#). The change in ^{1}H chemical shift with temperature of the asterisk and hash marked resonances are shown in (b) in black and red, respectively. The change in T_1 with temperature of the asterisk labelled resonance is shown in (c) with the two T_1 components of this resonance shown in black and red. The T_1 data has been fitted to the BPP model.

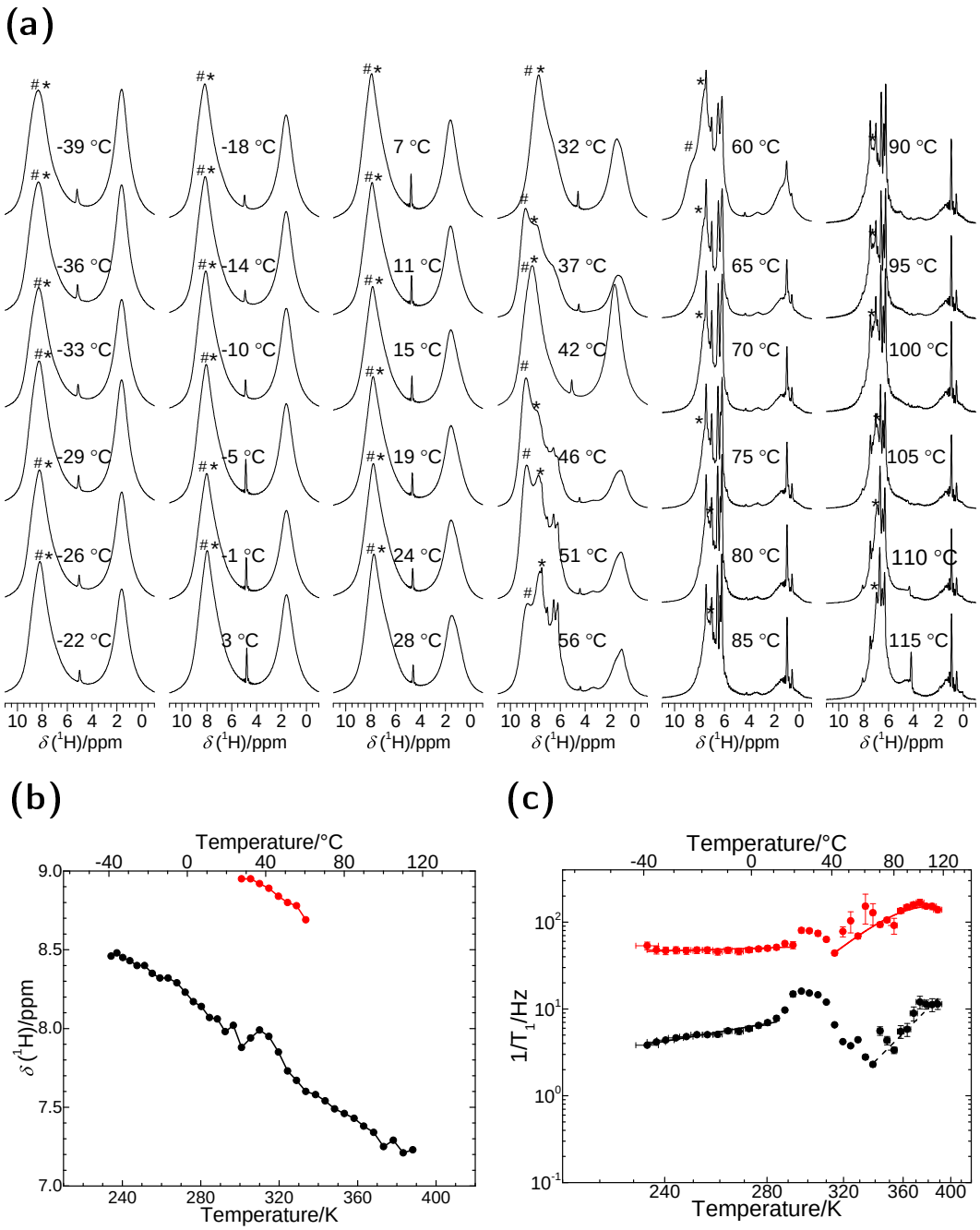

Figure 4.3: The ^{1}H spin echo MAS data of C18-mTa_2O_5(NSF) between -39 °C and 115 °C is shown in (a), where the resonance assigned to the conduction ^{1}H species associated with the NSF SO_3H moieties and conduction H species from the Ta_2O_5 pore wall are labelled with with an asterisk (∗) and a hash (#). The change in ^{1}H chemical shift with temperature of the asterisk and hash marked resonances are shown in (b) in black and red, respectively. The change in T_1 with temperature of the asterisk labelled resonance is shown in (c) with the two T_1 components of this resonance shown in black and red. The T_1 data has been fitted to the BPP model.

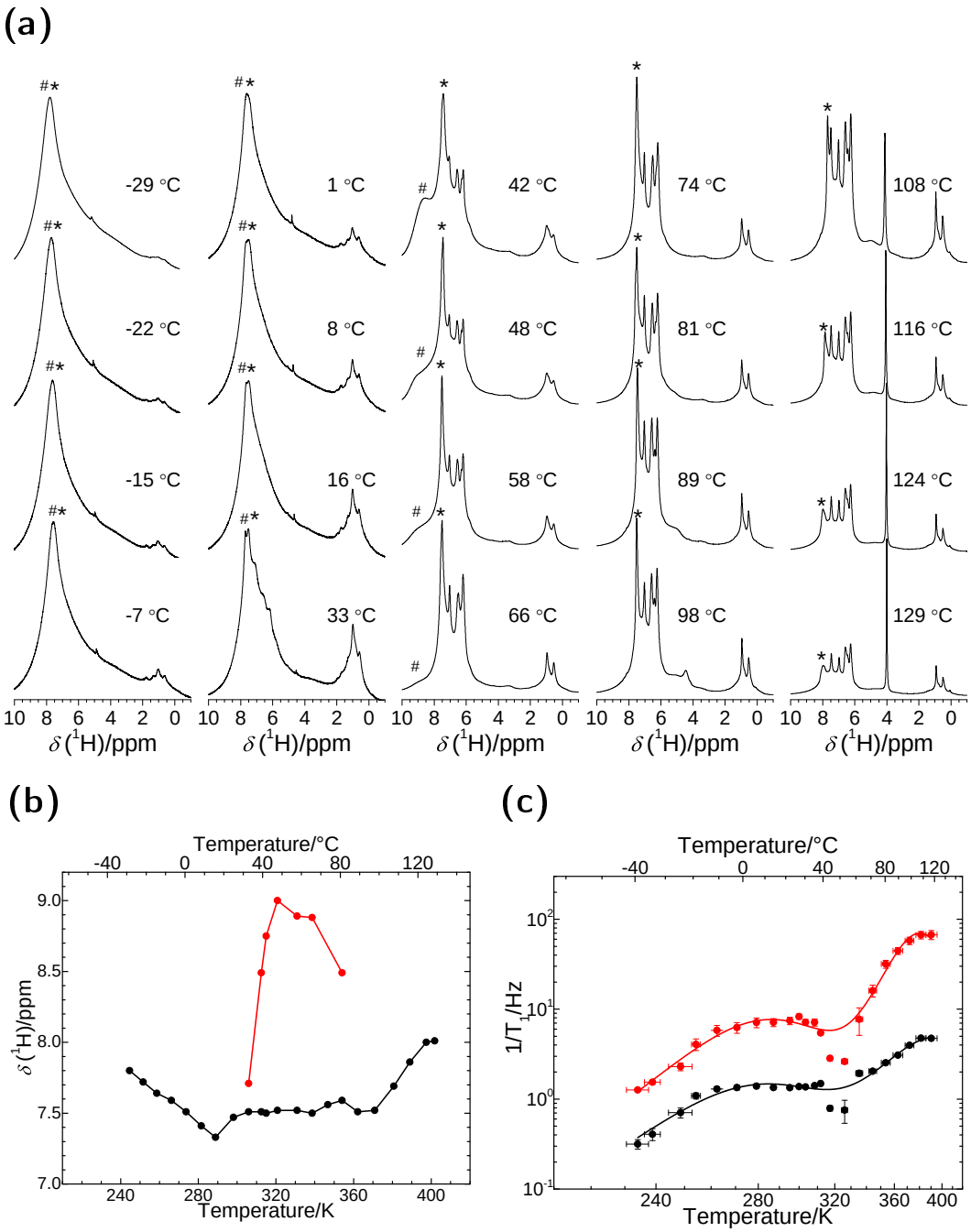

Figure 4.4: The ^{1}H spin echo MAS data of C6-mNb_2O_5(NSF) between -29 °C and 129 °C is shown in (a), where the resonance assigned to the conduction ^{1}H species associated with the NSF SO_3H moieties and conduction H species from the Nb_2O_5 pore wall are labelled with with an asterisk (∗) and a hash (#). The change in ^{1}H chemical shift with temperature of the asterisk and hash marked resonances are shown in (b) in black and red, respectively. The change in T_1 with temperature of the asterisk labelled resonance is shown in (c) with the two T_1 components of this resonance shown in black and red. The T_1 data has been fitted to the BPP model.

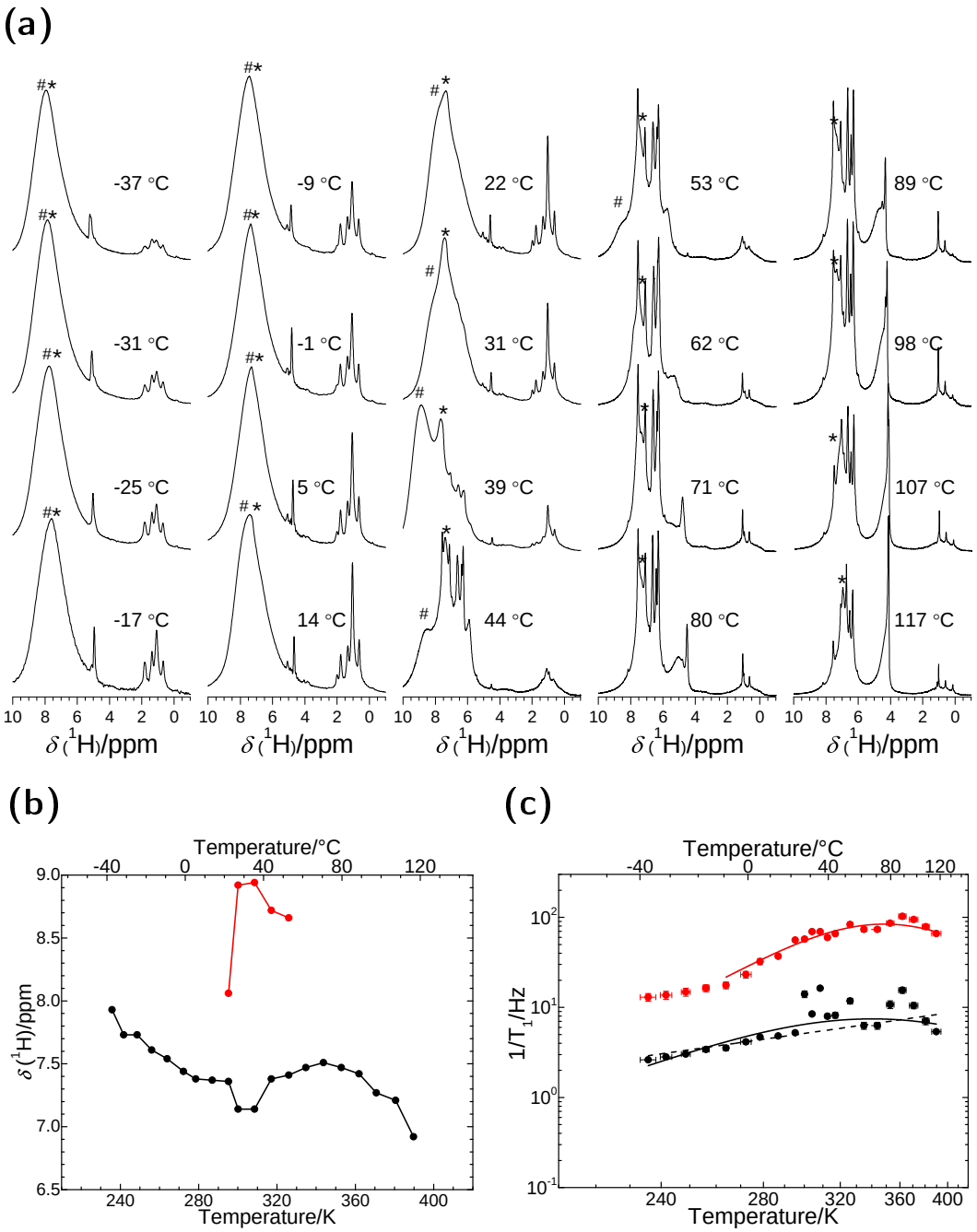

Figure 4.5: The ^{1}H spin echo MAS data of C12-mNb_2O_5(NSF) between -29 °C and 129 °C is shown in (a), where the resonance assigned to the conduction ^{1}H species associated with the NSF SO_3H moieties and conduction H species from the Nb_2O_5 pore wall are labelled with with an asterisk (∗) and a hash (#). The change in ^{1}H chemical shift with temperature of the asterisk and hash marked resonances are shown in (b) in black and red, respectively. The change in T_1 with temperature of the asterisk labelled resonance is shown in (c) with the two T_1 components of this resonance shown in black and red. The T_1 data has been fitted to the BPP model.

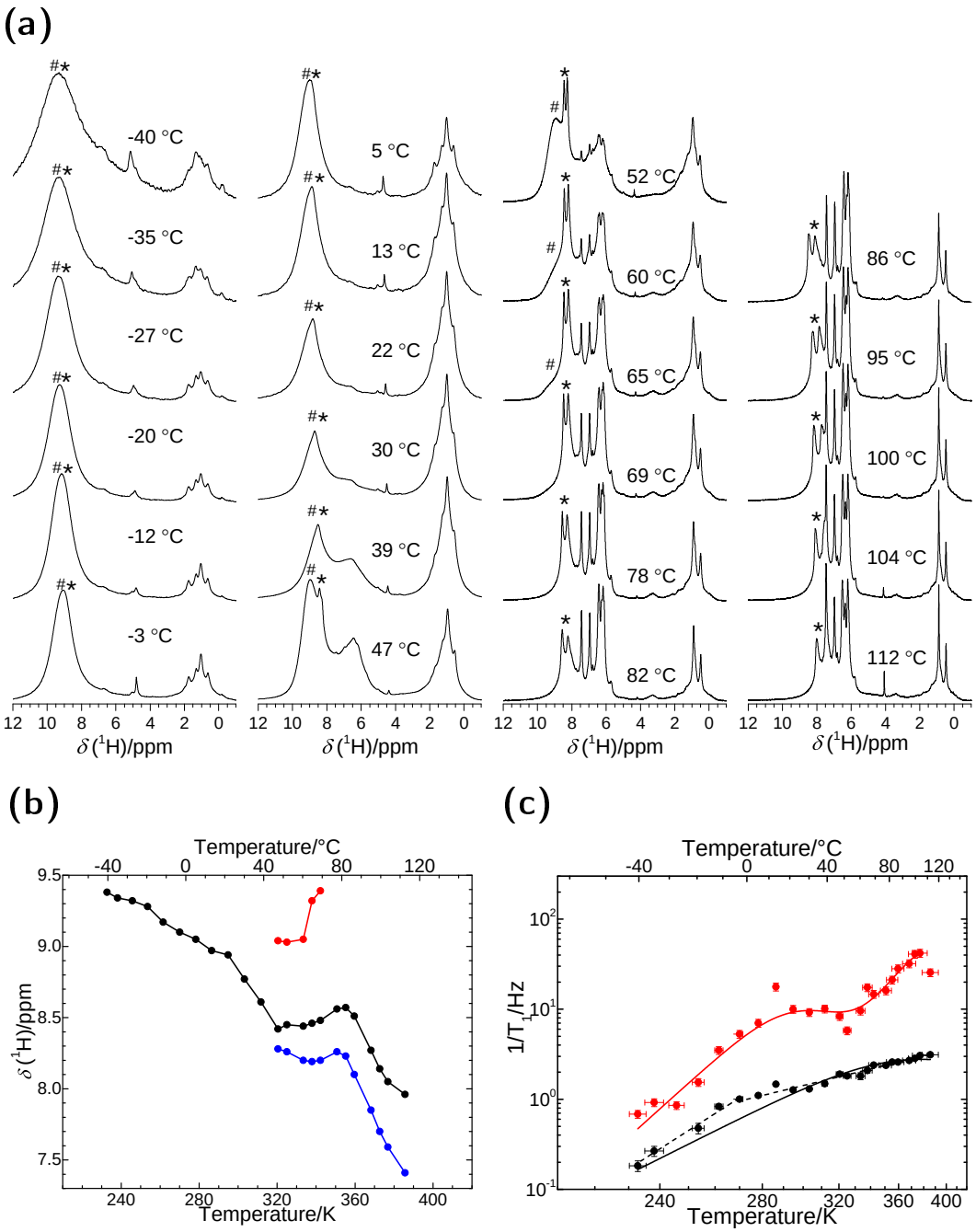

Figure 4.6: The ^{1}H spin echo MAS data of C18-mNb_2O_5(NSF) between -40 °C and 112 °C is shown in (a), where the resonance assigned to the conduction ^{1}H species associated with the NSF SO_3H moieties and conduction H species from the Nb_2O_5 pore wall are labelled with with an asterisk (∗) and a hash (#). The change in ^{1}H chemical shift with temperature of the asterisk and hash marked resonances are shown in (b) in black and red, respectively. The change in T_1 with temperature of the asterisk labelled resonance is shown in (c) with the two T_1 components of this resonance shown in black and red. The T_1 data has been fitted to the BPP model.

at below 40 °C and the other above. Both these regimes can be fitted separately using the BPP model though the energy barrier of the temperature regime above 40 °C is consistently higher than that below 30 °C as can be seen in 4.2.

The temperature at which this change in the T_1 behaviour occurs at 30 °C is very similar to the appearance of two conduction resonances in chemical shift data discussed previously. As that effect is likely caused by the dissociation of NSF from the pore walls it is consistent that this would also affect the T_1 behaviour of the sample. This could also explain the T_1 data from C12-mTa_2O_5(NSF), C18-mTa_2O_5(NSF) and C6-mNb_2O_5(NSF) which become very erratic and in the case of C18-mTa_2O_5(NSF) completely uninterpretable using the BPP model. The complexity of the proton motion resulting from the molecular motion of NSF in the pores means there is no single barrier to proton motion and therefore the BPP model is not applicable.

4.4 Proton MAS PFG

Samples of C12- and C18-mNb_2O_5(NSF) were investigated using a stimulated echo pulsed field gradient (STE-PFG) experiment of protons while spinning at a MAS frequency of 20 kHz on a Bruker 750 MHz spectrometer. The attenuation curve due to proton diffusion of C12-mNb_2O_5(NSF) was measured at temperatures between 20 to 100 °C and is shown in figure 4.7a. The PFG attenuation of C18-mNb_2O_5(NSF) could only be measured between 60 °C and 80 °C. Measurements at temperatures below 60 °C were attempted but could not be acquired. It is speculated that at lower temperatures the diffusion was too slow for the apparatus to measure and at higher temperatures the sample breaks down. The measured diffusion coefficients are shown in table 4.3. The diffusion coefficients of C12- and C18-mNb_2O_5(NSF) are plotted against temperature as an Arrhenius plot in figure 4.7c. The diffusion coefficients of mNb_2O_5(NSF) are compared on an Arrhenius plot to Nafion, water, NSF and mTiO_2(NSF) plotted in the same figure. The latter two samples which were also discussed in chapter 3.

In the STE-PFG NMR MAS spectra of mNb_2O_5(NSF) a single resonance

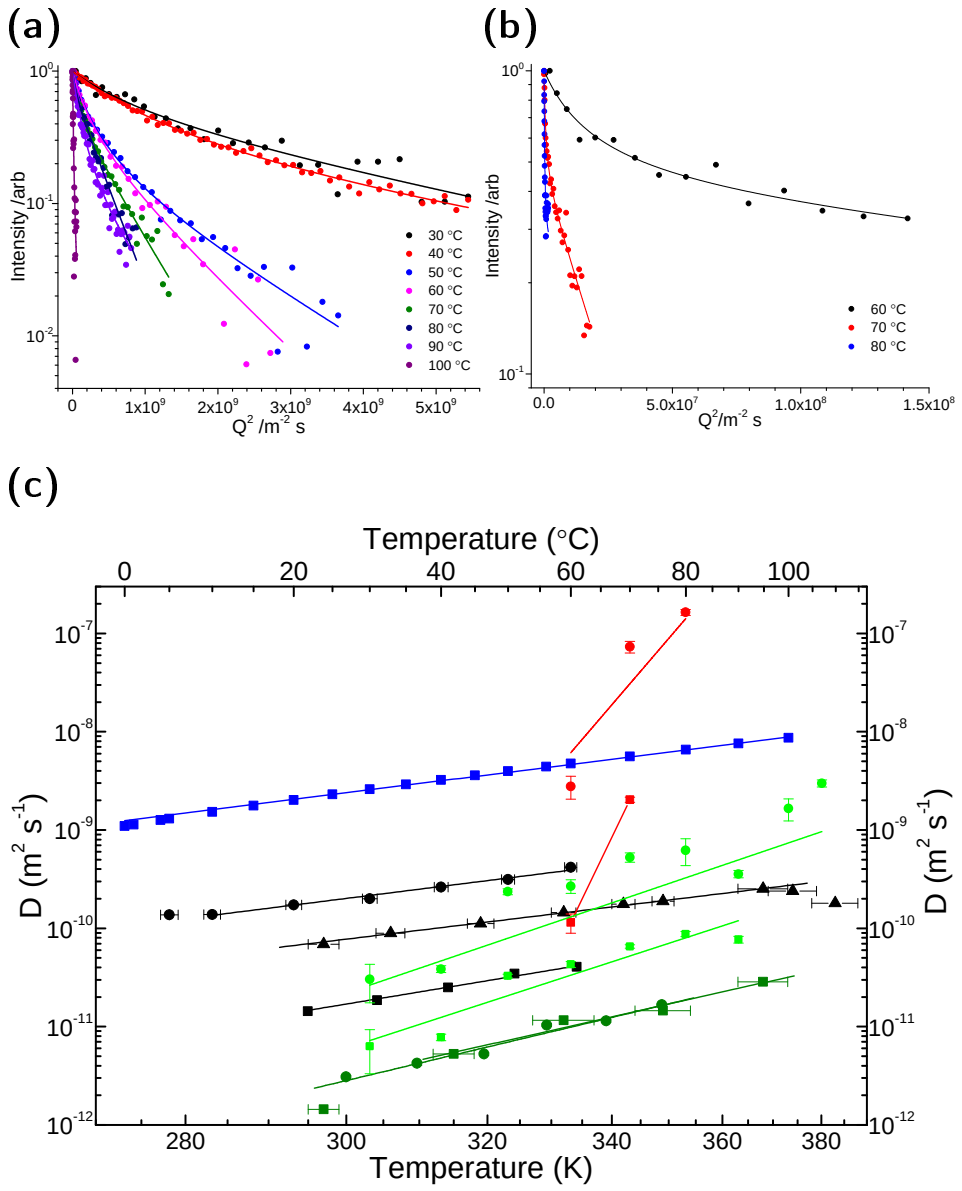

Figure 4.7: The ^{1}H STE-PFG attenuation of C12-mNb_2O_5(NSF) and C18-mNb_2O_5(NSF) due to self diffusion are shown in figures (a) and (b). The temperature is 30 °C (black), 40 °C (red), 50 °C (blue), 60 °C (magenta), 70 °C (dark green), 80 °C (navy blue), 90 °C (violet) and 100 °C (purple). The MAS rotation frequency was 20 kHz using a Bruker 3.2 mm HXY probe in a spectrometer operating at a ^{1}H $\omega_0 = 750$ MHz. The corresponding Arrhenius plot of C12-mNb_2O_5 (red) as well as C18-mNb_2O_5 (green) is shown in figure (c). Additionally, the Arrhenius plot of NSF (dark green), water (blue) and Nafion (black).

is observed at all temperatures. In the spin echo NMR spectra in section 4.3 there clearly are two resonances which arise from protons in hydrogen bonded environments at temperatures between 20 °C and 60 °C. Therefore only protons in one of these hydrogen bonded environments contributes to the proton diffusion between these temperatures. This resonance is associated with the NSF sulfonate as the Nb_2O_5 does not exhibit proton conduction separately from NSF. However, at temperatures below 20 °C it is possible that there is exchange between NSF and the pore wall. This description is consistent with proton diffusion occurring between adjacent NSF moieties with use of the pore wall to link between NSF moieties. However, there it appears that the proton diffusion never occurs independently on the pore wall.

It is observed in figure 4.7a that the attenuation in the PFG-STE experiment is not a straight line and therefore must be described by more than one diffusion coefficient. There are several models which give rise to such behaviour for a single diffusing species. Models which were attempted but discarded include diffusion in randomly distributed pipes and slow exchange between regions resulting in two diffusion coefficients. The former because it yielded non-physical answers and the latter because it did not simulate the either extreme of attenuation curve.

The model which best describes this data is the exchange and diffusion of protons between two sites. The assumptions and mathematical description and derivation of this model is given in section 2.10.4 and yields the following form for the attenuation,

$$E(g) = \exp\left(-\gamma^2\delta^2 g^2 \Delta\left[D_2 + \frac{P_1 D_1}{\gamma^2\delta^2 g^2 \tau_2 P_1 D_1 + 1}\right]\right), \qquad (4.1)$$

where γ is the proton gyromagnetic ratio, δ is the length of the gradient pulse, g is the maximum strength of the gradient pulse and Δ is the length of time protons diffuse. D_2 is the diffusion rate in region two, P_1D_1 is the diffusion rate in region one multiplied by the probability of finding the proton in this region and τ_2 is the average time a proton spends in region two. The latter three parameters are used to fit the model to the experimental data.

This model describes attenuation in PFG-STE experiment of a species diffusing between two types of sub-regions with different diffusion rates which are randomly distributed in a larger area. More precisely the assumption is that diffusion in the first sub-region, D_1, is substantially quicker than the second, D_2. Under these conditions it is only possible to extract the slower of two diffusion coefficients, D_2. The faster diffusion coefficient, D_1, can only be extracted as a product with P_1, the probability of finding the proton in the fast diffusing sub-region. However, this does give a lower limit on this diffusion rate as P_1 being a probability will always be less than 1. Furthermore, the energy barrier of the slow diffusion is likely to be the rate limiting step for proton diffusion and this value is extracted. This model fits all the collected data from the mNb_2O_5(NSF) samples extremely well as seen in figure 4.7a particularly considering it only needs three search parameters.

This model of fast and slow diffusing regions is consistent with the observation that protons diffuse primarily between NSF sulfonate moieties with the sulfates on the Nb_2O_5 pore wall providing a bridge between the NSF moieties. In this scenario the interaction between NSF and the pore wall is weak in certain regions and thus this bridging cannot occur and proton diffusion is forced to proceed mostly directly between NSF moieties. By contrast there is regions where the NSF is arranged such that there is a strong interaction between it and the pore wall. This allows the pore wall bridging between NSF moieties to occur frequently and assuming this type of proton transfer is faster leads to a higher proton diffusion rate.

The energy barriers to proton mobility were calculated from the diffusion coefficients in the Arrhenius plot in figure 4.7c. For C12-mNb_2O_5(NSF) the energy barrier for the slower diffusion coefficient, D_2, is 48 ± 1 kJ mol^{-1} while that of C18-mNb_2O_5(NSF) appears to be in excess of 100 kJ mol^{-1}. Both of these energy barriers to diffusion are higher than the D_2 for mTiO_2(NSF) which is measured at 35 ± 3 kJ mol^{-1} and pure NSF measured at 30 ± 4 kJ mol^{-1}. All of these again exhibit higher energy barriers to proton diffusion than Nafion 22 ± 2 kJ mol^{-1} [53] and water 16.5 ± 0.2 kJ mol^{-1} [106] which are consistent with literature values.

Table 4.3: The diffusion coefficients of C12-mNb_2O_5(NSF) and C18-mNb_2O_5(NSF) measured using STE-PFG NMR MAS at temperatures between 30 °C and 100 °C.

Temperature	C12-mNb_2O_5(NSF)		C18-mNb_2O_5(NSF)	
	D_2 /m^2 s^{-1}	P_1D_1 /m^2 s^{-1}	D_2 /m^2 s^{-1}	P_1D_1 /m^2 s^{-1}
30 C	$(6 \pm 2)\times10^{-12}$	$(1.8 \pm 0.3)\times10^{-11}$		
40 C	$(4 \pm 1)\times10^{-12}$	$(2.10 \pm 0.08)\times10^{-11}$		
50 C	$(1.9 \pm 0.4)\times10^{-11}$	$(9.4 \pm 0.5)\times10^{-11}$		
60 C	$(3.0 \pm 0.6)\times10^{-11}$	$(9.0 \pm 0.6)\times10^{-11}$		
70 C	$(5.2 \pm 0.4)\times10^{-11}$	$(1.74 \pm 0.09)\times10^{-10}$	$(5 \pm 5)\times10^{-11}$	$(1.1 \pm 0.2)\times10^{-9}$
80 C	$(8.3 \pm 0.6)\times10^{-11}$	$(1.8 \pm 0.3)\times10^{-10}$	$(1.5 \pm 0.2)\times10^{-9}$	$(3.2 \pm 0.4)\times10^{-8}$
90 C	$(3 \pm 2)\times10^{-11}$	$(2.0 \pm 0.1)\times10^{-10}$	$(0 \pm 2)\times10^{-9}$	$(1.2 \pm 0.1)\times10^{-11}$
100 C	$(0 \pm 2)\times10^{-10}$	$(2.7 \pm 0.3)\times10^{-9}$		

There appears to be a clear trend in the thermal dependence of the diffusion coefficients, D_2, of NSF containing samples seen in figure 4.7c. The energy barrier of NSF is lower when it is pure than when it is impregnated into metal oxides in all cases. This suggests that the pathway which leads to rapid proton diffusion rate includes intermediary steps between the proton transfer between moieties leading to diffusion in mNb_2O_5(NSF). Such an intermediary step is likely to be a rotation or reorientation of the sulfonate on pore wall in order to bring the diffusing proton into proximity with the following NSF moiety. Therefore while the overall energy barrier to diffusion measured by the PFG experiment increases this in fact represents many lower energy barriers which combined must be overcome by thermal activation before actual proton transfer between adjacent moieties occurs and leads to proton diffusion.

The energy barriers calculated from T_1 for mNb_2O_5(NSF) using the Arrhenius and BPP models in section 4.3 are 18 ± 1 kJ mol^{-1} for C12-mNb_2O_5(NSF) as well as 33 ± 4 and 53 ± 28 kJ mol^{-1} for C18-mNb_2O_5(NSF). These are consistently lower than the values obtained measuring self diffusion using PFG NMR. This is consistent with the diffusion process being composed of several separate intermediary steps. Each such step will have associated with it a certain characteristic frequency which corresponds to the rate at which the process occurs. However, the motions which affect the T_1 relaxation rate most occur at a rate which is comparable to the proton Larmor frequency, specifically when

$$\tau_c \omega_0 = 1 \tag{4.2}$$

where τ_c is the characteristic rate of the motion and ω_0 is the proton Larmor frequency is satisfied. Therefore, in a system where the process leading to proton diffusion consists of multiple steps it is inevitable that some steps in the process contribute more to the T_1 relaxation. It also follows that the energy barrier measured using this technique must be lower (or at most equal) to the value measured using PFG.

The lower limit of the rate of proton diffusion, P_1D_1, is of the order of 3×10^{-7} m^{2}s^{-1} for C18-mNb_2O_5(NSF) at 80 °C which is 20 times faster than the

diffusion rate measured in H_2O at the same temperature and at least three orders of magnitude quicker than the fastest proton diffusion measured in Nafion. At this temperature the slower rate of proton diffusion, D_2, is 10^{-9} m^2s^{-1} which is two orders of magnitude slower is still an order of magnitude quicker than even the fastest measurements of Nafion. However, this slower rate of diffusion, D_2, dramatically decreases above 80 °C while the faster diffusion rate, P_1D_1 continues to increase. This is consistent with thermal motion detatching the NSF chains from the support of the pore wall surface. This results in the fast P_1D_1 being the diffusion rate along the chain being unaffected but the diffusion between chains is disrupted and thus D_2 is greatly reduced. Furthermore, the diffusion rate of pure NSF only starts to decline when the temperature reaches above 100 °C. This suggests that the reduction in diffusion rate seen in mNb_2O_5(NSF) is not due to the disruption of the NSF itself but the disruption of the interaction between the pore surface and the NSF.

The diffusion rates measured for C12-mNb_2O_5(NSF) are 10^{-10} m^2s^{-1} for the P_1D_1 and 5×10^{-11} m^2s^{-1} for D_2 which is slower than for C18-mNb_2O_5(NSF). However, they still exceed measurements of Nafion at temperatures above 70 C. This suggests that the smaller pore size of 24 Å of C18-mNb_2O_5(NSF) favours rapid proton diffusion compared to C12-mNb_2O_5(NSF) which have pores size of 39 Å. However, the diffusion rate of D_2 is greatly reduced above 80 °C which is the same behaviour seen for C18-mNb_2O_5(NSF) and therefore consistent with D_2 being the diffusion rate between NSF chains. Additionally, the proton diffusion of the mNb_2O_5(NSF) samples are higher than that measured for $mTiO_2$(NSF). This suggests that the sulfonation of the mNb_2O_5 pore surface enhances the proton diffusion pathways compared to $mTiO_2$. Furthermore, the temperature at which proton diffusion rate D_2 is reduced is higher in mNb_2O_5(NSF) at 80 °C compared to $mTiO_2$(NSF) at 50 °C. Therefore, mNb_2O_5 is more thermally stable than $mTiO_2$ despite higher pore wall acidity which enhances proton diffusion.

4.5 Oxygen Spin Echo

Figures 4.8a to 4.11a show the ^{17}O spin echo spectra of C6-, C12-, and C18-mNb_2O_5(NSF) as well as C12-mTa_2O_5(NSF) which have been enriched with ^{17}O. The spectra have been acquired at three magnetic field strengths of 7.05 T, 11.75 T and 14.05 T which is equivalent to ^{17}O Larmor frequencies of 40.69 MHz, 67.78 MHz and 81.37 MHz. These spectra each show 3 resonances which have been simulated using DMfit [107] and their chemical shifts are shown in table 4.4. Figures 4.8b to 4.11b and 4.8c to 4.11c show the MQMAS spectra of these samples acquired at 11.75 T or ^{17}O $\omega_0 = 67.78$ MHz.

The sample with the most well resolved ^{17}O spin echo spectra at all field strengths is C12-mTa_2O_5(NSF) shown in figure 4.11a. In this spectra the resonance at ^{17}O $\delta \approx 15$ ppm is assigned physio adsorbed water as there are no other oxygen containing compounds which come at this chemical shift. In this spectra one resonance at δ $^{17}O \approx 450$ ppm which is assigned to the OTa_2 environment in the mesoporous tantalum oxide framework [108]. The width of the resonance is 1860 Hz which is consistent with the work of Rao et al. [108]. Furthermore, this chemical shift is very consistent across several magnetic fields which suggests that the quadrupolar constant, C_Q, for this oxygen environment is low. This is unexpected in a metal oxide where oxygen mobility is not considered likely. There is an absence of a resonance at ^{17}O $\delta \approx 310$ ppm which is assigned to ^{17}O in a OTa_3 environment. This suggests that the oxygen in mTa_2O_5 examined here is less coordinated which may be due a greater prevalence of less coordinated surface oxygen.

The resonances observed at ^{17}O $\delta \approx 160$ ppm is assigned to sulfonate (R-SO_3^-) or sulfate (SO_4^{2-}) oxygen environments which have been shown to be between 100 to 170 ppm [109, 110]. Both sulfonate from the NSF and the sulfate on the pore walls appear very close in chemical shift and very difficult to distinguish. In figure 4.11ac depicting the spin echo at 14.05 T a second resonance at the right can be observed emerging. This shows that there are indeed two different but similar ^{17}O environments which are only resolved at high magnetic field. The sulfonate ^{17}O resonances have been shown to have a width of

approximately 6 MHz with a standard quadrupolar lineshape at ambient temperature in amino acids [109]. The chemical shift of this resonance is exactly the same. However, in figure 4.11a the resonance has a width of 630 Hz at 7.05 T with none of the usual quadrupolar features. This must be due to sulfonate having much higher motion likely due to the rotation around the 3-fold axis having a much lower energy barrier. This is important as the reorientation of hydrogen bonding sites have been shown to be extremely important for proton conductivity [111]. The third resonance appearing at 15 ppm is most likely due to residual OH species from the polymerisation of the sample.

The MQMAS in figure 4.11b and 4.11c shows ^{17}O resonances which correspond to the sulfonate and sulfate resonances at $\delta \approx 160$ ppm and water $\delta \approx 15$ ppm. No resonance assignable to OTa_2 is present at 450 ppm most likely due to insufficient signal to noise. The resonance at 160 ppm is clearly revealed to be two separate resonances which which is consistent with the spin echo at 14.05 T where a second resonance also appears thus suggesting there are two distinct acidic sulfate environments. Additionally, a resonance is present in the MQMAS spectrum corresponding to the residual OH at approximately 0 ppm.

The spin echo spectra of C12-mNb_2O_5(NSF) at three magnetic fields are shown in figure 4.8a. The resonances in these spectra have significantly worse signal to noise as well being less well resolved when compared to the spectra of C12-mTa_2O_5(NSF). At all three fields a resonance is present at ^{17}O $\delta \approx 575$ ppm. This resonance is assigned to oxygen in a ONb_2 environment [108]. The resonance width has been measured as 3540 Hz. Like for the tantalum sample there is no resonance present which can be assigned to a ONb_3 environment which has been observed previously [108].

Two resonances at ^{17}O $\delta \approx 100$ ppm and 130 ppm are present in the spectrum of C12-mNb_2O_5(NSF) but only at some magnetic fields. These resonances are due to sulfonate and sulfate oxygen environments [110]. However, at 7.05 T the resonance present is at 100 ppm with possibly a remnant of a resonance of very low intensity at 130 ppm. However, at 11.75 T there appears to be two resonances but they are not well resolved. The spectrum at 14.05 T shows that the resonance at 130 ppm completely dominates with the resonance 100 ppm no

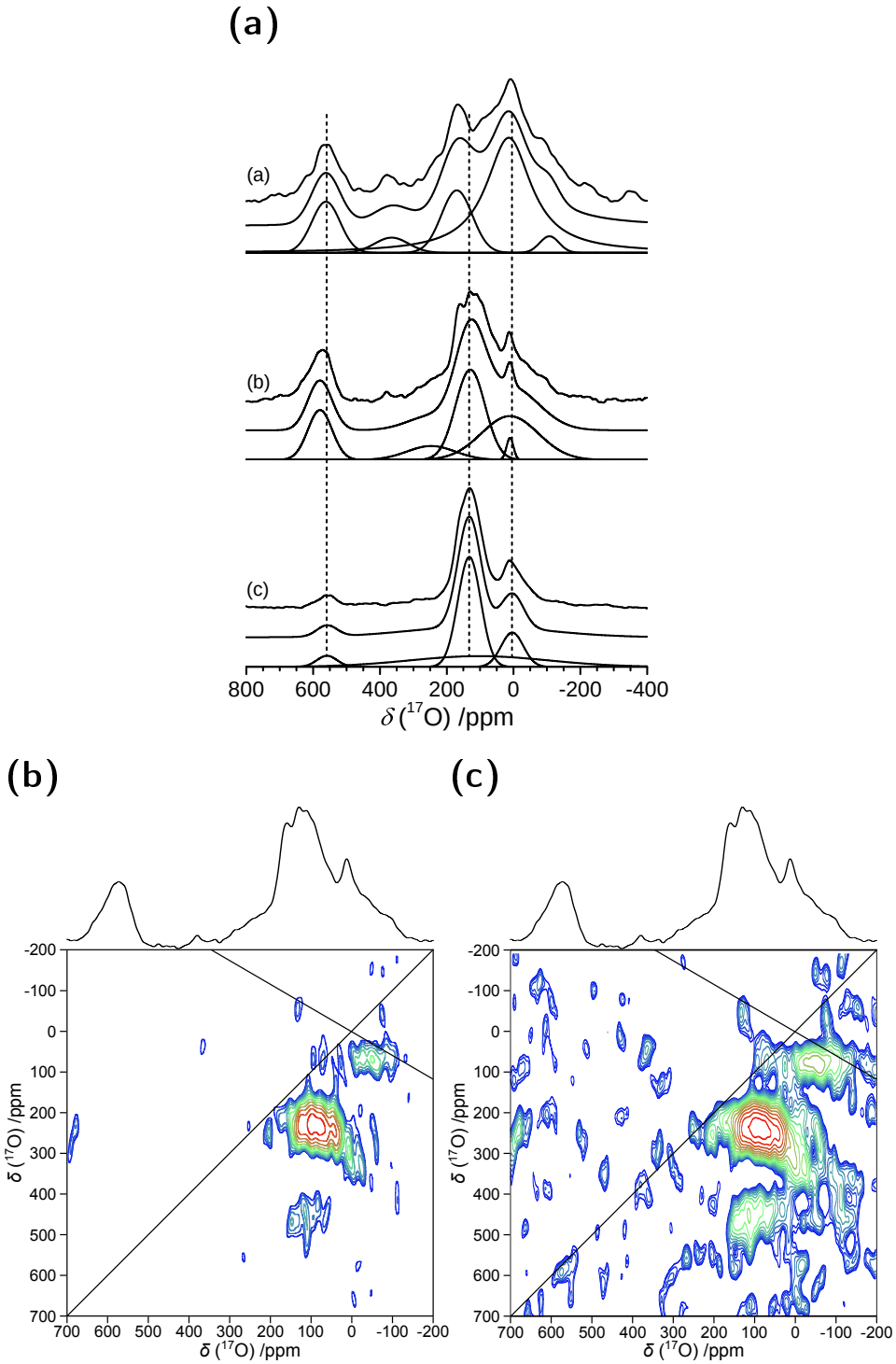

Figure 4.8: In figure (a) is shown the ^{17}O spin echo MAS NMR of C6-mNb_2O_5(NSF) acquired at (a) 40.69 MHz (b) 67.78 MHz and (c) 81.37 MHz. In figures (b) and (c) is shown the MQMAS acquired at 67.78 MHz with the contour levels of figure (c) beginning at a lower level.

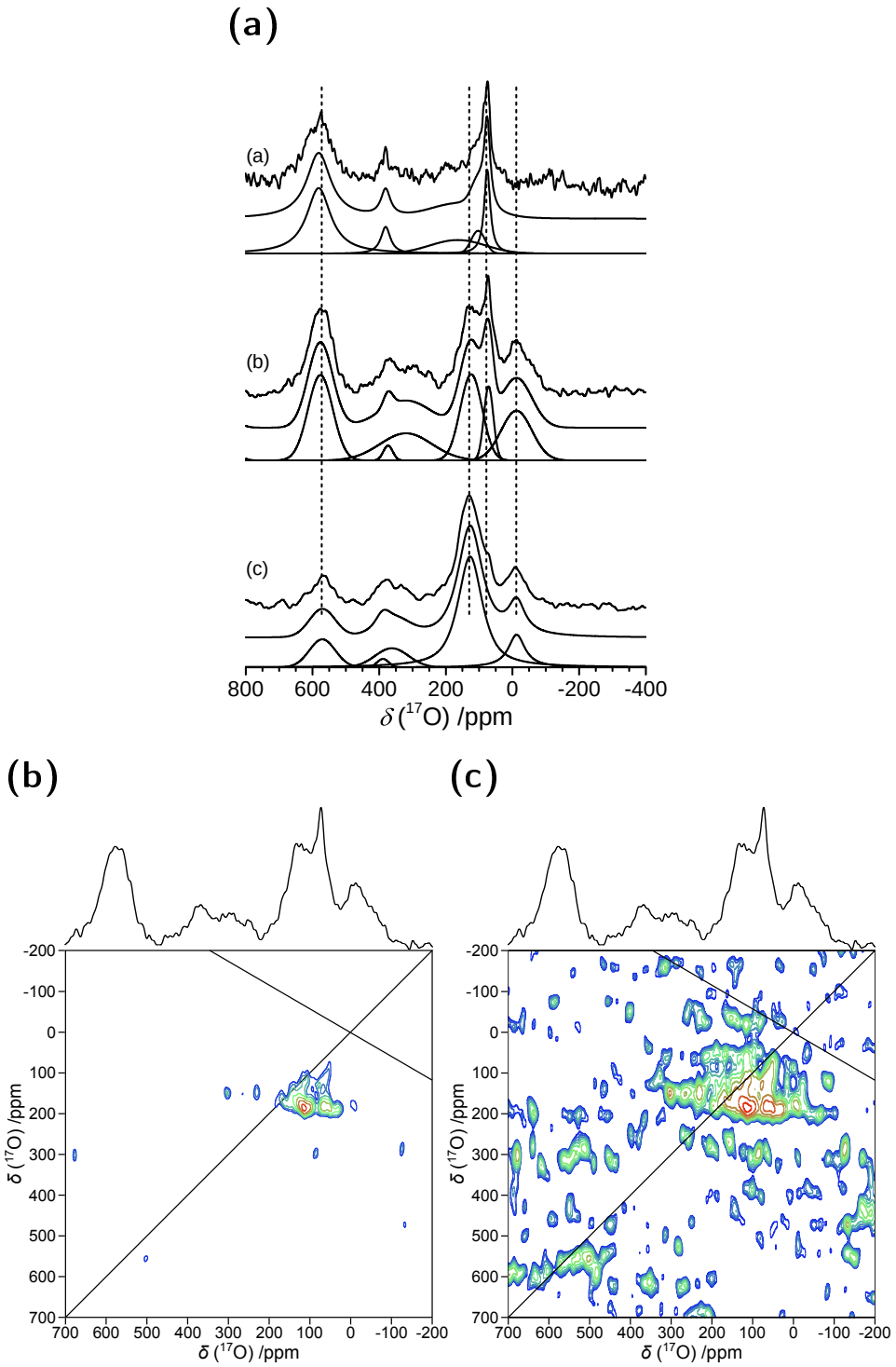

Figure 4.9: In figure (a) is shown the ^{17}O spin echo MAS NMR of C12-mNb_2O_5(NSF) acquired at (a) 40.69 MHz (b) 67.78 MHz and (c) 81.37 MHz. In figures (b) and (c) is shown the MQMAS acquired at 67.78 MHz with the contour levels of figure (c) beginning at a lower level.

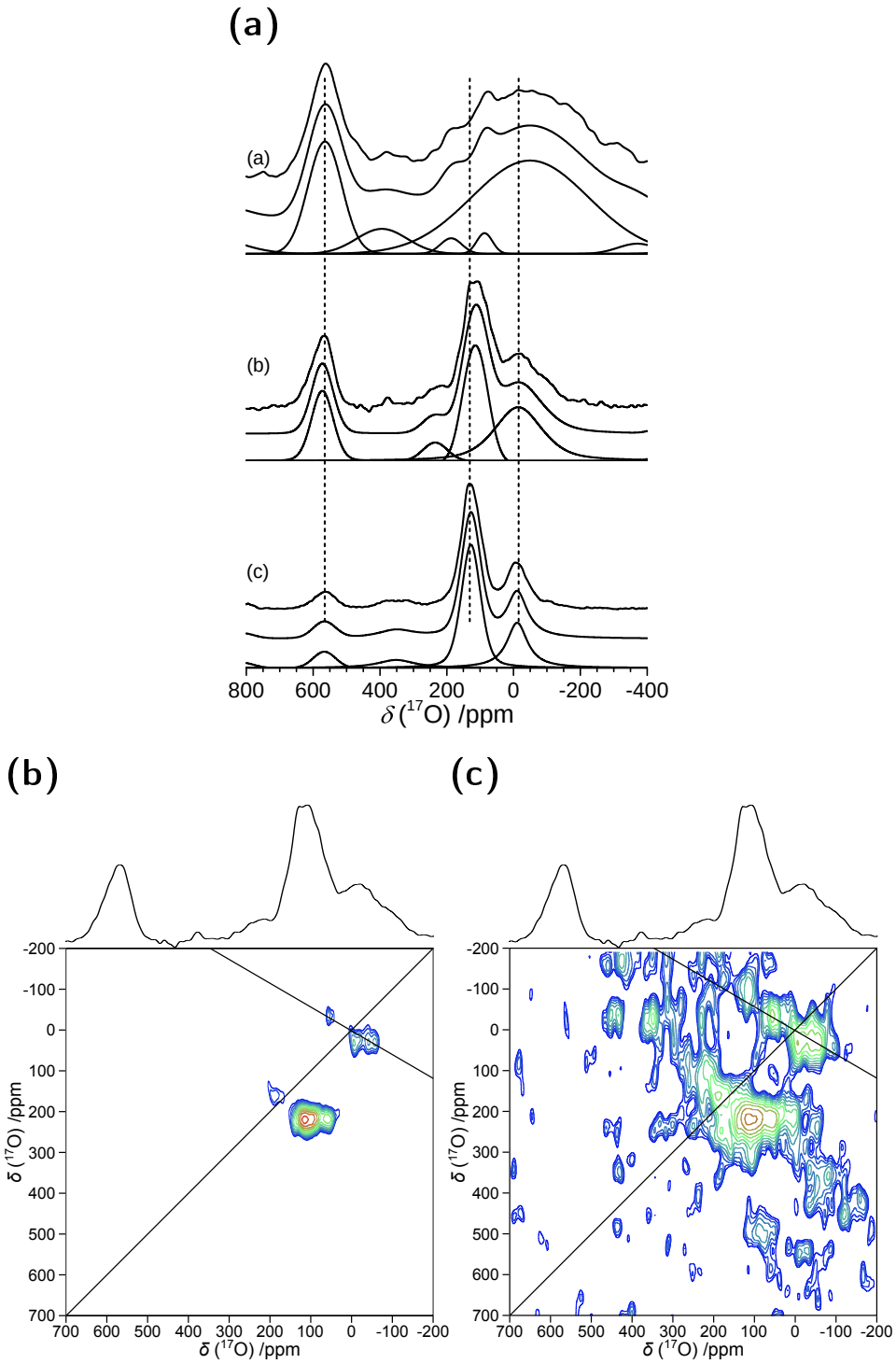

Figure 4.10: In figure (a) is shown the ^{17}O spin echo MAS NMR of C18-mNb_2O_5(NSF) acquired at (a) 40.69 MHz (b) 67.78 MHz and (c) 81.37 MHz. In figures (b) and (c) is shown the MQMAS acquired at 67.78 MHz with the contour levels of figure (c) beginning at a lower level.

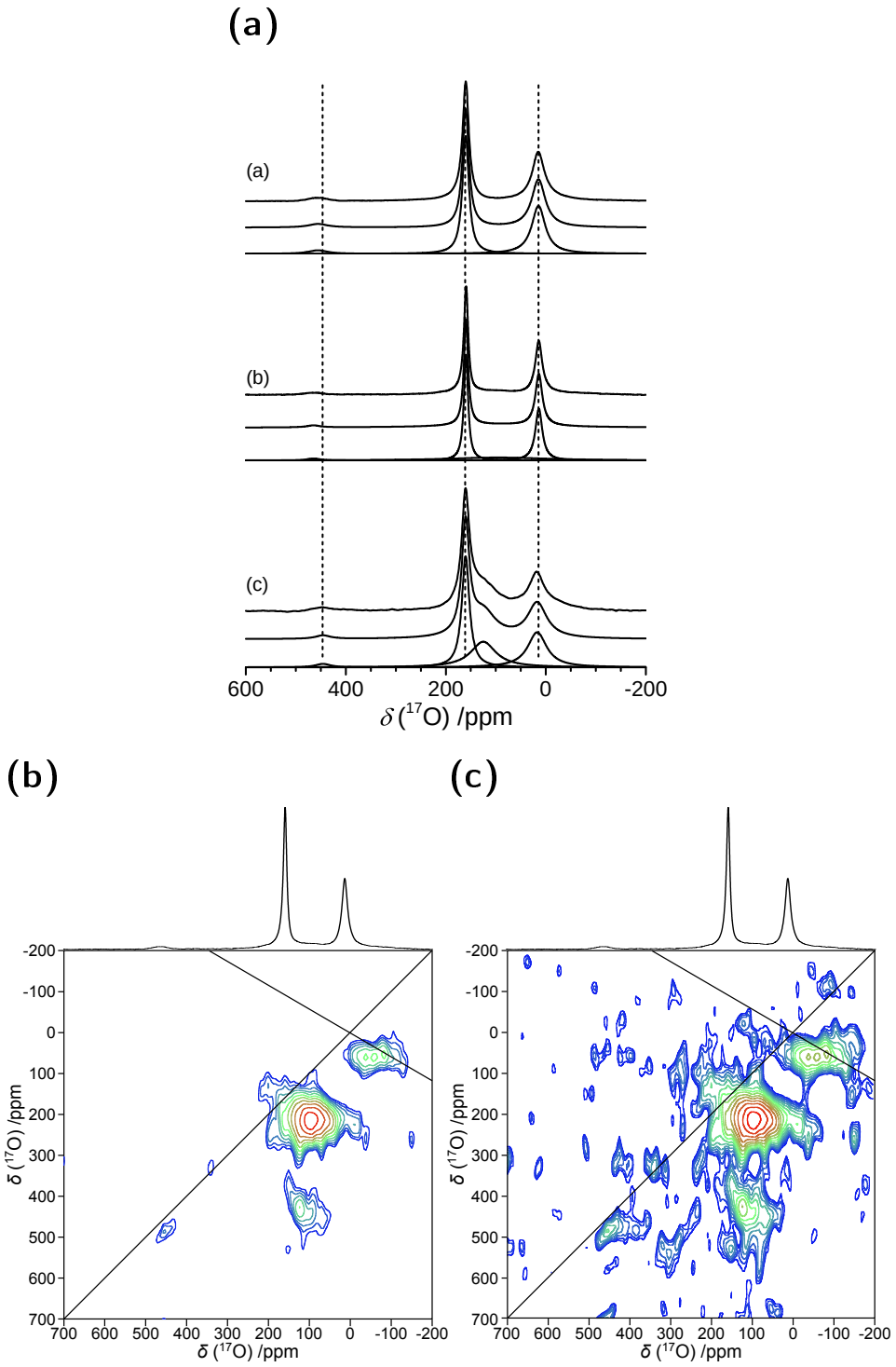

Figure 4.11: In figure (a) is shown the ^{17}O spin echo MAS NMR of C12-mTa_2O_5(NSF) acquired at (a) 40.69 MHz (b) 67.78 MHz and (c) 81.37 MHz. In figures (b) and (c) is shown the MQMAS acquired at 67.78 MHz with the contour levels of figure (c) beginning at a lower level.

Table 4.4: The ^{17}O chemical shift from the spin echo spectra of C6-, C12- and 18C-Nb_2O_5(NSF) as well as C12-Ta_2O_5(NSF) acquired at the magnetic field strengths of ^{17}O ω_0 of 40.69 MHz, 67.78 MHz and 81.37 MHz. The spin echo spectra are shown in figures 4.8a to 4.11a respectively.

Sample	Magnetic Field Strength		
	40.69 MHz	67.78 MHz	81.37 MHz
C6-Nb_2O_5 δ (^{17}O)\ppm	14	11	4
	109	130	132
	562	579	558
C12-Nb_2O_5 δ (^{17}O)\ppm	21	72	60
	103	128	127
	581	576	570
C18-Nb_2O_5 δ (^{17}O)\ppm	-49	-16	-11
	-	114	128
	564	572	566
C12-Ta_2O_5 δ (^{17}O)\ppm	15	14	17
	160	160	160
	456	464	446

longer appearing. This suggests that there are two sulfate based environments present like for C12-mTa_2O_5(NSF). A resonance is present at a 0 ppm but only at the higher fields of 11.75 T and 14.05 T. Its chemical shift suggests that it is due to residual OH released during polymerisation of the sample. This resonance appears to be missing at 7.05 T but this may be due to insufficient signal to noise in the spectra.

The MQMAS spectrum of C12-mNb_2O_5(NSF) is shown in figures 4.9b and 4.9c. This spectrum shows a resonance between 100 and 130 ppm. Like the spin echo spectra of this sample the resolution of the spectrum is not sufficient to determine whether there are one or two resonances. In this spectrum no resonances appear to correspond to the Nb_2 resonance at 575 ppm and the 0 ppm resonance of residual water which are present in the spin echo spectra.

The ^{17}O spin echo spectra of C6-mNb_2O_5(NSF) at three magnetic fields is shown in figure 4.8a. At 560 ppm is observed a resonance which is assigned to an ONb_2 environment. However, no resonace for the ONb_3 environment is found unlike Rao et al [108] but consistent with the other samples in this work.

There is only a single resonance at 130 ppm which can be assigned to sulfate and sulfonate oxygen environments. However, a second resonance is resolved at 120 ppm in the MQMAS in figure 4.8b such that distinct sites for sulfate and sulfonate are resolved in this sample like in C12-mNb_2O_5(NSF) and C12-mTa_2O_5(NSF). A resonance at 0 ppm is assigned to residual OH produced from the polymerisation. In the MQMAS no resonance is present from the ONb_2 resonance at 560 ppm but a resonance is present which matches the residual OH resonance at 0 ppm.

The ^{17}O spin echo spectra of C18-mNb_2O_5(NSF) at three magnetic fields are shown in figure 4.10a. A resonance at 565 ppm is assigned to a ONb_2 environment. At 11.75 T and 14.05 T two resonances are resolved at 130 ppm and 0 ppm. These are assigned to sulfonate and residual OH from polymerisation. However, in the spin echo spectra acquired at 7.05 T they appear to merge into a single broad resonance. The MQMAS acquired at 11.75 T shown in figures 4.8b and 4.8c show these two resonances as resolved as well. However, there is no resonance corresponding to the ONb2 at 565 ppm in the MQMAS. Neither is there a second resonance observed near 130 ppm like for C6-mNb_2O_5(NSF) and C12-mTa_2O_5(NSF). This suggests unlike other samples in this work there is only a single sulfonate environment. This could be because the the Nb_2O_5 was sulfonated less other samples.

4.6 Conclusion and Further Work

The spin echo MAS NMR spectra of mTa_2O_5(NSF) and mNb_2O_5(NSF) show clear signs of motional narrowing when the temperature reaches 50 °C. Aromatic resonances which should be subject to strong dipolar broadening become extremely narrow. This motion of NSF is the likely cause of the disruption of the hydrogen bonded network when it changes from being represented by a single resonance to splitting into two resonances. This process starts between 20 °C and 30 °C but continues until approximately 70 °C where one of the resonances disappears completely. This is when all contact between NSF and the pore walls cease. This

is consistent with the PFG MAS NMR diffusion measurements which show a significant drop in the diffusion rate above 80 °C.

Proton spin echo and PFG NMR data is consistent with the diffusion process occurring predominantly between NSF moieties with the sulfates on the pore wall bridging occasionally. The diffusion process consists of several independent steps some of which do not result in proton diffusion but require thermal activation. It is suggested such a step is likely to be the reorientation of sulfate before a proton can be transferred to the next moiety in the chain. This results in the measurement of different energy barriers to proton motion when using T_1 relaxation and PFG MAS NMR.

The samples of mNb_2O_5(NSF) and mTa_2O_5(NSF) show excellent diffusion rates which exceed even the industry standard of Nafion at 80 °C. However, it still suffers from thermal degradation due to NSF mobility at these temperatures. This should not be an impossible problem to overcome. It is plausible to modify NSF in order to reduce motion possibly by increasing the chain length or anchoring it in the pore to stabilise the proton conduction material at higher temperatures.

Chapter 5

The Protein-Ice Interface of Anti-Freeze Molecules

Naturally occurring anti-freeze proteins (AFPs) inhibit ice crystal growth by lowering the freezing temperature of water in internal fluids below the melting temperature. This is a process called thermal hysteresis and the difference between freezing and melting temperature is called the hysteresis gap. This effect was first reported in 1964 [112], but the phenomenon was not explained in its modern context until a few years later in the bodily fluids of polar fish [113, 114]. It has since been reported in a wide range of organisms including arthropods [115] plants [116], fungi and bacteria [117, 118]. Currently, the most studied anti-freeze proteins are extracted from polar fish where five different groups of anti-freeze proteins have been isolated. One group consists of anti-freeze glycoproteins and four remaining groups anti-freeze proteins termed type I-IV which are differentiated by biochemical properties and homology considerations [119]. In particular AFP type III has been studied in detail and is the antifreeze protein used herein.

AFPs inhibit ice crystal via adsorption and growth inhibition mechanism [120, 121]. AFPs bind to specific ice crystal planes which leads to ice crystal growth termination, a phenomenon called the Kelvin effect [121, 122]. The ice binding site pf AFP type III has been identified and found to be a convex surface

containing many non-polar residues using x-ray diffraction [123], solid state NMR [124–126] and mutagenesis [123, 127, 128]. The non-polar residues at the ice binding site were found by neutron diffraction to fit into holes on the ice crystal surface [129] which is critical to anti-freeze activity of the protein [124].

Carrageenans are commercially extracted from a species of red seaweed called Rhodophyta [130]. They are one of the principal thickening and gelling agents in the commercial food industry, notably for diary products [130], but have also found a wide variety of uses in diverse areas such as additives to cosmetics and oil well fluids [130]. It has been shown when carrageenans are added to water they act as an antifreeze lowering the freezing temperature [131]. Due to the proliferation of frozen foods the interest in using compounds which protects the frozen cell from bursting and thus preserving the texture are interesting. This work focuses on investigating the means by which APF III and carrageenan compounds achieve their effect of lowering the freezing point of water below 0 °C and preventing the formation of large ice crystals.

All carrageenans are linear chains of polysaccharides, specifically 3,6 anhydrogalactose which can be both sulphated and unsulphated. The units are joined by alternating α-1,3 and β-1,4 glycosidic linkages [130]. The main varieties of carrageenan are differentiated by the number of sulphonations. Carrageenans with a one, two and three sulphate substitution are termed κ-, ι- and λ-carrageenan, respectively [130]. However, the location and stereochemistry of these sulfonations further differentiates these carrageenans into numerous subgroups.

In this chapter the interaction between the solid or liquid water phase and a AFP of type III is studied using ^{1}H-^{1}H EXSY and ^{2}H saturation recovery solid state NMR of AFP III dissolved in H_2O and D_2O. When adding AFP III to D_2O two resonances are detected in the ^{2}H MAS NMR spectrum and assigned to frozen D_2O and liquid D_2O in the hydration shell of AFP III. The T_1 of the resonance assigned to frozen D_2O is reduced from 32 s in pure D_2O to approximately 2 s which is consistent with previous observations and the presence of an ice-protein interface where cross relaxation between protons and deuterium can occur [126]. It has been shown that anti-freeze proteins bound to ice crystals is

sufficient to prevent ice crystal growth [132]. The magnitude of the T_1 reduction depends on the concentration of AFP III which is consistent with the measured hysteresis gap dependence on concentration and thus inhibits ice crystal formation [121]. The ^{1}H-^{1}H EXSY spectra measuring proton spin diffusion shows that there is a clear cross peak between resonances from aliphatic protons in AFP III and ice as expected as non-polar resonances fill the holes in the ice lattice [129]. In contrast, no such change as observed in the T_1 relaxation in the equivalent spectrum where AFP III is replaced by lysozyme.

Four carrageenans were added to D_2O and investigated using ^{2}H saturation recovery T_1 measurements which were compared to those of AFP III added to D_2O. One carrageenan labelled ι exhibited T_1 behaviour like that of AFP III and thus consistent with an interface between ice and carrageenan. Two others, λ- and mixed carrageenan, exhibited T_1 behaviour resembling that of pure D_2O where the whole sample is frozen. It is hypothesized that the carrageenans are frozen into the ice which inhibits the motion necessary to reduce the T_1. The T_1 behaviour of Deltagel suggests that the D_2O is not completely frozen yet like λ-carrageenan there is insufficient motion in order to achieve the reduction in D_2O T_1 as seen with ι-carrageenan and AFP III.

5.1 Experimental Details

All spectra were acquired on a Bruker Avance III spectrometer operating at 11.75 T corresponding to a Larmor frequency of 500.10 MHz and 76.75 MHz for protons and deuterium respectively. A Bruker 4 mm triple channel probe operating in dual channel mode was used and a MAS frequency of 12.5 kHz was achieved. The sample temperature was referenced externally to the chemical shift of lead nitrate.

Saturation recovery spectra $(\tau_{sat}$ - $\pi/2)_n$ - τ_1 - $\pi/2$ were acquired to measure the T_1 of deuterium in D_2O. The temperature was -30 °C referenced externally using lead nitrate [102, 133]. A solid echo τ_R - $\pi/2$ - τ_R was used preceding acquisition to reduce artefacts where the echo delay was equal to

single rotor period $\tau_R = \nu_R^{-1} = 80$ μs. The initial $\pi/2$ excitation pulse was 2.5 μs as were the saturation and echo pulse. A deuterium shift of 0 ppm in D_2O was used as reference.

^{1}H-^{1}H EXSY 2D spectra $\pi/2$ - τ_1 - $\pi/2$ - τ_{mix} - $\pi/2$ were acquired of AFP III and lysozyme in H_2O and D_2O while maintaining a MAS frequency of 12.5 kHz and temperatures of -10 °C and -20 °C measured using lead nitrate as an external reference [102, 133]. A spin echo τ_R - π - τ_R was used preceding acquisition to reduce artefacts where the echo delay was a single rotor period $\tau_R = \nu_R^{-1} = 80$ μs. The $\pi/2$ pulses were 2.5 μs and the mixing time τ_{mix} was 100 ms. The spectra were recorded with 32 transients co-added per t_1 increment the number of which were changed depending on the length of the FID.

^{1}H spin echo spectra $\pi/2$ - τ_R - π - τ_R were acquired of H_2O with 20 mg mL^{-1} AFP III added while maintaining a MAS frequency of 12.5 kHz. The temperature was varied between -10 °C and -30 °C using the external reference of lead nitrate [102, 133]. The excitation $\pi/2$ pulse was 2.5 μs and the echo π pulse was 5 μs. The echo delay was equal to single rotor period $\tau_R = \nu_R^{-1} = 80$ μs. Each spectra was recorded by co-adding 64 transients. All ^{1}H EXSY and spin echo spectra were referenced to alanine, a solid state secondary reference with resonances at 1.3, 3.5 and 8.4 ppm relative to the primary reference of TMS at 0 ppm

5.2 Antifreeze Protein Type III

5.2.1 Deuterium Spin Lattice of Heavy Water with AFP III

Deuterium T_1 recovery curves of D_2O with AFP III were measured at -30°C. The measurements are consistent with Siemer *et al* [126]. They show that the T_1 relaxation of pure D_2O is 36 s while adding AFP III reduces the T_1 by more than order of magnitude to 2 s. This reduction of deuterium T_1 relaxation in D_2O when AFP III is present is proposed to be due to proton deuterium cross relaxation. The proton T_1 in AFP III is transferred via the dipolar coupling to

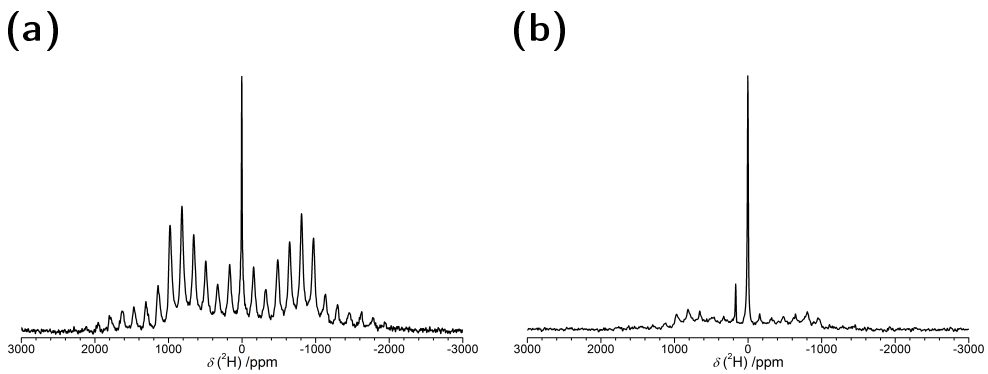

Figure 5.1: The line shape of (a) pure D_2O and (b) D_2O with 20 mg mL^{-1} AFP III. The temperature was calibrated to -30 °C using lead nitrate while maintaining a 12.5 kHz MAS frequency.

the deuterium in D_2O ice at a protein-ice interface [126]. The ^1H T_1 of AFP III is shorter than the ^2H T_1 of ice and the dipolar coupling between two types of spins results in a mixing of their T_1 which means a reduction of the ^2H T_1. This transfer is only possible if the dipolar coupling between protons in AFP III and the deuterium in the ice is strong. If there were a hydration shell with liquid water between the whole surface of the protein and the ice then the dipolar coupling would be weakened too much for this transfer of magnetisation to be observed. Hence, AFP III must have an interface with ice where the dipolar coupling between them is sufficiently strong to observe this effect on the ^2H T_1.

In figure 5.2 and table 5.1 it is observed that when the AFP III weight percentage in D_2O is changed from 10 mg mL^{-1} to 25 mg mL^{-1} the T_1 drops from 3 s to 0.6 s. This supports the hypothesis that AFP III is the cause of the reduction of T_1 in D_2O. When the weight percentage of AFP III is small the fast proton T_1 is diluted among many D_2O molecules and hence the ice deuterium T_1 becomes an average between the D_2O T_1 and the AFP III T_1. As the weight percentage of AFP III is increased this average is shifted towards the AFP III T_1 as its proton bath begins to dominate the equilibrium. In the limit the D_2O T_1 would therefore become the same as the fast AFP III proton T_1.

Another feature observed in the saturation recovery spectra D_2O with AFP III is the presence of narrow resonance at 0 ppm. This resonance exhibits

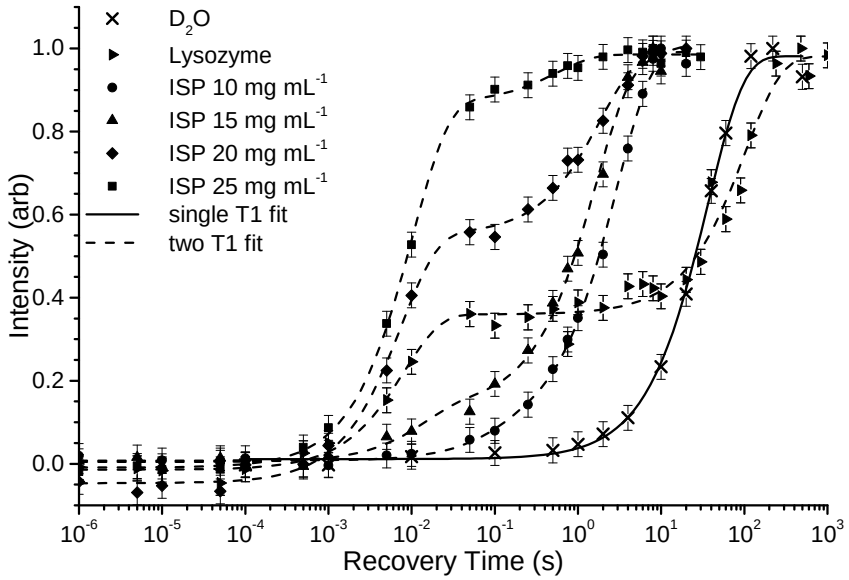

Figure 5.2: The deuterium saturation recovery T_1 with solid echo acquisition of pure D_2O and D_2O with added AFP III at concentrations of 10, 15, 20 and 25 mg mL^{-1} and lysozyme at 20 mg mL^{-1}. The temperature was calibrated to -30 °C using lead nitrate external reference and maintaining a MAS frequency of 12.5 kHz using a Bruker 4 mm HXY probe.

a different T_1 compared to that of the wide quadrupolar lineshape. The former has a T_1 in the order of tens of milliseconds while the latter has a T_1 in the order of seconds. This narrow resonance and the broad quadrupolar ice lineshape can be seen in figure 5.1b. The narrow width of this resonance implies that the D_2O molecules giving rise to the resonance as well as its chemical shift is consistent with liquid water. This liquid water is thought to be in the hydration shell of the protein [126] as water otherwise present as supernatant has been shown to be completely frozen at -20 °C [134]. This is consistent with the ^1H spectra in figure 5.3 where there are no ^1H resonances present which can be assigned to the supernatant below -10 °C. The narrow resonance is present in the deuterium spectra at all weight percentages of AFP III. However, the proportion of the total magnetisation which is located in this narrow resonance increases from 7% at 10 mg mL^{-1} to 87% at 25 mg mL^{-1}. This is as expected as an increase in the proportion of the AFP III would lead to an increase in the proportion of D_2O present as liquid in the hydration shell. The increase in the weight percentage of AFP III appears to be linearly correlated to the proportion of magnetisation

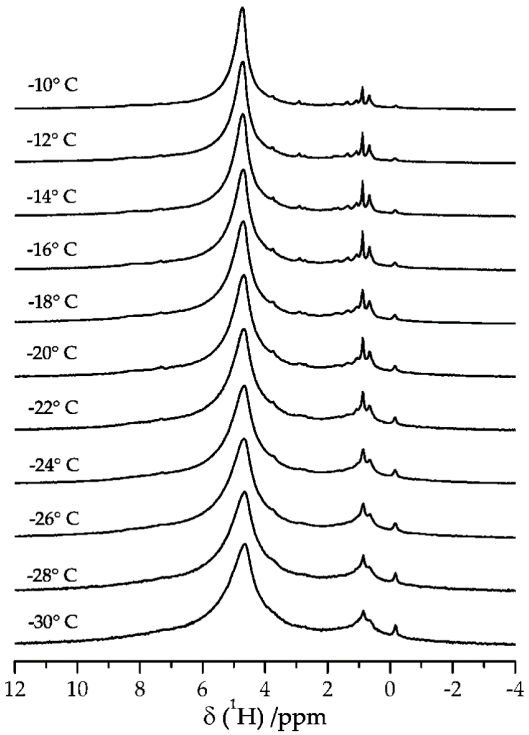

Figure 5.3: ^{1}H Hahn echo spectra of AFP III in H_2O recorded between -10 °C and -30 °C.

in the narrow resonance which is consistent with the increase being due to the AFP III weight percentage.

Figure 5.2 shows saturation recovery curve of lysozyme, which is a non ice active protein showed an increase of the deuterium T_1 to 100 s from 36 s in pure D_2O as well as well as 37 of the total magnetisation being present in the narrow central resonance with a T_1 of 8 ms. The increase in T_1 cannot be due to the transfer of the proton T_1 of the protein via the dipolar coupling as the proton T_1 is faster than the deuterium T_1. The presence of the narrow resonance previously assigned to the hydration shell is consistent with observations on AFP III. The overall behaviour of lysozyme is therefore consistent with a non ice active protein.

Table 5.1: The Deuterium T_1 recovery times of D_2O with antifreeze additives.

Sample	Central Resonance T_1 /ms	Quadruplar Resonance T_1 /s
D_2O	-	(36±2)
carrageenan	-	(32.5±0.8)
λ-carrageenan	-	(39±4)
ι-carrageenan	(6±1)	(11±1)
Deltagel	(4±1)	(35±2)
ISP (10 mg mL^{-1})	(6±2)	(2.9±0.2)
ISP (15 mg mL^{-1})	(7.5±0.6)	(2±0.1)
ISP (20 mg mL^{-1})	(7±1)	(1.9±0.5)
ISP (25 mg mL^{-1})	(10±3)	(0.6±0.1)
Lysozyme	(8±2)	$(1.0\pm0.1)\times10^2$

5.2.2 Proton EXSY of Antifreeze Proteins

In figures 5.4a and 5.4b is shown the ^{1}H-^{1}H EXSY 2D spectra with a 100 ms mixing time of 20 mg mL^{-1} AFP III added to H_2O at -10 °C and -20 °C. The intense and broad resonance at 4.8 ppm is assigned to H_2O as ice. The less intense proton resonances between 0 and 4 ppm are all assigned as aliphatic protons on AFP III. Both EXSY spectra show clear cross peaks between the ice resonance and the AFP III resonances. This is particularly evident at -20 °C. This is consistent with Howard el al [129] who found that non-polar (aliphatic) amino acids fill the holes in ice lattice and would therefore be in close proximity to ice. This is evidence of strong dipolar coupling between protons on AFP III and protons in the ice. Such dipolar coupling would not be possible if there were a complete hydration shell around AFP III and the presence of these cross peaks is therefore consistent with an ice-protein interface. The ice-AFP III cross peak becomes more intense going from -10 °C to -20 °C which is a result of the dipolar coupling becoming stronger. This is an effect of decreased motional averaging one cause of which could be that when the temperature decreases AFP III stays longer bound on the ice surface as it dynamically attaches and detaches itself from the surface which is consistent with the adsorption and growth inhibition mechanism proposed by Kristiansen *et al* [121].

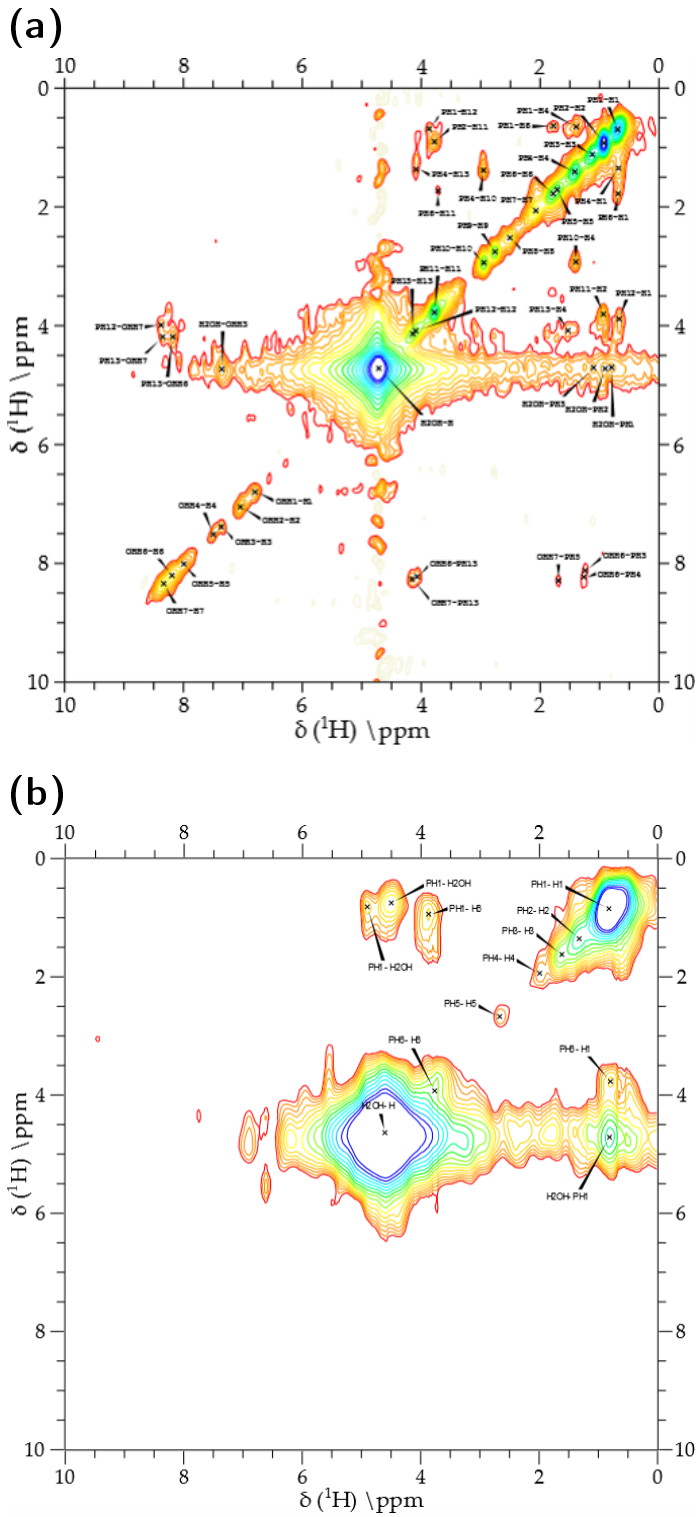

Figure 5.4: ^{1}H-^{1}H 2D EXSY spectra with 100 ms mixing time of H_2O with 20 mg mL^{-1} AFP III added at (a) -10 °C and (b) -20 °C. A spin echo was used to refocus before acquisition to reduce artifacts in the spectrum. The temperature was calibrated using lead nitrate while maintaining a MAS frequency of 12.5 kHz.

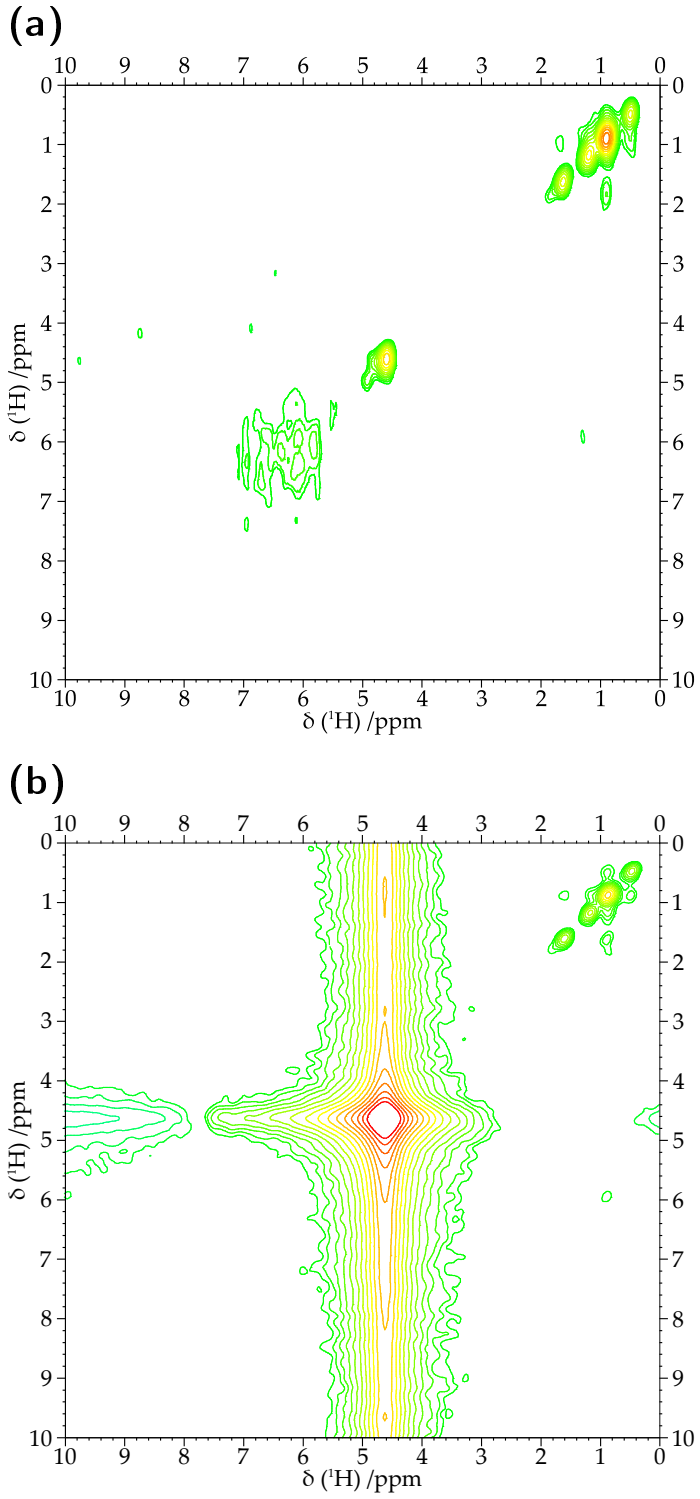

Figure 5.5: ^{1}H-^{1}H 2D EXSY spectra with 100 ms mixing time of (a) D2O with 20 mg mL^{-1} lysozyme added and (b) H_2O with 20 mg mL^{-1} lysozyme added. A spin echo was used to refocus before acquisition to reduce artifacts in the spectrum. The temperature was calibrated using lead nitrate to -20 °C while maintaining a MAS frequency of 12.5 kHz.

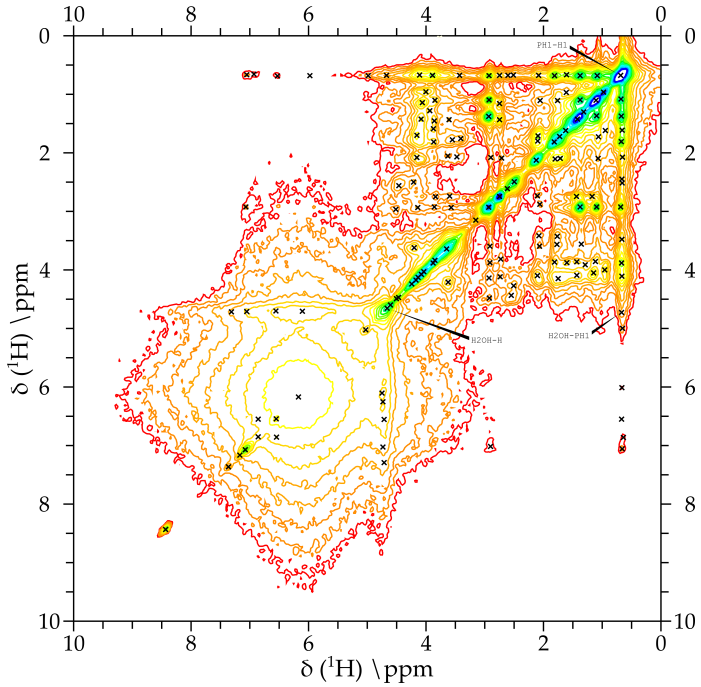

Figure 5.6: ^{1}H-^{1}H 2D EXSY spectra with 100 ms mixing time of D_2O with 20 mg mL^{-1} AFP III added. A spin echo was used to refocus before acquisition to reduce artifacts in the spectrum. The temperature was calibrated to -10 °C using lead nitrate while maintaining a MAS frequency of 12.5 kHz.

In figures 5.5a and 5.5b is shown the ^{1}H-^{1}H EXSY spectra with 100 ms mixing time of 20 mg mL^{-1} lysozyme added to D_2O and H_2O, respectively. The spectra were aquired at -20 °C. Two groups of resonances are present in the spectra. At 4.8 ppm is a broad resonance which is assigned to protons in the H_2O ice. The resonances between 0 and 3 ppm are assigned to aliphatic proton on lysozyme. The EXSY spectra of lysozyme added to H_2O suffers from an artifact called T_1 noise. However, it is still clear in both spectra that there is no indication of any cross peaks between the ice resonance and the lysozyme resonances. This shows that such cross peaks do no occur normally between proteins and ice but are a special feature only present in proteins with antifreeze activity.

In figure 5.6 is shown the ^{1}H-^{1}H EXSY with a mixing time of 100 ms of 20 mg mL^{-1} AFP III added to D_2O at -10 °C. This spectrum shows much improved resolution when compared with figure 5.4a where AFP III is mixed with H_2O. This is because the ice resonance in figure 5.4a is so intense that it obscures the

much smaller resonances which are very close by. This spectrum also contains possible ice-protein cross peaks which have been labelled on figure 5.6 but due to the dilution of ^{1}H in the ice cross peak has much lower intensity than in figure 5.4a.

In figure 5.3 is shown ^{1}H MAS spin echo spectra of AFP III in H_2O at variable temperatures. The spectra were recorded while going down in temperature from -10 °C to -30 °C. The most prominent features of these spectra are firstly the broadening of all the peaks including the very intense H_2O resonance at 4.8 ppm. This means that as the temperature is reduced the formation of ice continues as the ice lattice becomes more rigid. Secondly, the protein AFP III resonances between 0 and 2 ppm as well as becoming broader are shifting upfield. Thirdly, a resonance at 0 ppm becomes increasingly prominent as the temperature is reduced. Lastly, the very weak AFP III resonances between 2 to 4 ppm at -10 °C become absorbed into the baseline as the temperature decreases.

5.3 Carrageenan

5.3.1 Deuterium Spin Lattice of D_2O with Carrageenan

Figure 5.7 shows the effect on the T_1 saturation recovery of deuterium of adding ι-carrageenan, λ-carrageenan and two mixed carrageenans one labelled deltagel and the other just carrageenan to D_2O at a concentration of 20 mg mL^{-1}. The 1D spectra of D_2O with added carrageenans have the same features as with added AFP III, a broad quadrupolar lineshape and a narrow central resonance. These resonances have different T_1 relaxation times, the narrow on the order of milliseconds and the broad on the order of seconds.

Of the four carrageenans only ι-carrageenan exhibits a reduction in T_1 to 11 s from 36 s in pure D_2O. The T_1 of of D_2O with carrageenan is significantly higher than D_2O with added AFP which is 2 s. This reduction in T_1 is consistent with an interface between the ι-carrageenan and ice where cross-relaxation can be transferred via a strong dipolar coupling. There are two possibilities

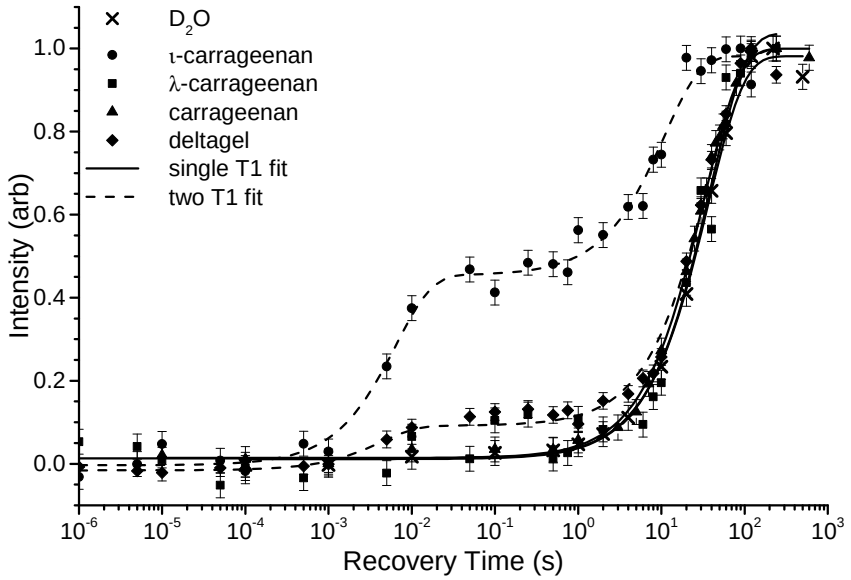

Figure 5.7: Deuterium saturation recovery T_1 with solid echo acquisition of pure D_2O as well **??** as D_2O with deltagel, ι-carrageenan, λ-carrageenan and mixed carrageenan added at 20 mg mL^{-1} . The temperature was calibrated to -30 °C using lead nitrate while maintaining a MAS frequency of 12.5 kHz.

explaining the higher T_1 value of D_2O with added ι-carrageenan compared to D_2O with APF III. It could be due the intrinsic T_1 of protons being different in ι-carrageenan than AFP III. Alternatively, it can be explained by weaker interaction between carrageenan and ice at the interface compared to AFP III. The spectra also exhibits a narrow resonance at 0 ppm with a T_1 of 6 ms which is equivalent to that observed in all spectra of AFP III and is consistent with there being a hydration shell around the ι-carrageenan.

The 1D ^2H MAS NMR spectra of λ-carrageenan and mixed carrageenan exhibit a spectra similar to that of pure D_2O in figure 5.1a with only a single broad resonance with a quadrupolar lineshape but no narrow central resonance. Additionally, the ^2H saturation recovery T_1 shown in figure 5.7 of these broad resonances are 32.5 s and 39 s which is very similar to the T_1 of pure D_2O which is 36 s. The lack of a narrow central resonance suggests that the samples contain no liquid water neither as hydration sphere or as a supernatant. This is very different to all other additives used in this work which all result in the D_2O which is unfrozen as is expected in a hydration shell around the additive. The

lack of this resonance therefore suggests that these additives are frozen into the bulk of the D_2O. This might explain why the T_1 of D_2O with these compounds added does not change from pure D_2O. The faster proton T_1 is caused by protons moving relative to one another causing fluctuations in the local magnetic field and thus relaxing as explained in section 2.7. As these carrageenans appear to be frozen into D_2O such movements are impossible and thus the T_1 of protons is longer than expected and cannot reduce the T_1 of the frozen D_2O through cross relaxation over an interface even if it exists.

The 1D ^2H MAS NMR spectrum of deltagel, another mixed carrageenan, exhibits two resonances similar to those of AFP III and ι-carrageenan. One is a broad resonance with quadrupolar lineshape and the other a narrow resonance both centred at 0 ppm. As with AFP III these resonances are assigned to frozen D_2O and liquid D_2O in a hydration shell, respectively. From the saturation recovery spectrum shown in figure 5.7 the T_1 of the broad and narrow resonances are measured to be 35 s and 2 ms, respectively. The T_1 of this broad resonance is very similar to that measured of pure D_2O. This is different from ι-carrageenan (and by extension AFP III) whose broad resonance has a much faster T_1. It also different from mixed carrageenan and λ-carrageenan which have the same broad quadrupolar resonance but no narrow resonance while their T_1 is similar to pure D_2O like deltagel.

There are two possible explanations for these observations. The first is that deltagel is acting like mixed carrageenan and λ-carrageenan as explained in the previous paragraph. While the D_2O in the deltagel sample is not completely frozen like in the λ- and mixed carrageenan there is too little liquid D_2O for the protons in deltagel to move sufficiently and thus reduce the deuterium T_1 through cross relaxation. The second explanation is unsatisfactorily that there is no interface to ice and thus no possibility of cross relaxation. The implication of this second explanation is that the thermal hysteresis of D_2O when deltagel is added must occur through another mechanism which does not involve a interface between the deltagel and the ice. Further experiments are required to differentiate between these two cases.

5.4 Conclusion and Further Work

The reduction in T_1 seen when AFP III is added to D_2O suggests there is an protein ice interface in agreement with previous studies [126]. The dependence of the T_1 on the concentration of AFP III added is consistent with the adsorption and growth inhibition mechanism suggested as the cause of the observed hysteresis gap [121]. This is extended to carrageenan with ι-carrageenan exhibiting the same ^2H saturation recovery T_1 behaviour as AFP III when added to D_2O. This strongly suggests that the same adsorption and growth inhibition mechanism at a carrageenan ice interface is responsible for the hysteresis gap exhibited by ι-carrageenan. However, λ-carrageenan, mixed carrageenan and deltagel which also exhibit the hysteresis gap of ι-carrageenan show a different ^2H saturation recovery T_1 when added to D_2O. Specifically, the T_1 is not reduced from that of pure D_2O and these samples also appear frozen like pure D_2O. It is hypothesised that the cause of this is that carrageenan is frozen into the ice which prevents the necessary proton motion which in the ultimate cause of the reduced D_2O T_1 through dipolar cross relaxation.

The ^1H-^1H EXSY spectra of AFP III added to H_2O show clear cross peaks between ice resonances and aliphatic proton resonances from AFP III. This is in contrast to the EXSY spectra where AFP III is replaced by lysozyme which shows no such cross peaks. This strongly suggests that the cross peaks observed are specific to AFP III and caused by a protein-ice interface not present with lysozyme.

Further investigations should start with ι-carrageenan as its performance in D_2O most closely resembles that of AFP III. Further confirmation of a carrageenan ice interface should involve measuring the D_2O ^2H saturation recovery T_1 while varying the carrageenan concentration dissolved in D_2O. Additionally, acquiring ^1H-^1H EXSY spectra of carrageenan added to H_2O and directly observing cross peaks between carrageenan and ice resonances.

Appendices

Appendix A

Irreducible Spherical Tensors

The Hamiltonian of any interaction can be written in the form

$$\hat{\mathscr{H}}_{\Lambda} = \hat{\mathbf{I}} \cdot \tilde{\mathbf{\Lambda}} \cdot \hat{\mathbf{S}}, \tag{A.1}$$

which can be rewritten using irreducible spherical tensors in the form

$$\hat{\mathscr{H}}_{\Lambda} = \sum_{j=0}^{2} \sum_{m=-j}^{+j} (-1)^m A_{j,m} \hat{T}_{j,-m}. \tag{A.2}$$

The component of the spacial spherical tensor $A_{j,m}$ are derived many places and have the form

$$\begin{aligned}
A_{0,0} &= \frac{1}{3}(A_{xx} + A_{yy} + A_{zz}) = \frac{1}{3} Tr\{\tilde{\mathbf{A}}\} \\
A_{1,0} &= -\frac{i}{\sqrt{2}}(A_{xy} - A_{yx}) \\
A_{1,\pm 1} &= -\frac{1}{2}\left[A_{zx} - A_{xz} \pm i(A_{zy} - A_{yz})\right] \\
A_{2,0} &= \frac{1}{\sqrt{6}}\left[3A_{zz} - (A_{xx} + A_{yy} + A_{zz})\right] \\
A_{2,\pm 1} &= \mp\frac{1}{2}\left[A_{zx} + A_{xz} \pm i(A_{zy} + A_{yz})\right] \\
A_{2,\pm 2} &= \frac{1}{2}\left[A_{xx} - A_{yy} \pm i(A_{xy} + A_{yx})\right].
\end{aligned} \tag{A.3}$$

For the dipolar coupling tensor in the principal axis frame all non-diagonal elements are zero. Additionally, the trace of the interaction tensor is zero $A_{xx} + A_{yy} + A_{zz} = 0$ and the interaction is axially symmetric $A_{xx} = A_{yy} \neq A_{zz}$. This means that only a single component of the spacial spherical tensor is non-zero

$$A^{IS}_{2,0} = \sqrt{\frac{1}{6}}\big[3A_{zz} - (A_{xx} + A_{yy} + A_{zz})\big] = \frac{3}{\sqrt{6}}A_{zz} \tag{A.4}$$

For the quadrupolar coupling tensor the in the principal axis frame all non-diagonoal elements are zero and the trace also zero but it is not axially symmetric. This leaves two non-zero elements in the spacial spherical tensor

$$\begin{aligned} A^{Q}_{2,0} &= \sqrt{\frac{1}{6}}\big[3A_{zz} - (A_{xx} + A_{yy} + A_{zz})\big] = \frac{3}{\sqrt{6}}A_{zz} \\ A^{Q}_{2,\pm 2} &= \frac{1}{2}\big[A_{xx} - A_{yy} \pm i(A_{xy} + A_{yx})\big] = \frac{1}{2}(A_{xx} - A_{yy}) \end{aligned} \tag{A.5}$$

The elements of the corresponding spin spherical tensor $\hat{T}_{j,-m}$ have the general form

$$\begin{aligned} \hat{T}_{0,0} &= \frac{1}{\sqrt{3}}(\hat{I}_x\hat{S}_x + \hat{I}_y\hat{S}_y + \hat{I}_z\hat{S}_z) \\ \hat{T}_{1,0} &= \frac{1}{\sqrt{2}}i(\hat{I}_x\hat{S}_y - \hat{I}_y\hat{S}_x) \\ \hat{T}_{1,\pm 1} &= \mp\frac{1}{2}i\big[\hat{I}_y\hat{S}_z - \hat{I}_z\hat{S}_y \pm i(\hat{I}_z\hat{S}_x - \hat{I}_x\hat{S}_z)\big] \\ \hat{T}_{2,0} &= \frac{1}{\sqrt{6}}(2\hat{I}_z\hat{S}_z - \hat{I}_x\hat{S}_x - \hat{I}_y\hat{S}_y) \\ \hat{T}_{2,\pm 1} &= \mp\frac{1}{2}\big[\hat{I}_x\hat{S}_z + \hat{I}_z\hat{S}_x \pm i(\hat{I}_y\hat{S}_z + \hat{I}_z\hat{S}_y)\big] \\ \hat{T}_{2,\pm 2} &= \frac{1}{2}\big[\hat{I}_x\hat{S}_x + \hat{I}_y\hat{S}_y \pm i(\hat{I}_x\hat{S}_y + \hat{I}_y\hat{S}_x)\big]. \end{aligned} \tag{A.6}$$

In the case of the heteronucelear dipolar coupling where $\hat{\mathbf{I}}$ and $\hat{\mathbf{S}}$ are different this is reduced to

$$\begin{aligned}
\hat{T}^{IS}_{00} &= -\frac{2}{\sqrt{3}}\left[\hat{I}_z\hat{S}_z + \frac{1}{2}(\hat{I}_+\hat{S}_- + \hat{I}_-\hat{S}_+)\right] \\
\hat{T}^{IS}_{10} &= \frac{1}{\sqrt{2}}(\hat{I}_-\hat{S}_+ - \hat{I}_+\hat{S}_-) \\
\hat{T}^{IS}_{1\pm1} &= (-\hat{I}_\pm\hat{S}_z + \hat{I}_z\hat{S}_\pm) \\
\hat{T}^{IS}_{2\pm0} &= \frac{1}{\sqrt{6}}(3\hat{I}_z\hat{S}_z - \hat{\mathbf{I}}\cdot\hat{\mathbf{S}}) \\
\hat{T}^{IS}_{2\pm1} &= \mp\frac{1}{2}(\hat{I}_\pm\hat{S}_z + \hat{I}_z\hat{S}_\pm) \\
\hat{T}^{IS}_{2\pm2} &= \frac{1}{2}\hat{I}_\pm\hat{S}_\pm. \qquad \text{(A.7)}
\end{aligned}$$

In the case of the quadrupolar coupling where $\hat{\mathbf{S}} = \hat{\mathbf{I}}$ are different this is reduced to

$$\begin{aligned}
\hat{T}^{Q}_{00} &= -\frac{1}{\sqrt{2}} \\
\hat{T}^{Q}_{10} &= \sqrt{2}\hat{I}_z \\
\hat{T}^{Q}_{1\pm1} &= \mp\frac{1}{\sqrt{2}}(\hat{I}_z \pm i\hat{I}_y \\
\hat{T}^{Q}_{2\pm0} &= \frac{1}{\sqrt{6}}(3\hat{I}^2_z - \hat{\mathbf{I}}\cdot\hat{\mathbf{I}}) \\
\hat{T}^{Q}_{2\pm1} &= \mp(\hat{I}_\pm\hat{I}_z + \hat{I}_z\hat{I}_\pm) \\
\hat{T}^{Q}_{2\pm2} &= \frac{1}{2}\hat{I}^2_\pm. \qquad \text{(A.8)}
\end{aligned}$$

Appendix B

Spin-Lattice Saturation Recovery Curves of Titanium Oxide

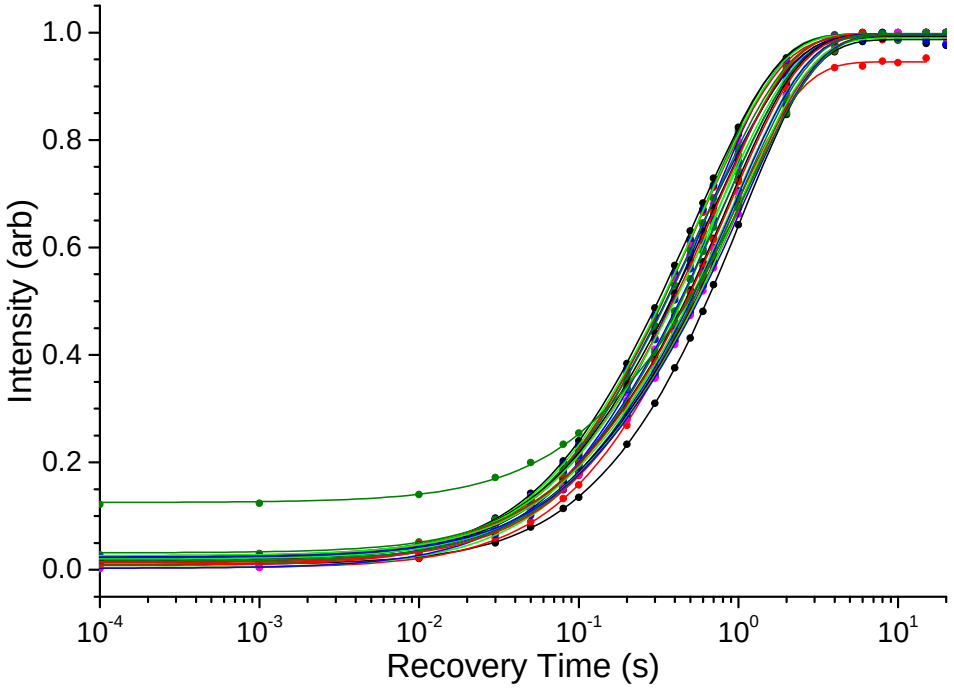

Figure B.1: The spin-lattice T_1 saturation recovery curves of pure NSF and TiO_2 NSF DEE.

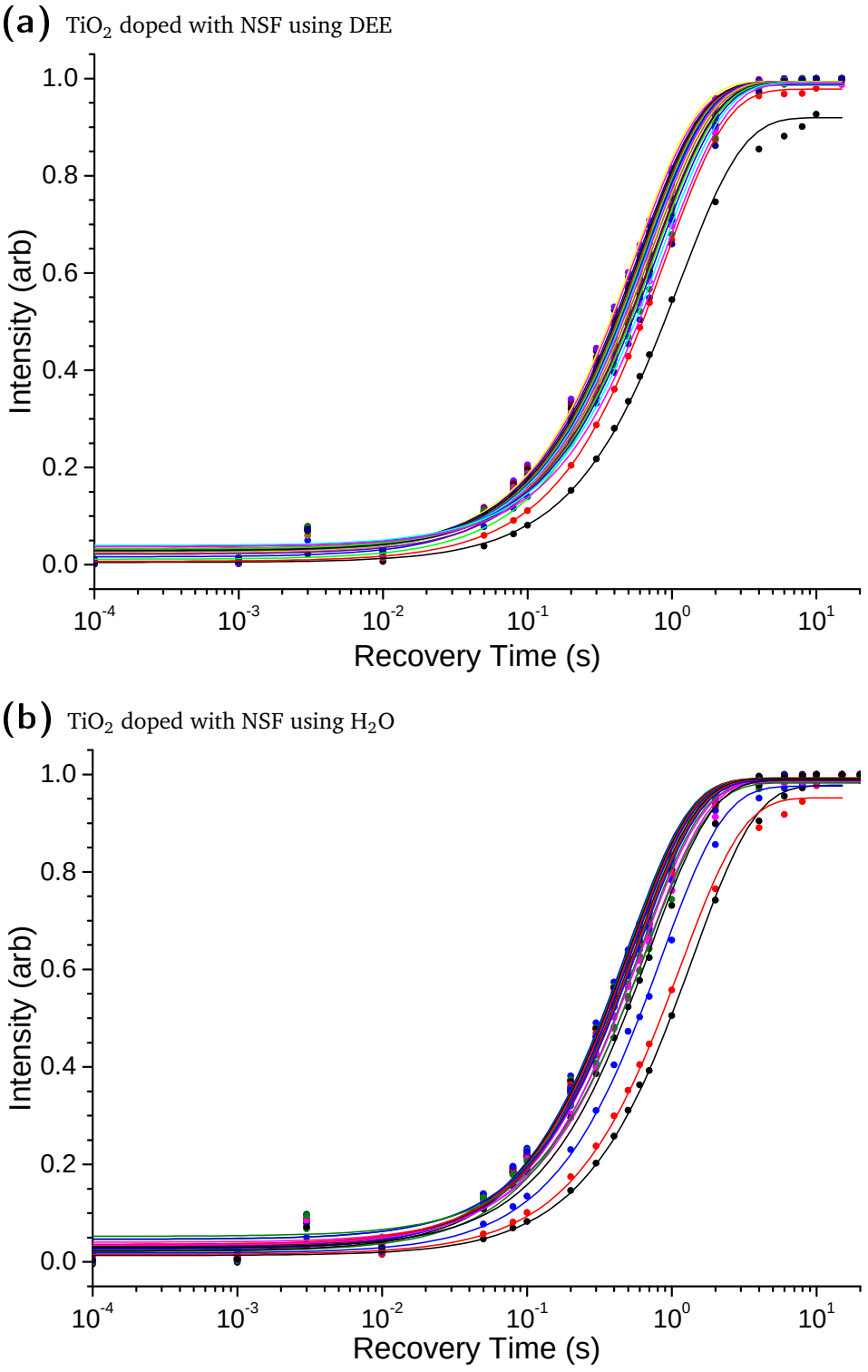

Figure B.2: The spin-lattice T_1 saturation recovery curves of pure NSF and TiO_2 NSF DEE.

Appendix C

Spin-Lattice Saturation Recovery Curves of Tantalum and Niobium Oxide

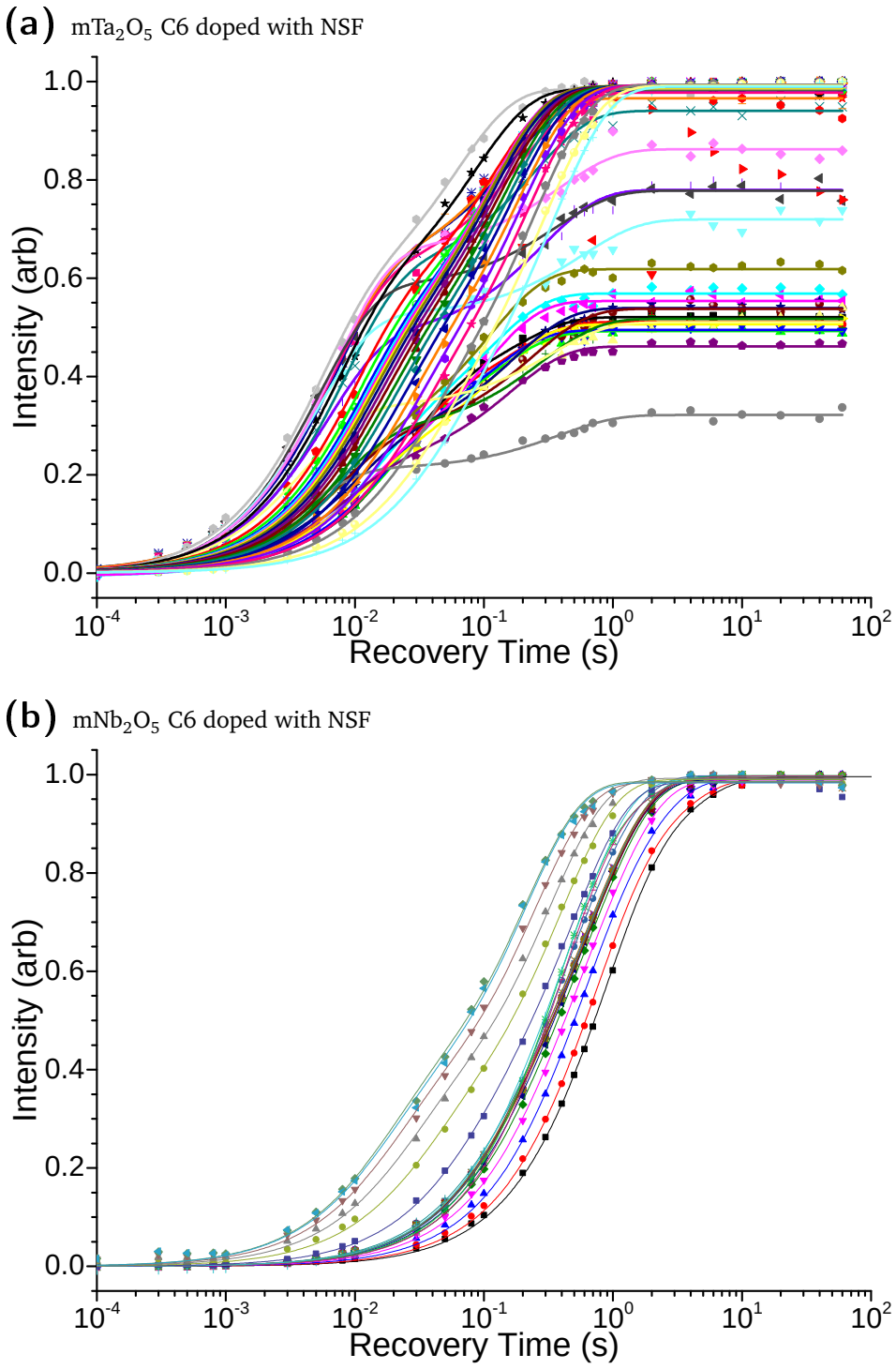

Figure C.1: The spin-lattice T_1 saturation recovery curves of mTa_2O_5 and mNb_2O_5 C6.

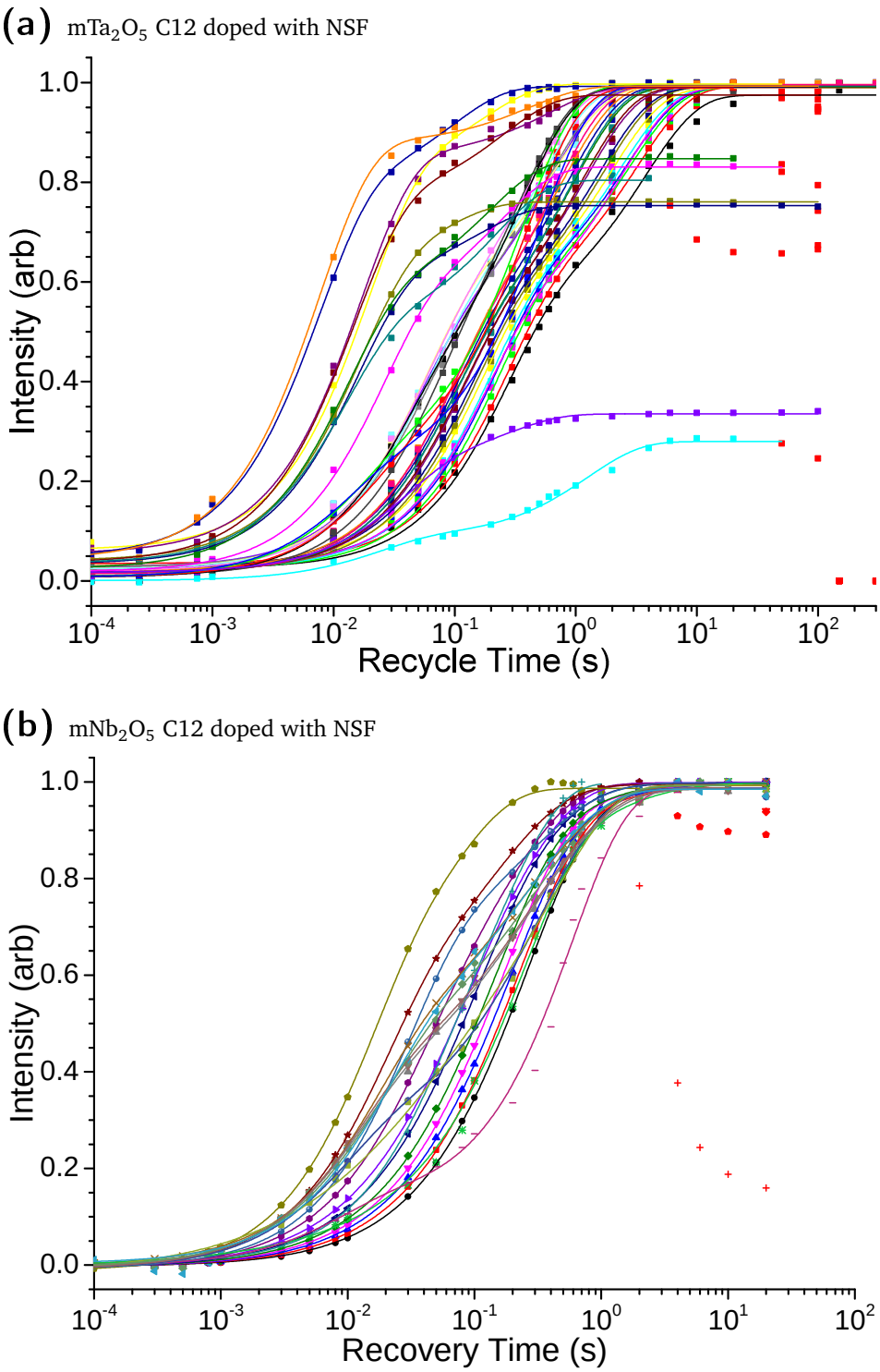

Figure C.2: The spin-lattice T_1 saturation recovery curves of mTa_2O_5 and mNb_2O_5 C12.

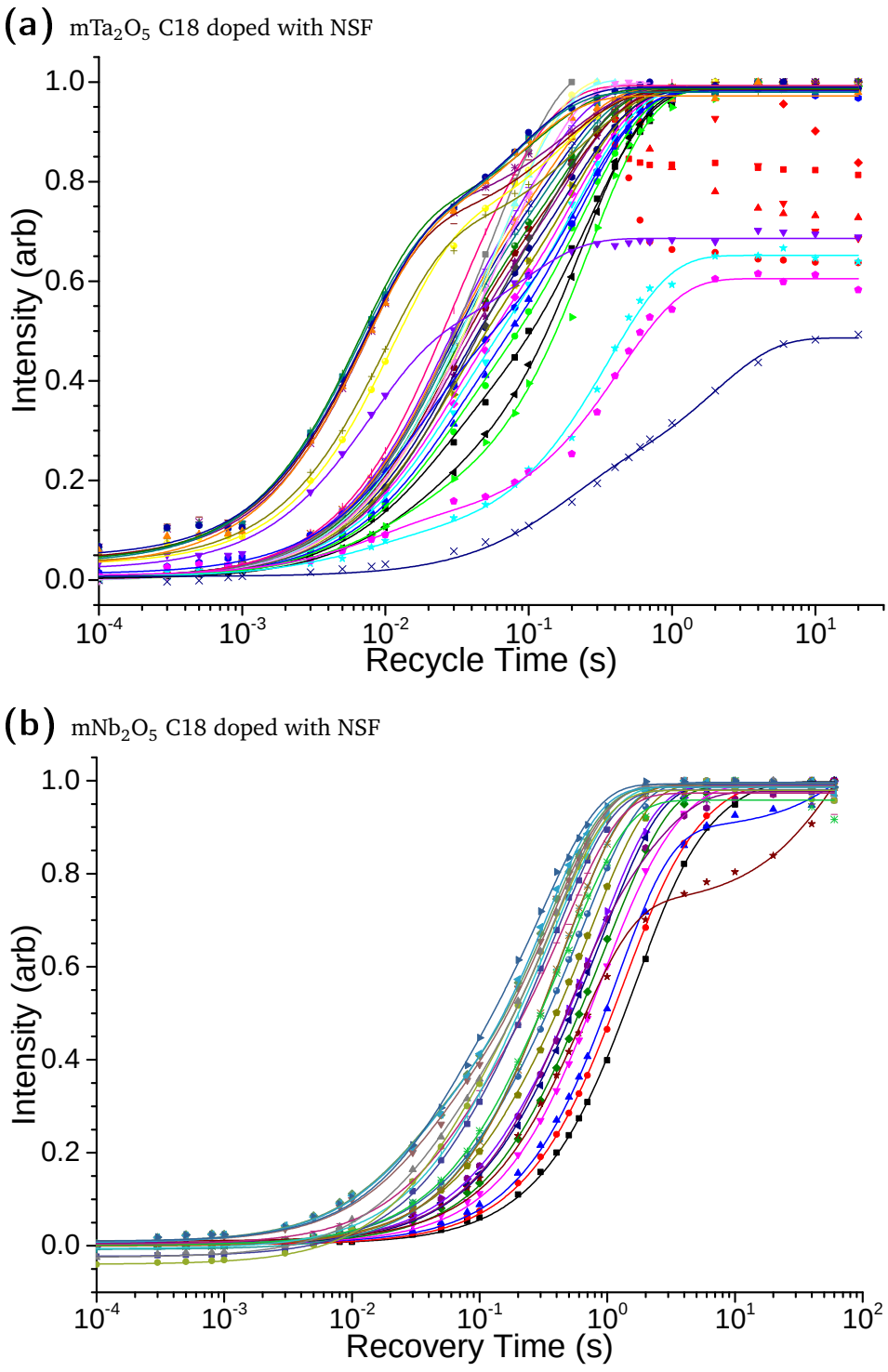

Figure C.3: The spin-lattice T_1 saturation recovery curves of mTa_2O_5 and mNb_2O_5 C18.

Appendix D

PFG MAS diffusion curves of Titanium Oxide doped NSF

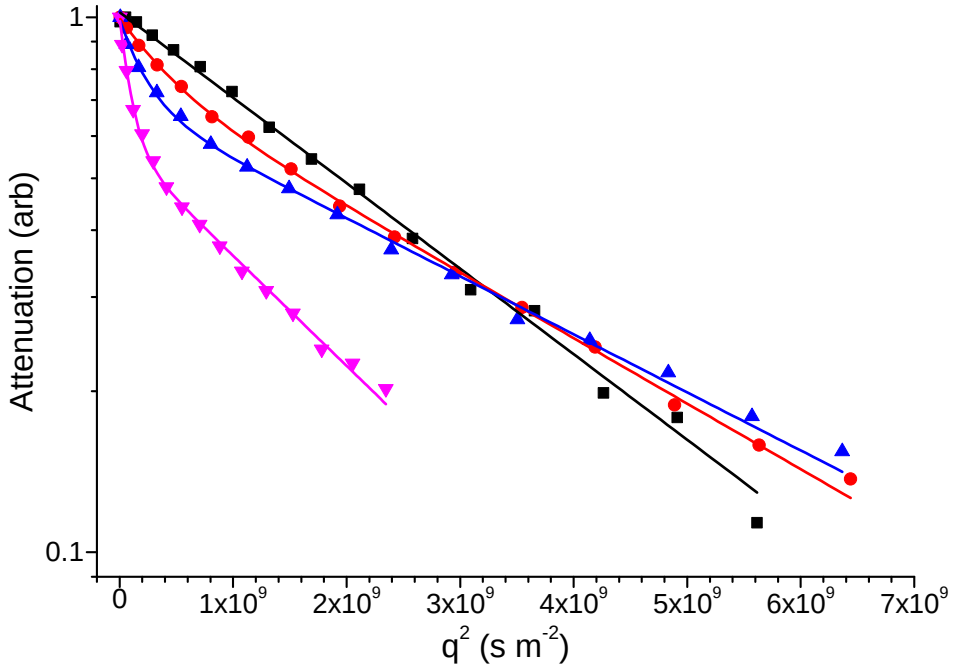

Figure D.1: The STE-PFG MAS decay curves of $mTiO_2$-NSF-DEE. Black squares have $\Delta = 14$ ms, red circles $\Delta = 20$ ms, blue triangles $\Delta = 50$ ms, purple triangle $\Delta = 100$ ms, green diamond $\Delta = 200$ ms and navy blue triangle $\Delta = 400$ ms

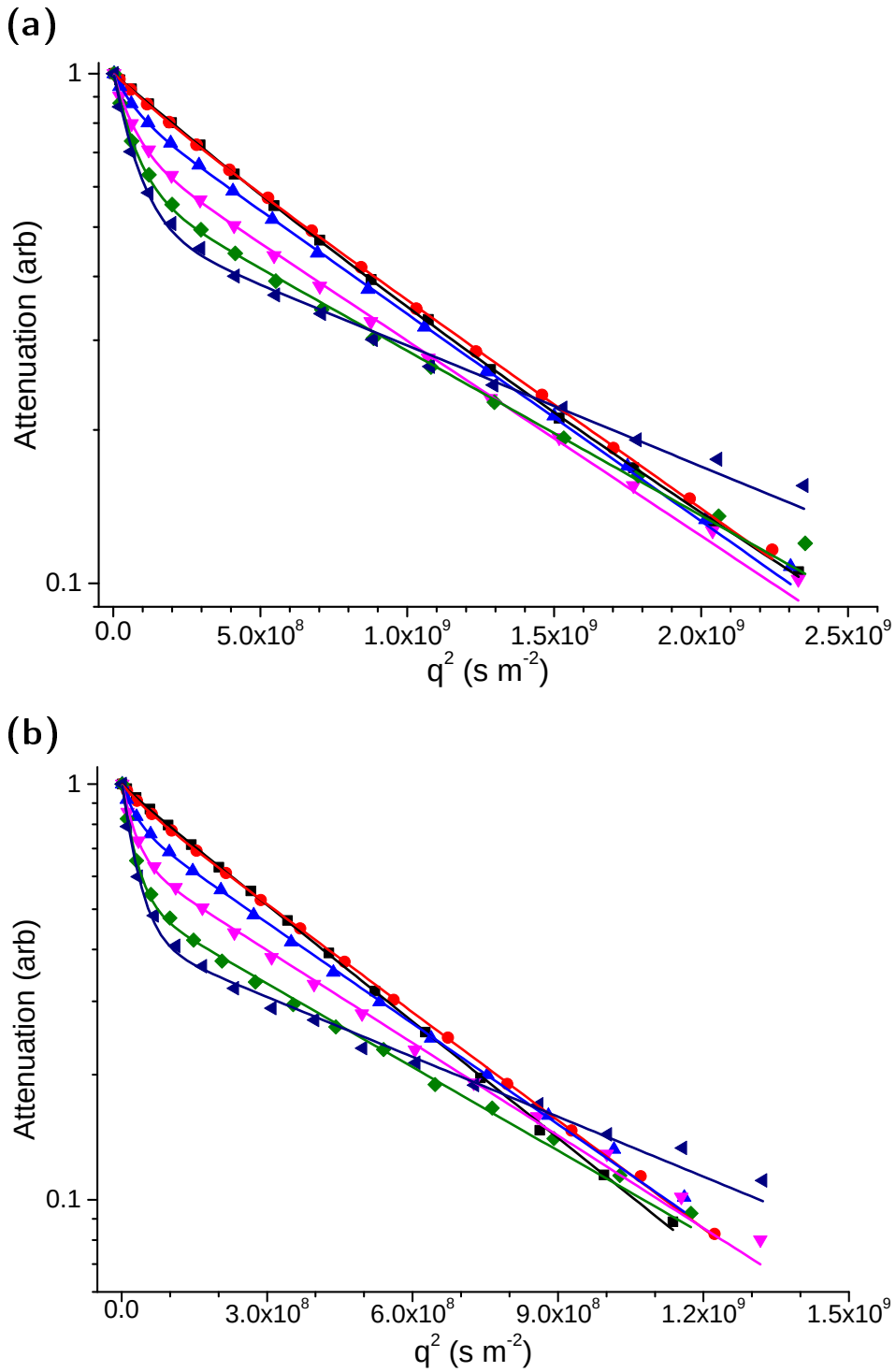

Figure D.2: The STE-PFG MAS decay curves of $mTiO_2$-NSF-DEE. Black squares have $\Delta = 14$ ms, red circles $\Delta = 20$ ms, blue triangles $\Delta = 50$ ms, purple triangle $\Delta = 100$ ms, green diamond $\Delta = 200$ ms and navy blue triangle $\Delta = 400$ ms

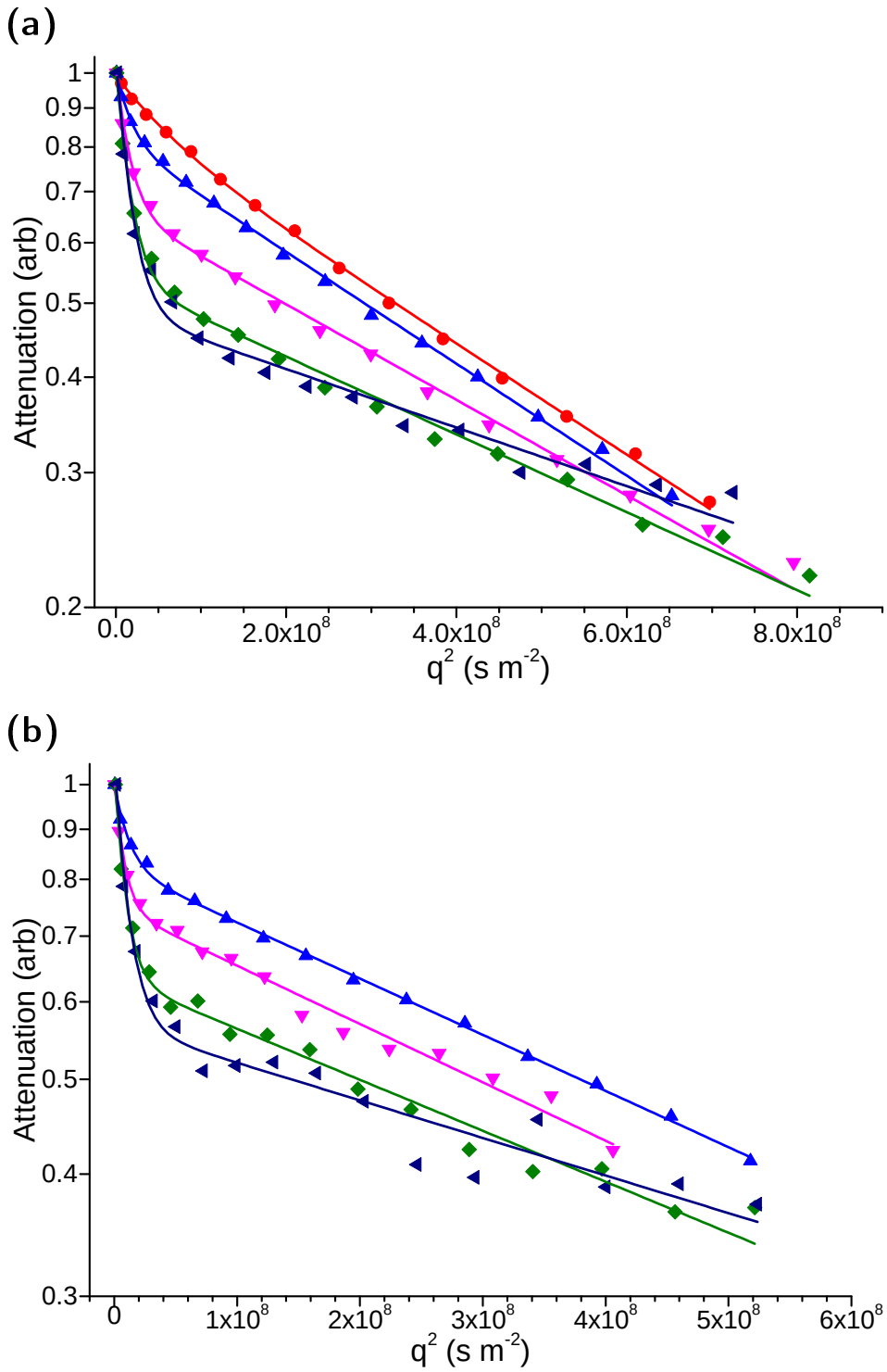

Figure D.3: The STE-PFG MAS decay curves of $mTiO_2$-NSF-DEE. Black squares have $\Delta = 14$ ms, red circles $\Delta = 20$ ms, blue triangles $\Delta = 50$ ms, purple triangle $\Delta = 100$ ms, green diamond $\Delta = 200$ ms and navy blue triangle $\Delta = 400$ ms

Bibliography

[1] L. Carrette, K. a. Friedrich, U. Stimming, *Chemphyschem* **1**, 162 (2000).

[2] T. Zhao, K. D. Kreuer, T. V. Nguyen, *Advances in fuel cells* (2007).

[3] H. Zhang, P. K. Shen, *Chem. Rev.* **112**, 2780 (2012).

[4] W. Grove, *Philos. Mag. Ser. 3* **14**, 127 (1839).

[5] W. R. Grove, *Philos. Mag. J. Sci.* **XXI**, 417 (1842).

[6] L. Mond, C. Langer, *Proc. R. Soc.* **46**, 296 (1889).

[7] W. Ostwald, *Zeitschrift für Elektrotechnik und Elektrochemie* **1**, 122 (1894).

[8] F. T. Bacon, T. M. Fry, *Proc. R. Soc. A Math. Phys. Eng. Sci.* **334**, 427 (1973).

[9] M. Warshay, P. R. Prokopiusm, The Fuel Cell in Space: Yesterday, Today and Tomorrow (1989).

[10] J. M. Andújar, F. Segura, *Renew. Sustain. Energy Rev.* **13**, 2309 (2009).

[11] J. M. Grimwood, B. C. Hacker, P. J. Vorzimmer, Project Gemini Technology and Operations A Chronology (1969).

[12] S. Paddison, *Annu. Rev. Mater. Res.* **33**, 289 (2003).

[13] A.-C. Dupuis, *Prog. Mater. Sci.* **56**, 289 (2011).

[14] K. D. Kreuer, S. J. Paddison, E. Spohr, M. Schuster, *Chem. Rev.* **104**, 4637 (2004).

[15] A. S. Aricò, S. Srinivasan, V. Antonucci, *Fuel Cells* **1**, 133 (2001).

[16] S. Bose, *et al.*, *Prog. Polym. Sci.* **36**, 813 (2011).

[17] R. Devanathan, *Energy Environ. Sci.* **1**, 101 (2008).

[18] M. Schuster, *et al.*, *Solid State Ionics* **145**, 85 (2001).

[19] J. C. Persson, P. Jannasch, *Chem. Mater.* **15**, 3044 (2003).

[20] Z. Zhou, S. Li, Y. Zhang, M. Liu, W. Li, *J. Am. Chem. Soc.* **127**, 10824 (2005).

[21] S. Li, Z. Zhou, Y. Zhang, M. Liu, W. Li, *Chem. Mater.* **17**, 5884 (2005).

[22] A. L. Blumenfeld, *et al.*, *Solid State Ionics* **68**, 105 (1994).

[23] M. F. Schuster, W. H. Meyer, *Ann. Rev. Mater. Res.* **33**, 233 (2003).

[24] J. P. Turley, *et al.*, *Microporous Mesoporous Mater.* **190**, 284 (2014).

[25] J. P. Turley, *et al.*, *ChemSusChem* **8**, 301 (2015).

[26] K. D. Kreuer, *Solid State Ionics* **136-137**, 149 (2000).

[27] N. Agmon, *Chem. Phys. Lett.* **244**, 456 (1995).

[28] M. Tuckerman, K. Laasonen, M. Sprik, M. Parrinello, *J. Chem. Phys.* **103**, 150 (1995).

[29] D. Marx, M. E. Tuckerman, J. Hutter, M. Parrinello, *Nature* **397**, 601 (1998).

[30] K. D. Kreuer, *Chem. Mater.* **26**, 361 (2014).

[31] K. D. Kreuer, S. J. Paddison, E. Spohr, M. Schuster, *Chem. Rev.* **104**, 4637 (2004).

[32] S. P. Brown, I. Schnell, J. Diedrich Brand, K. Müllen, H. Wolfgang Spiess, *Phys. Chem. Chem. Phys.* **2**, 1735 (2000).

[33] S. P. Brown, H. W. Spiess, *Chem. Rev.* **101**, 4125 (2001).

[34] U. Akbey, S. Granados-Focil, E. B. Coughlin, R. Graf, H. W. Spiess, *J. Phys. Chem. B* **113**, 9151 (2009).

[35] J. W. Traer, G. R. Goward, *Phys. Chem. Chem. Phys.* **12**, 263 (2010).

[36] G. Kim, F. Blanc, Y.-Y. Hu, C. P. Grey, *J. Phys. Chem. C* **117**, 6504 (2013).

[37] M. Fechtelkord, a. Engelhardt, J. C. Buhl, L. Schwalowsky, U. Bismayer, *Solid State Nucl. Magn. Reson.* **17**, 76 (2000).

[38] G. R. Goward, M. F. H. Schuster, D. Sebastiani, I. Schnell, H. W. Spiess, *J. Phys. Chem. B* **106**, 9322 (2002).

[39] C. E. Hughes, *et al.*, *J. Phys. Chem. B* **108**, 13626 (2004).

[40] Y. J. Lee, *et al.*, *J. Phys. Chem. B* **111**, 9711 (2007).

[41] J. H. Kristensen, H. Bildsøe, H. J. Jakobsen, N. C. Nielsen, *J. Magn. Reson.* **100**, 437 (1992).

[42] J. H. Kristensen, G. L. Hoatson, R. L. Vold, *Solid State Nucl. Magn. Reson.* **13**, 1 (1998).

[43] Y. J. Lee, T. Murakhtina, D. Sebastiani, H. W. Spiess, *J. Am. Chem. Soc.* **129**, 12406 (2007).

[44] H. Arribart, Y. Piffard, *Solid State Commun.* **45**, 571 (1983).

[45] a. Ishikawa, *et al.*, *Solid State Ionics* **179**, 2345 (2008).

[46] K. Hayamizu, *et al.*, *J. Phys. Chem. B* **112**, 1189 (2008).

[47] R. Mattos, *et al.*, *Electrochim. Acta* **55**, 1396 (2010).

[48] A. Pawlicka, *et al.*, *J. Membr. Sci.* **429**, 190 (2013).

[49] K. L. Ngai, *Phys. Rev. B* **48**, 13481 (1993).

[50] Z. B. Yan, N. E. De Almeida, J. W. Traer, G. R. Goward, *Phys. Chem. Chem. Phys.* **15**, 17983 (2013).

[51] E. O. Stejskal, J. E. Tanner, *J. Chem. Phys.* **42**, 288 (1965).

[52] G. Ye, N. Janzen, G. R. Goward, *Macromol.* **39**, 3283 (2006).

[53] G. Ye, C. A. Hayden, G. R. Goward, *Macromolecules* **40**, 1529 (2007).

[54] T. Dippel, K. D. Kreuer, J. Lassegues, D. Rodriguez, *Solid State Ionics* **61**, 41 (1993).

[55] M. Schuster, K. D. Kreuer, H. Steininger, J. Maier, *Solid State Ionics* **179**, 523 (2008).

[56] L. Vilčiauskas, C. C. de Araujo, K. D. Kreuer, *Solid State Ionics* **212**, 6 (2012).

[57] A. Noda, K. Hayamizu, M. Watanabe, *J. Phys. Chem. B* (2001).

[58] M. Sharifi, M. Wark, D. Freude, J. Haase, *Microporous Mesoporous Mater.* **156**, 80 (2012).

[59] A. Abragam, *The Principles of Nuclear Magnetism* (Oxford University Press, Oxford, 1983).

[60] M. J. Duer, *Introduction to Solid-State NMR Spectroscopy* (Wiley-Blackwell, 2004).

[61] P. T. Callaghan, *Translational Dynamics and Magnetic Resonance* (Oxford University Press, 2011).

[62] U. Haeberlen, *Advances in Magnetic Resonance* (Academic Press, New York, 1976).

[63] G. E. Pake, *J. Chem. Phys.* **16**, 327 (1948).

[64] R. K. Wangsness, F. Bloch, *Phys. Rev.* **89**, 728 (1953).

[65] N. Bloembergen, E. M. Purcell, R. V. Pound, *Phys. Rev.* **73**, 679 (1948).

[66] K. Funke, *Prog. Solid State Chem.* **22**, 111 (1993).

[67] D. C. Johnston, *Phys. Rev. B* **74**, 184430 (2006).

[68] J. R. Zimmerman, W. E. Brittin, *J. Phys. Chem.* **61**, 1328 (1957).

[69] H. Wennerström, *Mol. Phys.* **24**, 69 (1972).

[70] E. L. Hahn, *Phys. Rev.* **80**, 580 (1950).

[71] C. P. Slichter, *Principles of Magnetic Resonance* (Springer-Verlag, Berlin, 1990).

[72] M. Cohen, F. Reif (1957), pp. 321–438.

[73] D. Fenzke, D. Freude, T. Fröhlich, J. Haase, *Chem. Phys. Lett.* **111**, 171 (1984).

[74] P. P. Man, J. Klinowski, A. Trokiner, H. Zanni, P. Papon, *Chem. Phys. Lett.* **151**, 143 (1988).

[75] A. Fick, *Ann. der Phys. und Chemie* **170**, 59 (1855).

[76] A. Fick, *Philos. Mag.* **10**, 30 (1855).

[77] H. C. Torrey, *Phys. Rev.* **104**, 563 (1956).

[78] W. S. Price, *Concepts Magn. Reson.* **9**, 299 (1997).

[79] P. W. Kuchel, *et al.*, *Concepts Magn. Reson. Part A* **40A**, 205 (2012).

[80] J. E. Tanner, *J. Chem. Phys.* **52**, 2523 (1970).

[81] J. Kärger, M. Kočirik, A. Zikánová, *J. Colloid Interface Sci.* **84**, 240 (1981).

[82] J. Kärger, H. Pfeifer, W. Heink, *Adv. Magn. Reson.* (Academic Press, 1988), vol. 12, pp. 1–89.

[83] W. S. Price, a. V. Barzykin, K. Hayamizu, M. Tachiya, *Biophys. J.* **74**, 2259 (1998).

[84] C. Johnson, *Prog. Nucl. Magn. Reson. Spectrosc.* **34**, 203 (1999).

[85] M. Bauer, R. Valiullin, G. Radons, J. Kärger, *J. Chem. Phys.* **135** (2011).

[86] H. Lechert, *Catal. Rev.* **14**, 1 (1976).

[87] A. Pampel, F. Engelke, D. Gross, T. Oerther, K. Zick, *SpinREPORT* **157/158**, 26 (2006).

[88] T. Meyer, *et al.*, *Chem. Phys. Lipids* **184**, e1 (2014).

[89] K. Kreuer, *J. Memb. Sci.* **185**, 29 (2001).

[90] B. Smitha, S. Sridhar, A. Khan, *J. Memb. Sci.* **259**, 10 (2005).

[91] J. J. Baschuk, X. Li, *Int. J. Energy Res.* **25**, 695 (2001).

[92] S. M. Haile, D. a. Boysen, C. R. Chisholm, R. B. Merle, *Nature* **410**, 910 (2001).

[93] S. P. Brown, *Prog. Nucl. Magn. Reson. Spectrosc.* **50**, 199 (2007).

[94] R. Graf, *Solid State Nucl. Magn. Res.* **40**, 127 (2011).

[95] E. Andrew, W. Hinshaw, M. Hutchins, R. Sjöblom, P. Canepa, *Mol. Phys.* **32**, 795 (1976).

[96] E. Steiner, *et al.*, *Chem. Phys. Let.* **495**, 287 (2010).

[97] D. Antonelli, *Microporous Mesoporous Mater.* **33**, 209 (1999).

[98] E. P. Barrett, L. G. Joyner, P. P. Halenda, *J. Am. Chem. Soc.* **73**, 373 (1951).

[99] C. Wolf, *et al.*, *Anal. Chem.* **72**, 5466 (2000).

[100] K. Bergstrom, C. Strandberg, Agrochemical Compositions Containing Naphthalene Sulfonate Derivatives and Nitrogen-Containing Surfactants (2013).

[101] T. Mildner, H. Ernst, D. Freude, *Solid State Nucl. Magn. Reson.* **5**, 269 (1995).

[102] A. Bielecki, D. P. Burum, *J. Magn. Reson. Ser. A* **116**, 215 (1995).

[103] T. F. Kemp, G. Balakrishnan, K. J. Pike, M. E. Smith, R. Dupree, *J. Magn. Reson.* **204**, 169 (2010).

[104] G. Ye, B. Fortier-McGill, J. W. Traer, A. Czardybon, G. R. Goward, *Macromol. Chem. Phys.* **208**, 2076 (2007).

[105] D. Massiot, *et al.*, *Magn. Reson. Chem.* **40**, 70 (2002).

[106] M. Holz, S. R. Heil, A. Sacco, *Phys. Chem. Chem. Phys.* **2**, 4740 (2000).

[107] D. Massiot, *et al.*, *Magn. Reson. Chem.* **40**, 70 (2002).

[108] Y. Rao, T. F. Kemp, M. Trudeau, M. E. Smith, D. M. Antonelli, *J. Am. Chem. Soc.* **130**, 15726 (2008).

[109] X. Q. Kong, *et al.*, *J. Am. Chem. Soc.* **134**, 14609 (2012).

[110] A. Marker, A. B. Roy, *Biochim. Biophys. Acta* **742**, 446 (1983).

[111] G. R. Goward, K. Saalwächter, I. Fischbach, H. W. Spiess, *Solid State Nucl. Magn. Res.* **24**, 150 (2003).

[112] J. A. Ramsay, *Philos. Trans. R. Soc. B Biol. Sci.* **248**, 279 (1964).

[113] A. L. DeVries, D. E. Wohlschlag, *Science (80-.).* **163**, 1073 (1969).

[114] A. L. Devries, *Science (80-.).* **172**, 1152 (1971).

[115] J. G. Duman, *Annu. Rev. Physiol.* **63**, 327 (2001).

[116] M. E. Urrutia, J. G. Duman, C. A. Knight, *Biochim. Biophys. Acta - Protein Struct. Mol. Enzymol.* **1121**, 199 (1992).

[117] J. G. Duman, T. Olsen, *Cryobiology* **30**, 322 (1993).

[118] H. Xu, M. Griffith, C. L. Patten, B. R. Glick, *Can. J. Microbiol.* **44**, 64 (1998).

[119] P. L. Davies, C. L. Hew, *FASEB J.* **4**, 2460 (1990).

[120] J. A. Raymond, A. L. Devries, *Proc. Natl. Acad. Sci. U. S. A.* **74**, 2589 (1977).

[121] E. Kristiansen, K. E. Zachariassen, *Cryobiol.* **51**, 262 (2005).

[122] P. W. Wilson, *Cryo Letters* **14**, 31 (1993).

[123] Z. Jia, C. I. DeLuca, H. Chao, P. L. Davies, *Nature* **384**, 285 (1996).

[124] F. D. Sönnichsen, C. I. DeLuca, P. L. Davies, B. D. Sykes, *Structure* **4**, 1325 (1996).

[125] A. B. Siemer, A. E. McDermott, *J. Am. Chem. Soc.* **130**, 17394 (2008).

[126] A. B. Siemer, K.-Y. Huang, A. E. McDermott, *P. Natl. Acad. Sci. USA* **107**, 17580 (2010).

[127] G. Chen, Z. Jia, *Biophys. J.* **77**, 1602 (1999).

[128] J. Baardsnes, P. L. Davies, *Biochim. Biophys. Acta - Proteins Proteomics* **1601**, 49 (2002).

[129] E. I. Howard, *et al.*, *J. Mol. Recognit.* **24**, 724 (2011).

[130] F. Van De Velde, S. H. Knutsen, A. I. Usov, H. S. Rollema, A. S. Cerezo, *Trends Food Sci. Technol.* **13**, 73 (2002).

[131] V. Gaukel, A. Leiter, W. E. Spieß, *J. Food Eng.* **141**, 44 (2014).

[132] Y. Celik, *et al.*, *Proc. Natl. Acad. Sci.* **110** (2013).

[133] L. C. M. van Gorkom, J. M. Hook, M. B. Logan, J. V. Hanna, R. E. Wasylishen, *Magn. Reson. Chem.* **33**, 791 (1995).

[134] A. Böckmann, *Angew. Chem. Int. Ed. Engl.* **47**, 6110 (2008).